Title
Pallidal Modulation of Thalamic Activity in Motor Function

ISBN
9798189297885

Author
Chang, Isaac Yau Ming

Publication Date
2026-09-03

Peer reviewed|Thesis/dissertation

Pallidal Modulation of Thalamic Activity in Motor Function

by
Yau Ming Chang

DISSERTATION
Submitted in partial satisfaction of the requirements for degree of
DOCTOR OF PHILOSOPHY

in

Neuroscience

in the

GRADUATE DIVISION
of the
UNIVERSITY OF CALIFORNIA, SAN FRANCISCO

Approved:

DocuSigned by:
4AF406E430B7472...
Massimo Scanziani
Chair

DocuSigned by:
Alexandra Nelson
Alexandra Nelson

DocuSigned by:
Jeanne Paz
Jeanne Paz

DocuSigned by:
70A483C8DEB04E6...
Vikaas Sohal
Vikaas Sohal

Committee Members

Dedication

I dedicate this dissertation to Tomo, my furry graduate school buddy, who provided unwavering emotional support while contributing absolutely nothing to the experiments.

Acknowledgements

I would like to thank my advisor, Dr. Jeanne Paz, for providing the opportunity to pursue my PhD in her laboratory. I am grateful for the resources, scientific environment, and collaborations that made these studies possible.

I thank the members of my thesis committee Dr. Massimo Scanziani, Dr. Alexandra Nelson, and Dr. Vikaas Sohal, for their guidance and feedback.

I thank my colleagues in the Paz laboratory, the Gladstone Institutes, and the UCSF Neuroscience Graduate Program for creating a welcoming and stimulating research environment.

Finally, I thank my family and friends for their support.

Contributions

Chapter 1 was written by Isaac Y.M. Chang.

Chapter 2 is reproduced from the submitted manuscript, with unpublished data on optogenetic manipulation of GPe→nRT pathway *in vivo*:

> Chang, I. Y. M., & Paz, J. T. (2026). A non-canonical pallidothalamic pathway for motor control (p. 2026.06.08.730902). bioRxiv. https://doi.org/10.64898/2026.06.08.730902

I.Y.M.C. and J.T.P. conceived the study. I.Y.M.C. performed all experiments and analyses. I.Y.M.C. and J.T.P. wrote the paper.

Chapter 3 is reproduced in its entirety from the published manuscript under the terms of the Creative Commons Attribution (CC-BY 4.0) license.

> Chang, I. Y. M., & Paz, J. T. (2025). Distinct firing responses to synthetic synaptic currents in the adult murine reticular and relay thalamus. *Journal of neurophysiology*, *133*(4), 1329–1340. https://doi.org/10.1152/jn.00052.2025

I.Y.M.C. and J.T.P. conceived and designed research; I.Y.M.C. performed experiments; I.Y.M.C. analyzed data; I.Y.M.C. and J.T.P. interpreted results of experiments; I.Y.M.C. and J.T.P. prepared figures; I.Y.M.C. and J.T.P. drafted manuscript; I.Y.M.C. and J.T.P. edited and revised manuscript; I.Y.M.C. and J.T.P. approved final version of manuscript.

Chapter 4 was written by Isaac Y.M. Chang.

Pallidal Modulation of Thalamic Activity in Motor Function

Isaac Yau Ming Chang

Abstract

The nucleus reticularis thalami (nRT) is a sheet of GABAergic neurons that surrounds the thalamus and plays critical roles in sensory processing, attention, and sleep. Despite its central position within thalamocortical circuits, the mechanisms by which GABAergic signals converge and integrate within the nRT remain incompletely understood. The goal of this dissertation was to investigate the organization and functional consequences of GABAergic signaling in the nRT, particularly that originating from the external globus pallidus (GPe), across circuit and behavior. In **Chapter 2**, we characterized a previously underappreciated projection from the GPe to the nRT. We found that GPe input exerts opposing effects across nRT subregions due to regional differences in chloride homeostasis, resulting in either inhibitory or excitatory responses to GPe stimulation. These opposing effects produce distinct downstream consequences in thalamocortical (TC) circuits with a potential role in motor control, thereby identifying the GPe→nRT pathway as a non-canonical route through which the basal ganglia influence thalamic information processing. In **Chapter 3**, we examined how nRT and TC neurons transform synaptic inputs into spiking outputs using synthetic current injections. We found that the same input currents elicited distinct firing responses in nRT and TC neurons, demonstrating that intrinsic cellular properties play a critical role in shaping firing output.

Together, these studies demonstrate that the functional consequences of GABAergic signaling in thalamic circuits are shaped by multiple interacting mechanisms, including chloride homeostasis and intrinsic neuronal properties.

Table of Contents

List of Figures

List of Tables

Chapter 1: Introduction

1.1. Overview

In this dissertation, we aim to understand how GABAergic signaling, particularly that originating from the external globus pallidus (GPe), regulates thalamic activity and motor output. **Chapter 2** presents a detailed characterization of the anatomical connectivity, synaptic properties, *in vivo* activity, and behavioral relevance of a non-canonical pallidothalamic pathway stemming from the GPe to the nucleus reticularis thalami (nRT). **Chapter 3** presents a systematic overview of how nRT neurons and thalamocortical (TC) neurons respond to inhibitory and excitatory synthetic currents, generating a map of which synaptic inputs are transformed into firing output in the thalamus. Finally, **Chapter 4** discusses several speculative hypotheses including the potential role of short-term chloride plasticity in state-dependent behavioral modulation, the functional organization of the GPe→nRT pathway *in vivo*, and the possible relevance of this pathway to neurological disease.

1.2. Classical basal ganglia circuit models

The basal ganglia are a highly interconnected group of subcortical nuclei that play critical roles in motor control, action selection, reinforcement learning, and habit formation. Comprehensive reviews of the basal ganglia are available elsewhere (*1*, *2*). Here, I focus on the prevailing model of basal ganglia-thalamic communication and several observations that motivated this dissertation.

One of the most influential models for understanding basal ganglia function is the rate model, which emerged during the 1980s (*3*, *4*). A central tenet of this model is that basal ganglia network output is integrated at the level of two output nuclei: the internal globus pallidus (GPi) and the substantia nigra pars reticulata (SNr). These nuclei provide tonic inhibitory input to thalamic and brainstem targets to suppress or promote specific actions. Although the field has

since evolved substantially, many contemporary models retain the core concept that the GPi and SNr serve as the principal output pathway through which the basal ganglia influence behavior. Within this framework, the GPe has traditionally been viewed as an intrinsic nucleus that relays information between basal ganglia nuclei.

Although this framework has provided an invaluable foundation for understanding basal ganglia function, several observations suggest that it may not fully capture the complexity of basal ganglia circuitry. Notably, focal lesions or inactivation of the GPi in both Parkinson's disease patients (*5*) and non-human primates (*6*, *7*) do not produce the severe motor deficits predicted by a model in which all basal ganglia output is routed through the GPi. These findings raise the possibility that additional pathways exist that contribute to basal ganglia-thalamic communication. Furthermore, recent studies have revealed extensive cellular heterogeneity within the GPe (*8*) and identified GPe projections to numerous targets both within and outside the basal ganglia. These findings have challenged the traditional view of the GPe as a simple relay nucleus and instead suggest that it may participate more directly in regulating brain-wide network activity.

The pathway from the GPe to the nucleus reticularis thalami (nRT) represents an attractive candidate for an alternative route of basal ganglia-thalamic communication **(Fig. 1.1)**. Unlike the canonical GPi/SNr output pathway, the GPe→nRT projection provides a route through which the basal ganglia could influence thalamocortical processing indirectly by modulating thalamic gating mechanisms. Given the central role of the nRT in regulating information flow through the thalamus, this pathway may represent an important but understudied mechanism through which the basal ganglia influence behavior.

In addition, accumulating evidence has demonstrated that the basal ganglia are organized into multiple structurally and functionally distinct cortico-basal ganglia-thalamic circuits, defined by the topographical organization of cortical inputs and their corresponding thalamic targets (*9*). Despite exhibiting a comparable topographical organization (*10*, *11*) and being strategically positioned to regulate thalamocortical communication, the nRT was never incorporated into these

canonical circuit models. Consequently, the potential contribution of the nRT to basal ganglia information processing has remained largely unexplored.

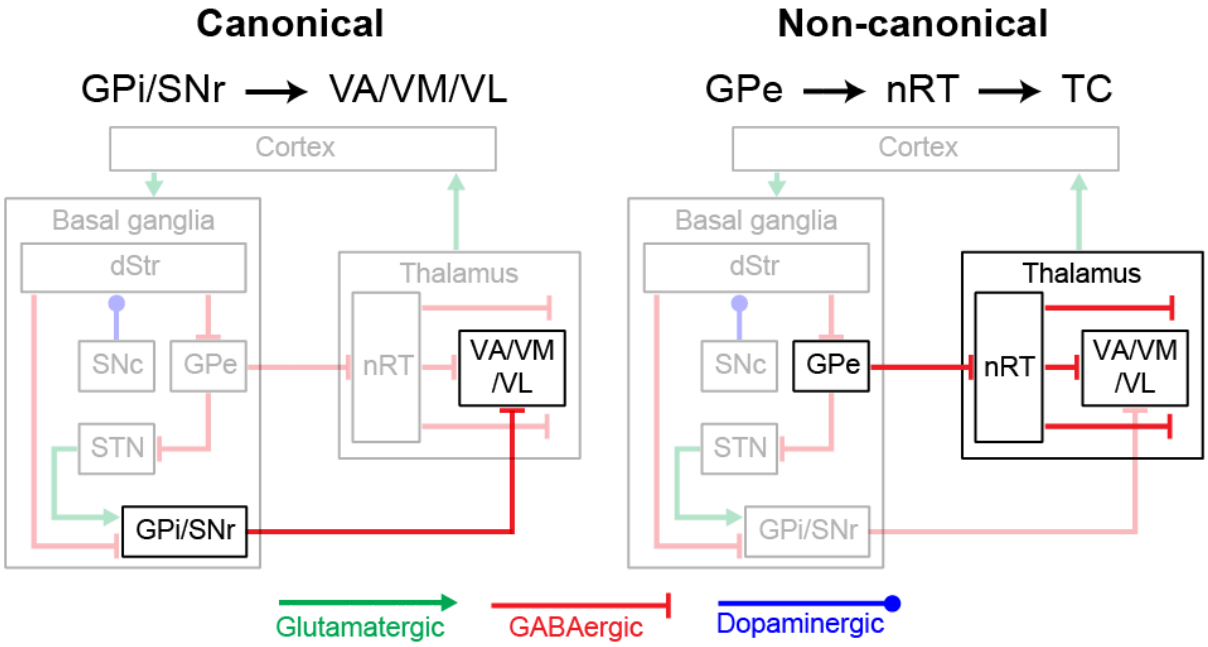

Figure 1.1. Two basal ganglia motor output pathways to the thalamus

Simplified basal ganglia models highlighting two routes in which basal ganglia can communicate with the thalamus in the context of motor control. Adapted from (*12*). Abbreviations: dStr, dorsal striatum; SNc, substantia nigra pars compacta; STN, subthalamic nucleus; GPe, external globus pallidus; GPi, internal globus pallidus; SNr, substantia nigra pars reticulata; nRT, nucleus reticularis thalami; VA, ventral anterior thalamic nucleus; VM, ventromedial thalamic nucleus; VL, ventrolateral thalamic nucleus; TC, thalamocortical nuclei.

1.3. The external globus pallidus

The external globus pallidus (GPe) is a central hub within the basal ganglia and is characterized by extensive connectivity to numerous brain regions and substantial cellular heterogeneity. Comprehensive reviews of the GPe are available elsewhere (*8*, *13*). Here, I focus on the diversity GPe neuronal populations, with particular emphasis on the GPe→nRT projection, which is the primary subject of this dissertation **(Chapter 2)**.

The GPe is composed of multiple molecularly defined neuronal populations **(Fig. 1.2)**. Among these, parvalbumin-expressing (PV^+) and Npas1-expressing ($Npas1^+$) neurons represent the two principal classes and account for approximately 50% and 30% of GPe neurons,

respectively (*14*). These populations are GABAergic and differ in their electrophysiological properties, projection targets, synaptic inputs, disease alterations, and behavioral functions (*14–19*). A subset of GPe neurons (5%) is choline acetyltransferase-expressing (ChAT$^+$) and projects to the cortex. The remaining populations are less well characterized.

The Npas1$^+$ population can be further subdivided into distinct subclasses. Approximately 60% of Npas1$^+$ neurons express Foxp2 and are commonly referred to as arkypallidal neurons. These Npas1$^+$Foxp2$^+$ neurons project primarily to the dorsal striatum (*20*). In contrast, the remaining Npas1$^+$ neurons express Nkx2.1 and project to the cortex, midbrain, and the nRT (*14*, *19*). The identification of molecularly distinct Npas1$^+$ subclasses has facilitated the study of specific GPe output pathways. Importantly, the development of the Npas1-iCre mouse line has provided an important genetic entry point for investigating the GPe→nRT projection, a pathway that remained poorly understood despite being anatomically recognized for decades.

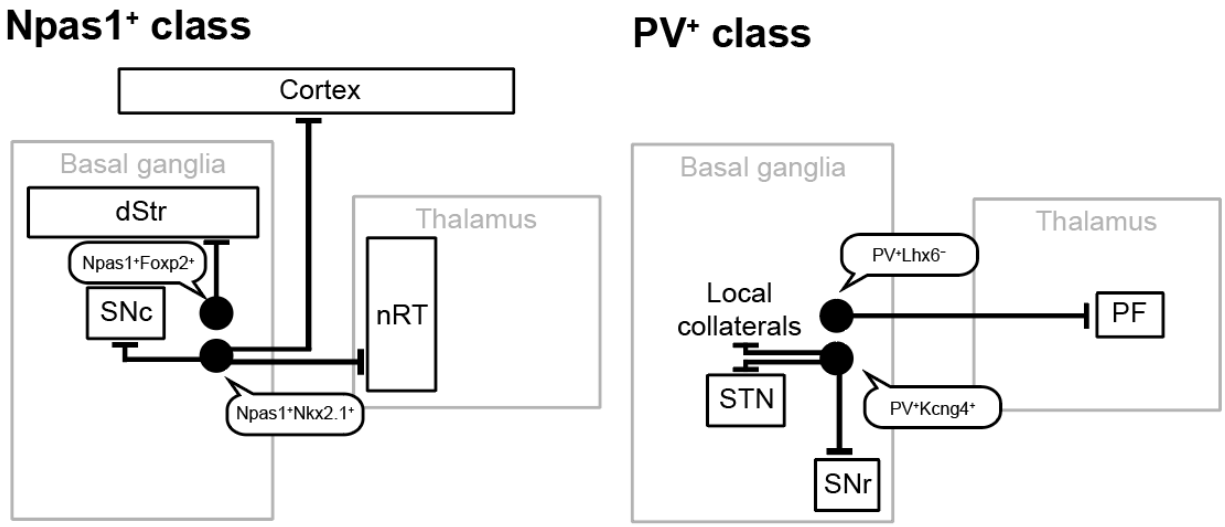

Figure 1.2. Molecular makeup of the GPe
Illustration of the projection targets of GPe neuron subtypes. Adapted from (*8*).

1.4. The nucleus reticularis thalami

The nucleus reticularis thalami (nRT) is a thin sheet of GABAergic neurons that surrounds the main body of the thalamus. Comprehensive reviews of the nRT are available elsewhere (*10*,

21). Here, we focus on the current understanding of the organization of GABAergic signaling within the nRT, focusing on extrinsic GPe input **(Chapter 2)**, and its role in regulating thalamocortical information flow.

Unlike other thalamic nuclei, the nRT does not project to the cortex. Instead, it receives excitatory inputs from both corticothalamic and thalamocortical axons and sends inhibitory projections primarily to thalamocortical (TC) nuclei. Because nearly all signals transmitted from the thalamus to the cortex are gated by inhibitory input from the nRT, it has been hailed as the "guardian of the gateway" **(Fig. 1.3)**. Consistent with this role, the nRT has been implicated in sensory gating (*22*) and modulating attention (*23*, *24*).

One influential framework for understanding nRT function is the searchlight hypothesis (*25*), which proposes that the nRT selectively gates information flow through the thalamus by dynamically suppressing or permitting activity in specific thalamocortical circuits. This framework has traditionally emphasized the role of intrinsic nRT circuitry, where localized activity patterns within the nRT are thought to mediate gating. Considerably less known is how extrinsic GABAergic input shapes nRT activity and contributes to these circuit computations. Understanding how GABAergic signals arising both within and outside the nRT serve to perform this searchlight function remains an important question.

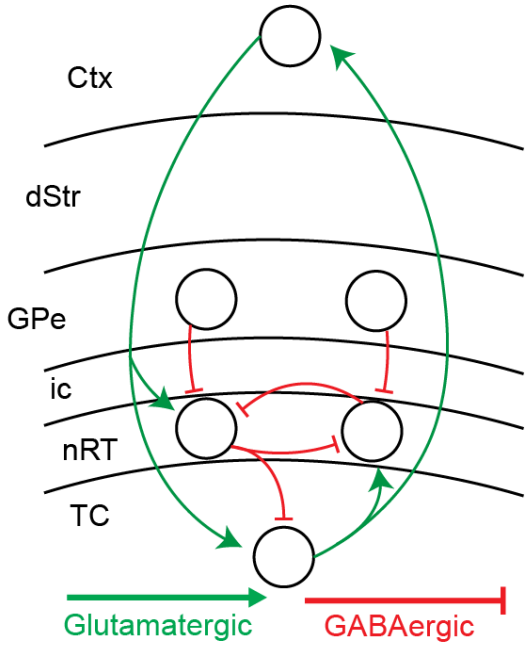

Figure 1.3. Main connections of the thalamocortical circuits
Adapted from (*25*).

1.5. A historical perspective of the GPe→nRT pathway

The GPe→nRT projection has been recognized for nearly five decades, with its first anatomical description dating back to the 1970s (*26*) **(Table 1.1)**. Subsequent studies (*27*–*37*) in rats, cats, and non-human primates confirmed the existence of this projection and established it as an evolutionarily conserved pathway in mammals. A small number of electrophysiological studies have reported that electrical and pharmacological manipulation of the GPe can alter nRT activity (*38*–*42*). However, these studies relied on manipulations that broadly affected all GPe projection neurons, rather than selectively targeting GPe→nRT projection. Consequently, the observed effects may have arisen indirectly through polysynaptic circuits, recurrent network interactions, or other GPe output pathways, making it difficult to determine the specific contribution of the GPe→nRT projection.

The behavioral relevance of the GPe→nRT pathway remains largely unexplored. To date, only one study(*22*) has linked GPe manipulation to behavioral outcomes potentially involving the

nRT. Nakajima et al. found that optogenetic inhibition of the GPe increased auditory nRT activity and improved performance in an auditory discrimination task. However, because the manipulation was applied broadly to the GPe, the extent to which these effects were mediated specifically by the GPe→nRT pathway remains unclear.

Despite decades of investigation, fundamental questions regarding the circuit organization and behavioral function of the GPe→nRT pathway remain unresolved. Addressing these questions is the primary objective of the study presented in **Chapter 2**.

Table 1.1. Previous investigations on the GPe→nRT pathway.

Abbreviations: HRP, horseradish peroxidase; WGA-HRP, wheat germ agglutinin-horseradish peroxidase; PHA-L, Phaseolus vulgaris leucoagglutinin.

Year	Study	Species	Approach	Technique	Main Finding
1976	Severin et al.	Rats	Anatomical	Silver degeneration method and autoradiography	Proof of existence
1978	Carter & Fibiger	Rats	Anatomical	HRP histochemistry and autoradiography	
1979	Nauta	Cats	Anatomical	Autoradiography	
1983	Yamamoto et al.	Squirrel monkeys	Electrophysiological	Electrode recording	GPe electrical stimulation suppressed firing and induced positive field potential in the nRT.
1985	Haber et al.	Rats	Anatomical	Autoradiography	Proof of existence
1989	Asanuma	Rats	Anatomical	PHA-L anterograde tracing	
1990	Asanuma & Porter	Rats	Anatomical	PHA-L and fluoro-ruby anterograde tracing WGA-HRP retrograde tracing Light and electron microscopy	GPe→nRT projection is likely GABAergic
1990	Cornwall et al.	Rats	Anatomical	PHA-L anterograde tracing WGA-HRP retrograde tracing	Proof of existence
1991	Hazrati & Parent	Squirrel monkeys	Anatomical	Biocytin anterograde tracing WGA-HRP retrograde tracing	
1993	Gandia et al.	Rats	Anatomical	WGA-HRP anterograde tracing	
1994	Bickford et al.	Cats	Anatomical	Biocytin anterograde tracing WGA-HRP retrograde tracing	
1994	Asanuma	Squirrel monkeys	Anatomical	WGA-HRP anterograde tracing Light and electron microscopy	
1998	Kayahara & Nakano	Cats	Anatomical	WGA-HRP anterograde tracing	
2013	Pazo et al.	Rats	Electrophysiological	Electrode recording	GPe electrical or pharmacological stimulation suppresed firing in the nRT
2016	Villalobos et al.	Rats	Electrophysiological	Electrode recording	GPe pharmacological stimulation and inhibition suppressed firing and increased firing in the nRT, respectively
2019	Nakajima et al.	Rats	Electrophysiological & Behavioral	Electrode recording & auditory discrimination task	GPe optogenetical inhibition increased audtiory nRT activity and improved behavioral performance in the task
2022	Villalobos et al.	Rats	Electrophysiological	Electrode recording	GPe GAT-1 inhibition increased nRT firing.
2023	Villalobos et al.	Rats	Electrophysiological	Electrode recording	GPe GABA-B activation and inactivation increased and suppressed nRT firing, respectively.

Chapter 2: A Non-canonical Pallidothalamic Pathway for Motor Control

2.1. Abstract

Coordinated movement relies on interactions between the basal ganglia and the thalamus, yet the circuits linking these structures are not fully understood. Here, we dissect a non-canonical basal ganglia output pathway, from the external globus pallidus (GPe) to the nucleus reticularis thalami (nRT). We show that GPe input to the nRT is broad and spatially pervasive. Strikingly, despite its GABAergic nature, GPe input excites the posterior nRT but inhibits the anterior nRT, due to region-specific expression of the chloride transporter KCC2. This divergence shapes downstream thalamocortical activity, producing feedforward inhibition in the somatosensory thalamus but not the motor thalamus. Functionally, the *in vivo* activity of GPe→nRT axons is time-locked to movement, and optogenetic experiments revealed evidence suggestive of state-dependent effects on movement following manipulation of the GPe→nRT pathway. Overall, our work highlights the GPe as a major regulator of thalamic activity and establishes a novel role of the GPe→nRT pathway in motor control.

2.2. Introduction

Movement is orchestrated by interconnected loops between the cortex and subcortical regions. The cortico-basal-ganglia-thalamo-cortical loop, in particular, is a fundamental circuit motif in vertebrates, and its anatomical connectivity is evolutionarily conserved across species (*43*, *44*). The rate model (*3*, *4*), formulated in the 1980s, provided a functional and structural framework for the cortico-basal-ganglia-thalamo-cortical loop in motor function and dysfunction. A key component in this model is that basal ganglia output converges at the level of two nuclei, the internal globus pallidus (GPi) and the substantia nigra pars reticulata (SNr). The GPi/SNr, in turn, projects to the motor thalamus. In this working model, the GPi/SNr→motor thalamus

pathway is thought to be the sole canonical basal ganglia output. Accordingly, one would predict that disruption in this canonical pathway would be detrimental to motor function. However, focal lesions or inactivation of the GPi performed on human Parkinson's disease patients (*5*) do not cause motor disturbances. This and other lines of evidence (*2*) challenge the notion that GPi/SNr are the sole basal ganglia output nuclei and raise the possibility of an additional circuit node that interfaces between the basal ganglia and the thalamus.

The projection pathway from the external globus pallidus (GPe) to the nucleus reticularis thalami (nRT) is of particular interest as a critical junction that bridges information transfer between the basal ganglia and the thalamus. The GPe is a central nucleus in the basal ganglia and sends widespread GABAergic projections to all basal ganglia nuclei, nRT, and regions beyond (*8*). The nRT sends powerful inhibitory connections to all thalamocortical (TC) nuclei, thereby gating information flow from the thalamus to the cortex (*45*). The GPe and nRT play central roles in regulating the network activity of the basal ganglia (*46*) and the thalamus (*25*), respectively. Via the GPe→nRT→TC pathway, the GPe is well-positioned to exert powerful control over TC activity. The existence of the GPe→nRT pathway was first shown in rats (*26*, *27*, *29*, *30*), cats (*28*), and squirrel monkeys (*33*, *36*) in the 1970s, and subsequent anatomical studies (*31*, *32*, *34*, *35*, *37*) followed. Dissecting the GPe→nRT pathway in isolation has been challenging due to the cellular heterogeneity of the GPe (*8*, *14*, *19*). Previous studies examining GPe regulation of nRT activity (*39–42*) or its behavioral role (*22*) largely relied on non-specific pharmacological, electrical, or optogenetic manipulations that engaged multiple GPe populations simultaneously. Given the numerous molecular subclasses of GPe neurons, each with distinct projection patterns, molecular identities, and electrophysiological properties (*8*, *19*), it has been difficult to parse out the specific contributions of distinct GPe pathways. In addition, circuit physiology and behavioral effects have historically been examined independently, leaving unresolved how GPe→nRT circuit dynamics relate to behavioral function.

Here, we provide a detailed characterization of the GPe→nRT pathway at the circuit and behavioral levels. We uncovered a mechanism by which GABAergic GPe input elicits region-specific postsynaptic responses of opposite polarity across the nRT, driven by local differences in chloride homeostasis. We further identified a previously unrecognized GPe→nRT involvement in motor control: specifically, GPe→nRT axons exhibited time-locked activity during movement *in vivo*, and optogenetic manipulation of GPe→nRT axons produced evidence of state-dependent effects on movement.

2.3. Results

GPe sends widespread projections to the entire nRT

To visualize the GPe→nRT projection, we injected adeno-associated virus (AAV) carrying Cre-dependent eYFP into the GPe of Npas1-iCre mice **(Fig. 2.1A)**. Npas1-positive ($Npas1^{+}$) neurons comprise 32.1% of the total GPe population and include GPe→nRT projection neurons (*16*). We observed dense axonal arborizations distributed throughout the entire nRT, whereas TC nuclei were completely devoid of eYFP signal **(Fig. 2.1B)**. Given the robust and selective labeling achieved with this mouse line, we used the Npas1-iCre mice for all subsequent experiments.

To functionally characterize GPe→nRT synapses, we injected AAV carrying Cre-dependent ChR2-eYFP into the GPe of Npas1-iCre mice. Six weeks post-injection, we prepared acute horizontal brain slices and measured optically evoked postsynaptic currents (oPSCs) in nRT neurons **(Fig. 2.1C and D)**. We recorded GABA-receptor-mediated currents in nRT neurons in the presence of blockers of AMPA and NMDA receptors, DNQX (30μM) and APV (100μM), respectively. We optically activated GPe terminals in the nRT using the minimal stimulation intensity, defined as the light power that resulted in a 25–75% success rate. Synaptic currents recorded in this configuration are the result of the activation of a single synapse (*47*). Paired-pulse stimulations revealed no correlation between the paired-pulse ratio and facilitation **(Fig. 2.2)**, consistent with unitary synaptic transmission. oPSCs exhibit exceptionally slow decay kinetics

with a tau decay constant of 263.61 ± 29.42 ms **(Fig. 2.1C)**, typical of $GABA_A$ currents in nRT neurons (*48*). Short-term plasticity of the GPe→nRT synapses was assessed by applying a train of five stimulations at frequencies ranging from 2 to 30Hz. GPe→nRT synapses show activity-dependent short-term facilitation, with the strongest synaptic facilitation at 5 Hz **(Fig. 2.1D)**, which falls within the range of the *ex vivo* spontaneous firing rate of $Npas1^+$ GPe neurons (*16*). We systematically recorded oPSCs across the entire nRT **(Fig. 2.1E)**, and found, remarkably, that GPe stimulation evoked oPSCs in 100% (41/41) of recorded nRT neurons, irrespective of their location. Minimal oPSC amplitudes are uniformly distributed across all the anterior-posterior, medial-lateral, and dorso-ventral axes **(Fig. 2.1E)**, consistent with GPe providing broad synaptic input throughout the nRT.

Region-specific KCC2 expression drives opposing GABAergic GPe→nRT signaling

To assess how GPe input modulates nRT activity, we performed tight-sealed cell-attached recordings to monitor the firing changes of nRT neurons in response to optical stimulation of GPe→nRT terminals, without perturbing the intracellular milieu **(Fig. 2.3A)**. GPe stimulation reduced firing in 21.3% (13/61) of nRT neurons and did not affect firing in 26.2% (16/61) of nRT neurons. Surprisingly, activation of GABAergic GPe input increased firing in 52.5% (32/61) of nRT neurons **(Fig. 2.3B)**. This finding was unexpected as GABAergic transmission is typically inhibitory in the adult brain, and examples of excitatory GABAergic synapses capable of directly driving firing are rare (*49*–*51*). Mapping the locations of recorded cells revealed a striking spatial segregation in GPe-evoked response: cells excited by GPe input were predominantly located in the lateral-posterior nRT, whereas those in the anterior-lateral nRT were more likely to be inhibited **(Fig. 2.3D)**, revealing opposing effects of GPe input across these two regions.

How could a single source of GABAergic pallidal input produce this divergence in firing response? The effect of $GABA_A$ receptor activation is determined by the difference between the membrane potential (Vm) and the chloride reversal potential (E_{Cl}). To investigate whether a more

hyperpolarized Vm at rest could be responsible for the increased firing (as GABA is depolarizing if and only if E_{Cl} > Vm), we measured Vm upon rupturing the membrane into whole-cell mode. Vm was similar between the three groups of responders **(Fig. 2.3C)**, suggesting that the excitatory effects of GABA did not arise from differences in Vm.

Next, we tested the hypothesis that regional differences in chloride homeostasis, specifically mediated by the chloride transporter, KCC2, underlie the mixed responses upon GPe stimulation. KCC2 is a neuron-specific transporter that extrudes chloride ions (Cl^-) from the cell, thereby maintaining a low intracellular chloride concentration, which is essential for hyperpolarizing GABAergic signaling in the adult brain. In rodents, it has been shown that the anterior and dorsal regions of the nRT are immunopositive for KCC2, but KCC2 is not present in other regions of the nRT (*52*, *53*). We performed KCC2 immunostaining on mouse horizontal brain sections and found a clear anterior-posterior gradient of KCC2 expression within the nRT **(Fig. 2.3E)**. KCC2 immunoreactivity was strong in the anterior nRT but was minimal in the posterior region. The expression pattern of KCC2 closely mirrored the GPe-evoked response pattern along the anterior-posterior axis **(Fig. 2.3D)**. These data are consistent with the model in which high KCC2 expression in the anterior nRT maintains low intracellular chloride and a hyperpolarized E_{Cl}, leading to inhibitory GABAergic responses, whereas reduced KCC2 expression in the posterior nRT leads to elevated intracellular chloride, depolarized E_{Cl}, and excitatory GABAergic responses.

To test whether KCC2 determines the polarity of GPe-evoked responses, we pharmacologically blocked KCC2 using the selective antagonist VU 0463271 (100 μM) and examined whether GPe-mediated inhibition could be converted into excitation under KCC2 blockade. We quantified the response profiles in anterior nRT from slices incubated with or without VU. Under control conditions, the majority of anterior nRT neurons were inhibited by GPe stimulation. KCC2 blockade increased the proportion of neurons exhibiting excitation in response to GPe stimulation **(Fig. 2.3F)**, suggesting that KCC2 activity constrains GABAergic signaling

toward inhibitory responses at the population level. To determine whether this effect could occur within individual neurons, we performed VU wash-on experiments in anterior nRT neurons during steady spontaneous firing. Optogenetic stimulation of GPe axons initially suppressed spiking, but following the application of VU, the response progressively shifted from inhibition to excitation, and ultimately drove robust burst firing in the same cell **(Fig. 2.3F)**. Together, these findings indicate that KCC2 activity is a key determinant of the polarity of GABAergic GPe input to nRT neurons.

E_{Cl} governs the polarity of GPe-evoked firing response in nRT neurons

Does the observed KCC2 expression pattern translate to underlying differences in E_{Cl} in nRT neurons? We performed gramicidin-perforated patch recordings to measure physiological cell E_{Cl}. Gramicidin is a cation-selective ionophore that preserves native intracellular chloride concentrations while permitting electrical access to the cell, thereby enabling accurate measurement of E_{Cl} (*54*). We took advantage of the slow time course of perforation to first assess GPe-evoked firing response in cell-attached configuration following seal formation **(Fig. 2.4A)**. This approach enabled direct correlation between firing response and the subsequently measured E_{Cl} within the same cell.

After characterizing GPe-evoked response in cell-attached configuration, we monitored access resistance until stable perforation was achieved. E_{Cl} was determined from GPe-evoked currents recorded across command potentials **(Fig. 2.4A)**. Current-voltage (I-V) relationship curves were constructed, and x-intercepts of linear fits were used to determine E_{Cl}. Cells excited by GPe stimulation exhibited significantly more depolarized E_{Cl} than inhibited cells **(Fig. 2.4A)**. Anatomical mapping again revealed a pronounced anterior-posterior gradient in E_{Cl} **(Fig. 2.4B)**, closely mirroring the KCC2 expression pattern **(Fig. 2.4E)** and the distribution of excitatory versus inhibitory responses **(Fig 2.4B)**.

We next tested whether we could control the directionality of nRT neurons' response to GPe by varying intracellular chloride in whole-cell configuration. Whole-cell recordings were performed using pipette internal solutions with varying chloride concentration to manipulate E_{Cl}: –60 mV, –70 mV, and –80 mV. Experimental measurement of cell E_{Cl} obtained from I-V curves closely matched the predicted pipette E_{Cl} **(Fig. 2.4E)**. We injected +150 pA current to depolarize the cell to an active state and measured the relative change in firing rates upon GPe stimulation **(Fig. 2.4C and D)**. Using the –60 mV E_{Cl} internal, 52.4% (11/21) of the cells increased firing, consistent with the proportion of excited cells observed in cell-attached recordings **(Fig. 2.3B)**. In contrast, using the –70 mV and –80 mV E_{Cl} internals, GPe stimulation consistently resulted in inhibitory postsynaptic potentials (IPSPs) and suppressed firing in all nRT cells **(Fig. 2.4D)**. Together, these findings demonstrate that GABA release from GPe axons can exert either activating or suppressing effects depending on the E_{Cl} of nRT neurons.

Finally, we assessed the effects of GPe input on nRT neurons at rest, in the absence of ongoing firing. Consistent with our cell-attached recordings **(Fig. 2.3B)**, GPe stimulation evoked high-frequency burst firing in the posterior nRT neurons **(Fig. 2.4F)**. Notably, evoked action potentials ride on a slow and prolonged depolarizing current, presumably mediated by low-threshold Ca^{2+} channels (e.g., CaV3.3) expressed in nRT neurons (*55*). The number of action potentials increased with more depolarized E_{Cl} internals **(Fig. 2.4F)**.

GPe differentially regulates downstream thalamocortical activity through feedforward inhibition

Given the strong and regionally specialized control of GPe input on nRT activity, we next investigated whether GPe stimulation can differentially modulate the activity of TC neurons downstream of nRT **(Fig. 2.5A)**. We recorded responses in two TC nuclei neighboring the nRT, the somatosensory ventrobasal nucleus (VB), which receives inputs from the posterior nRT, and the motor ventrolateral nucleus (VL), which receives inputs from the anterior nRT (*56*). GPe

stimulation robustly inhibited firing in VB neurons and evoked burst-like IPSPs and inhibitory postsynaptic currents (IPSCs) in VB neurons **(Fig. 2.5B)**, consistent with our finding that GPe stimulation evoked burst firing in the nRT neurons in the posterior region **(Fig. 2.3B and 2.4F)**, which is known to project to the VB thalamus (*57*). In contrast, GPe stimulation produced little to no effect on the firing of VL neurons **(Fig. 2.5C)**. Because nRT neurons are largely silent in acute slice preparations, GPe inhibition of the anterior nRT neurons **(Fig. 2.3B)** would not substantially affect downstream VL activity.

In vivo activity of GPe→anterior nRT pathway tracks movement states and transitions

Given the central role of the GPe in basal ganglia circuitry and motor control, we asked whether the GPe→nRT pathway might be engaged during movement. Previous studies have shown phasic changes in GPe firing (*58*–*65*) and nRT firing (*66*–*69*) during movement. However, whether such activity extends to the Npas1$^+$ subpopulation or specifically to GPe→nRT projection neurons remains unclear. Because the anterior nRT projects to the motor VL thalamus (*56*), we hypothesized that movement might specifically engage the GPe→anterior nRT→VL pathway. Accordingly, we targeted this pathway for our *in vivo* experiments.

To investigate how the GPe→anterior nRT might be modulated during motor behavior, we monitored the real-time activity of GPe axons in the anterior nRT using fiber photometry. We used an axon-targeted GCaMP variant, axon-GCaMP6s (*70*), to image axonal Ca^{2+} dynamics at GPe→anterior nRT terminals. Axonal Ca^{2+} signals serve as a proxy for presynaptic activity and neurotransmitter release (*71*), providing a pathway-specific readout of presynaptic output. Npas1-iCre mice were unilaterally injected with AAV carrying Cre-dependent axon-GCaMP6s into the GPe and implanted with an optical fiber in the anterior nRT **(Fig. 2.6A)**. We monitored mouse speed during self-paced locomotion in an open-field arena **(Fig. 2.7A)** and aligned GPe axonal Ca^{2+} activity traces to mouse speed **(Fig. 2.6B)**. Activity in the GPe→anterior nRT pathway, quantified by the z-scored GCaMP fluorescence signal, increased at movement onset and

decreased at movement offset **(Fig. 2.6C)**. Analysis of the relationship between speed and GCaMP activity revealed a strong linear relationship at low movement speeds (0–1 cm/s), followed by a plateau at higher speeds **(Fig. 2.6D)**. In this low-speed window, pathway activity correlated with speed, with a maximal Pearson correlation of 0.34 ± 0.04. The plateau in signal at higher speeds may reflect sensor saturation or a ceiling effect in GPe→nRT pathway recruitment.

Because activity in multiple basal ganglia nuclei often correlates more strongly with contralateral compared to ipsilateral movements (*72*, *73*), we also asked whether pathway activity was associated with directional turning behavior. We quantified angular velocity based on changes in the mouse heading direction **(Fig. 2.7B)**. Both left and right turns were associated with transient increases in GCaMP activity in GPe→nRT axons in the right hemisphere, but no left/right bias was observed **(Fig. 2.7C)**. This leaves open the possibility that some of the observed fluorescence changes may reflect nonspecific signals associated with locomotion, rather than direction-selective neural activity. Together, these results provide evidence that the GPe→anterior nRT pathway is dynamically coupled to ongoing movement states and transitions in freely behaving mice.

Evidence suggestive of state-dependent modulation of movement following optogenetic stimulation of GPe→anterior nRT terminals

Stimulation of distinct GPe efferent pathways has been shown to produce different behavioral outcomes (*19*). Activation of GPe→dorsal striatum projections suppresses movement (*74*), whereas activation of GPe→subthalamic nucleus projections promotes movement (*75*). To investigate whether perturbing the GPe→nRT pathway can shape motor output, we used optogenetics to modulate the GPe→anterior nRT terminals while monitoring mouse locomotion in open-field arenas. Npas1-iCre mice were bilaterally injected with an AAV expressing Cre-dependent ChR2-eYFP into the GPe, and implanted with optical fibers targeting the anterior nRT **(Fig. 2.8A)**.

First, we tested whether optical stimulation of the GPe→anterior nRT pathway would promote or suppress overall movement in the open field. Because →anterior nRT pathway activity increased around movement onset **(Fig. 2.6C),** we hypothesized that optical stimulation of this pathway would increase movement. Contrary to our hypothesis, analysis of movement speed revealed no detectable difference in speed fold change between ChR2-eYFP and eYFP mice **(Fig. 2.9)**. These observations indicate that, under the stimulation conditions used here, optogenetic activation of the GPe→anterior nRT pathway did not produce a detectable change in overall movement.

The behavioral effects of neural circuit manipulations often depend on the ongoing state of the system or animal. For this reason, averaging behavioral responses across all trials irrespective of baseline movement states can obscure important state-dependent effects. In an exploratory analysis to address this possibility, we stratified optogenetic stimulation trials according to prestimulus speed and examined how the initial motor state might alter the behavioral effect of optical stimulation. This analysis revealed that activating the GPe→anterior nRT pathway produced bidirectional state-dependent effects on locomotion: stimulation following periods of low prestimulus speed increased mouse speed, whereas stimulation during periods of high prestimulus speed robustly decreased mouse speed **(Fig. 2.8B)**.

To quantify this state dependence, we used a linear mixed-effects modeling approach **(Fig. 2.8C)**. For each trial, prestimulus speed was plotted against the corresponding fold change in speed during stimulation, and the slope of this relationship was used as a metric of state-dependent modulation in each mouse (see Methods). Steeper slopes indicate stronger dependence. Notably, eYFP control and no laser control animals also exhibited a modest non-zero slope **(Fig. 2.10)**, likely reflecting the natural tendency of animals to accelerate from low speeds and decelerate from high speeds. To separately quantify the net movement effect of stimulation, we additionally derived a signed-area metric representing the total net change in

speed **(Fig. 2.8C)**. Together, these two orthogonal measures describe both the state dependence and overall net change in movement.

Compared to eYFP controls, ChR2-expressing animals exhibited significantly steeper slopes, indicating enhanced state-dependent modulation of movement **(Fig. 2.8D)**. This effect was consistently observed across both patterned (20 Hz, 5 ms pulse width) stimulation **(Fig. 2.8)** and sustained stimulation **(Fig. 2.10)**. Thus, the behavioral consequences of GPe→anterior nRT activation are not fixed, but appear to depend strongly on the ongoing movement state of the animal. These results suggest that the GPe→anterior nRT pathway dynamically regulates motor output in a state-dependent manner (see Discussion). This apparent state dependence could also reflect regression to the mean, and therefore should be interpreted with caution.

Finally, we asked whether directly manipulating anterior nRT neurons, thereby bypassing GPe input, could produce similar motor effects. We bilaterally injected SOM-Cre mice with an AAV encoding Cre-dependent ChR2-eYFP and implanted optical fibers above the anterior nRT **(Fig. 2.11A)**. Patterned stimulation of SOM^+ nRT neurons produced a significant decrease in signed area, indicating an overall movement suppression **(Fig. 2.11B and C)**. This effect is consistent with the circuit logic in which activation of anterior nRT neurons inhibits VL thalamic activity and suppresses motor output. Interestingly, sustained stimulation of SOM^+ nRT neurons produced the opposite behavioral effect, driving a robust increase in movement **(Fig. 2.12)**. One possible explanation is depolarization block, in which prolonged supraphysiological stimulation paradoxically reduces neuronal firing rather than enhancing activation, as evident in *ex vivo* slices **(Fig. 2.12C)**. Analogous experiments in mice expressing the inhibitory opsin eNpHR3.0 in SOM^+ nRT neurons **(Figure 2.13)** produced a mild change in slope but no significant change in signed area **(Fig. 2.10)**. However, the movement-promoting effect observed during sustained optogenetic stimulation **(Figure 2.12)**, which may induce depolarization block **(Fig. 2.12C)**, is consistent with the idea that inhibiting anterior nRT activity can facilitate movement.

Together, these findings demonstrate that direct manipulation of nRT neurons regulates movement and strongly support the conclusion that the behavioral effects of GPe→nRT pathway stimulation are mediated through nRT circuitry.

2.4. Discussion

This study provides the first integrated analysis of the GPe→nRT pathway levels since its initial identification in the 1970s. We show that this non-canonical pallidothalamic pathway possesses several unique properties supporting its capacity to regulate thalamic activity and motor output: 1) widespread connectivity across the entire nRT; 2) region-specific GABAergic signalling that depends on an anterior-posterior expression of the chloride transporter KCC2; and 3) time-locked activity to movement bouts. These properties position the GPe→nRT pathway as a critical circuit node in basal ganglia-thalamus communication.

Opponent control of thalamic activity through selective activation and inhibition

One of the most unexpected findings in our study was that the broad and near-uniform functional connectivity of GPe→nRT input **(Fig. 2.1E)** did not translate into a homogeneous response across nRT regions: Anterior nRT neurons were inhibited, whereas posterior nRT neurons were excited in response to GPe stimulation **(Fig. 2.3B)**. This bidirectional modulation of nRT activity was shaped by an anterior-posterior gradient in KCC2 expression, with high levels in the anterior nRT and low levels in the posterior nRT **(Fig. 2.3E)**, resulting in a similar anterior-posterior gradient of E_{Cl} **(Fig. 2.4B)**. Previous studies have reported a wide range of E_{Cl} in the nRT (*53*, *76*–*78*), ranging from −71.0 mV (*77*) to −45.0 mV (*76*). We show that the KCC2 expression gradient described here **(Fig. 2.3E)** provides a molecular explanation for this variability of E_{Cl}, and that E_{Cl} is spatially organized along the same anterior-posterior gradient as KCC2 expression **(Fig. 2.4B)**.

What does the dual and opposing effect of GPe GABAergic input on the nRT mean for information gating in the thalamus? The nRT has long been proposed to function as a “searchlight”

that selectively gates information flow through the thalamus, thereby shaping sensory processing, attention, and behavior (*25*). The original formulation proposes that this searchlight function is mediated through intrinsic intra-nRT connections, whereby localized nRT activity patterns selectively gate downstream TC nuclei. Our findings suggest an additional, complementary mechanism in which this searchlight function may be achieved through region-specific GABAergic excitation and inhibition from the GPe. Specifically, the inhibitory GPe→anterior nRT pathway and excitatory GPe→posterior nRT pathway may constitute parallel information streams that are recruited under certain behavioral conditions. This unique circuit architecture could enable flexible and context-dependent modulation of thalamic output (*23*).

In addition, the organization of the extrinsic GPe→nRT input differs from that of intrinsic intra-nRT connectivity. Whereas intra-nRT connections are relatively sparse, GPe→nRT input is pervasive and distributed throughout the nRT (*79*), suggesting these systems likely serve complementary roles. Intrinsic intra-nRT connectivity is well-positioned to mediate local interactions between neighboring nRT neurons and coordinate activity within regions. In contrast, the widespread nature of GPe→nRT suggests thalamic gating on a broader scale, dynamically regulating thalamic activity across regions.

One open question is the functional role of GPe input to the rest of the nRT, such as the posterior region, which is excited by GPe input and thus provides feedforward inhibition onto the VB thalamus **(Fig. 2.5)**. Given the established role of VB in sensory processing (*57*, *80*), this pathway may contribute to sensory filtering mechanisms that suppress irrelevant or distracting inputs while enhancing the salience of behaviorally relevant signals. Consistent with this, broad optogenetic suppression of the GPe has previously been shown to enhance behavioral performance in an auditory discrimination task through the auditory nRT (*22*). The GPe→posterior nRT→VB pathway may similarly contribute to filtering background noise activity through feedforward inhibition and improve neural signal-to-noise ratio. Although the present study

primarily focuses on motor-related functions of the GPe→anterior nRT pathway, defining the role of the GPe→posterior nRT pathway will be an important future direction.

A conceptual framework for chloride dynamics in state-dependent movement modulation

In freely behaving mice, we did not observe a global effect of optogenetic stimulation of GPe axons on locomotion. However, in an exploratory analysis, we found that stimulation of this pathway could produce bidirectional behavioral effects that depend on the animal's initial movement state. Specifically, when mice were already moving at high speeds, activation of the GPe→anterior nRT pathway appeared to suppress movement, whereas stimulation during stationary periods or low speeds seemed to promote movement **(Fig. 2.8)**. This state-dependent effect is particularly intriguing and suggests that the functional impact of GPe→anterior nRT input may depend on the ongoing network state.

One potential mechanism is activity-dependent chloride dynamics in nRT neurons. During high-movement states, sustained GABA release from the GPe could promote intracellular chloride accumulation in nRT neurons, shifting E_{Cl} towards more depolarized values. Under this condition, GPe→anterior nRT input could depolarize anterior nRT neurons, thereby enhancing inhibition of the VL thalamus and suppressing movement. In contrast, during low-movement states, lower levels of GPe activity may favor restoration of a more hyperpolarizing E_{Cl} through chloride extrusion, thus inhibiting anterior nRT and disinhibiting the VL thalamus to promote movement. This activity-dependent circuit effect shift is well supported by established biophysical principles of short-term ionic plasticity. High-frequency GABAergic transmission is well-documented to cause rapid, localized intracellular chloride accumulation when the rate of chloride influx outpaces the native extrusion capacity of the neuron (*53*, *81*). Our fiber photometry data demonstrated that GPe→anterior nRT terminals are sustainedly activated during high-speed locomotion **(Fig. 2.6C and D)**. The resulting high-volume GABA release could drive activity-dependent chloride loading in anterior nRT neurons. This chloride loading could progressively depolarize E_{Cl} from baseline,

dynamically shifting GPe-evoked responses from inhibitory to excitatory. Directly tracking real-time intracellular chloride shifts *in vivo* remains technically challenging because of the pH-sensitivity of current biosensors and temporal resolution (*82*, *83*). Here, we provide this conceptual framework, suggesting how short-term ionic plasticity can act as a dynamic substrate for state-dependent motor control.

Although we cannot entirely exclude the possibility that stimulating GPe→nRT axons could produce antidromic activation of GPe somata and engage local GPe circuitry through collateral interactions, direct manipulation of nRT neurons produced behavioral effects consistent with those observed following GPe→nRT terminal stimulation. Specifically, activation of nRT neurons suppressed movement at high speeds, whereas inhibition of nRT activity through depolarization block increased movement at low speeds. These effects were similarly state-dependent, supporting that the nRT is the primary downstream effector through which the GPe→nRT pathway regulates motor behavior.

Implications for basal ganglia-thalamus connectivity and function

The classical circuit model posits the GPi and the SNr as the canonical output nuclei of the basal ganglia, which give rise to GABAergic projections that inhibit the motor thalamus, thus inhibiting movement. Due to their characteristically high tonic firing rates *in vivo* (*84*, *85*), GPi/SNr are thought to tonically inhibit the motor thalamus (*86*). Movement initiation requires a transient pause in GPi/SNr firing, thereby disinhibiting the motor thalamus and allowing motor programs to be executed (*87*).

How the non-canonical GPe→nRT pathway operates alongside the canonical GPi/SNr pathway to coordinate movement remains to be determined. The activity of GPi/SNr is controlled upstream through a population of GPe neurons that are parvalbumin-positive and distinct from the Npas1^{+} GPe neurons that project to the nRT. The relative *in vivo* firing patterns of these two GPe subtypes have been studied in dopamine-depleted animals (*20*, *46*), but not under

physiological conditions. Thus, it is currently difficult to determine whether these pathways operate in concert, in opposition, or in parallel. Simultaneous monitoring of both pathways during behavior will be essential to elucidate how they shape thalamic activity and motor output.

Conclusions and outlook

This work expands the classical basal ganglia model by positioning the GPe as an output nucleus that directly regulates thalamic activity alongside the canonical GPi/SNr output pathway. Our findings demonstrate that basal ganglia-thalamic communication is not a static inhibitory gate, but a dynamic system capable of bidirectional motor modulation. We establish the GPe→nRT pathway as a previously underappreciated component of motor circuitry with broad implications for thalamic function and motor control in health and disease.

2.5. Methods

Mice

We performed all experiments per protocols approved by the Institutional Animal Care and Use Committee at the University of California, San Francisco, and Gladstone Institutes. Precautions were taken to minimize stress and the number of animals used in all experiments. Adult (P56–P180) male and female mice were used. C57BL/6J mice (wild-type, IMSR_JAX:000664), SOM-Cre mice (SOM-IRES-Cre, IMSR_JAX:013044), and Npas1-iCre (Npas1-Cre-2A-tdTomato BAC transgenic line 1, IMSR_JAX:027718, generously provided by Dr. Aryn Gittis, Carnegie Mellon University) were used.

Viral injections and optic fiber implantations

Mice aged postnatal day 50–70 were anesthetized with 2–5% isoflurane and secured in a stereotaxic apparatus (Kopf Instruments). AAV constructs were delivered using the following coordinates into the GPe: (relative to bregma, AP: –0.28 mm; ML: 2.10 mm; DV: 4.00 mm, 150 nL, 30 nL/min); into the anterior nRT: (relative to bregma, AP: –0.70 mm; ML: 1.30 mm; DV: 3.70 mm and 4.10 mm at two DV positions, 40 nL each, 20 nL/min). For all injections, the MicroSyringe

Pump Controller (Micro4, WPI), NanoFil syringes (10 µL, WPI), and 33-g beveled NanoFil needles (NF33BV-2, WPI) were used. After injection, the needle was left at the injection site for 5 min before slow withdrawal to allow diffusion and minimize backflow. Viral injections were performed unilaterally for *ex vivo* slice electrophysiology and fiber photometry, and bilaterally for *in vivo* optogenetic experiments. Experiments were performed at least six weeks after viral injections.

For circuit mapping experiments, we injected AAV5-EF1a-DIO-EYFP (RRID: Addgene_27056, 9.6 × 10^{12} GC/mL) into the GPe or nRT. For optogenetic experiments, we injected AAV5-EF1a-double floxed-hChR2(H134R)-EYFP-WPRE-HGHpA (RRID: Addgene_20298, 17 × 10^{12} GC/mL) for optogenetic excitation or AAV5-Ef1a-DIO-eNpHR 3.0-EYFP (RRID: Addgene_26966, 24 × 10^{12} GC/mL) for optogenetic inhibition into the GPe or nRT. For fiber photometry experiments, we injected AAV5-hSynapsin1-FLEx-axon-GCaMP6s (RRID: Addgene_112010, 22 × 10^{12} GC/mL) into the GPe.

For *in vivo* optogenetic experiments, four weeks after viral injections, fiber optic cannulae (Thorlabs, 1.25 mm stainless ferrule, 200 µm core, 0.39 NA) were implanted bilaterally using the following coordinates above the nRT (relative to bregma, AP: –0.58 mm; ML: 1.55 mm, DV: –3.25 mm). Optical fibers were manually cleaved using a ruby scribe to the appropriate length. For fiber photometry experiments, four weeks after viral injections, fiber optic cannulae (Doric Lenses, 1.25 mm zirconia ferrule, 400 µm core, 0.66 NA, 4.0 mm length) were implanted unilaterally using the same coordinates above the nRT. Cannulae were fixed to the skull using dental cement (Henry Schlein, Flow It ALC Flowable Composite A0). Optical fibers were coated with DiI stain to visualize fiber tracts.

Ex vivo patch-clamp recordings

Mice aged postnatal day 90–140 (at least 6 weeks after viral injections) were anesthetized with 4% isoflurane and perfused transcardially with ice-cold sucrose slicing solution containing 234 mM sucrose, 26 mM $NaHCO_3$, 11 mM glucose, 10 mM $MgSO_4$, 2.5 mM KCl, 1.25 mM

NaH_2PO_4, and 0.5 mM $CaCl_2$, equilibrated with 95% O_2 and 5% CO_2. Brains were rapidly extracted and dissected in ice-cold sucrose slicing solution. Horizontal slices containing the thalamus were cut at a thickness of 250 μm. We incubated the slices, initially at 32 °C for 30 min and then at room temperature (24–26 °C) for 1 h, in artificial cerebrospinal fluid (ACSF) containing 126 mM NaCl, 26 mM $NaHCO_3$, 10 mM glucose, 2.5 mM KCl, 2 mM $CaCl_2$, 1.25 mM NaH_2PO_4, and 1 mM $MgSO_4$, equilibrated with 95% O_2 and 5% CO_2.

Following incubation, brain slices were transferred to the recording chamber and superfused with ACSF at a flow rate of 2 mL/min at room temperature. We obtained recordings from nRT and TC neurons visually identified using differential contrast optics with an Olympus microscope (60X objective; numerical aperture, 1.1; working distance, 1.5 mm; SKU 1-U2M592). Recording electrodes made of borosilicate glass had a resistance of 3–6 MΩ when filled with an internal solution. In all recording conditions, we monitored access resistance (Raccess), and cells were included for analysis only if the Raccess was <25 MΩ. All recordings were performed in the presence of DNQX (30 μM, Sigma-Aldrich, no. D0540) and DL-2-Amino-5-phosphonopentanoic acid (APV) (100 μM, Sigma-Aldrich, no. A5282) to pharmacologically isolate GABA-mediated events. Electrophysiological data were acquired at 100 kHz and filtered at 3 kHz using a Multiclamp 700B amplifier (Molecular Devices) and the pClamp11 software suite (Molecular Devices).

For voltage-clamp recordings, the internal solution contained 135 mM CsCl, 10 mM HEPES, 10 mM EGTA, 5 mM QX-314 (lidocaine N-ethyl bromide), and 2 mM $MgCl_2$, pH adjusted to 7.3 with CsOH (290 mOsm/kg). E_{Cl} was estimated to be about 0 mV based on the Nernst equation. Neurons were clamped at –65 mV. Junction potential, calculated using the JPCal Program in Clampex, was –3.2 mV and left uncorrected.

For cell-attached and current-clamp recordings, the internal solution contained 120 mM potassium gluconate, 11 mM KCl, 10 mM HEPES, 1 mM EGTA, 1 mM $MgCl_2$, 1 mM $CaCl_2$, pH adjusted to 7.4 with KOH (290 mOsm/kg). E_{Cl} was estimated to be about –60 mV based on the

Nernst equation. Some experiments used internal solutions with –70 mV and –80 mV $E_{Cl,}$ which contained the same ingredients but with 127 mM potassium gluconate/4 mM KCl, 129 mM potassium gluconate/2 mM KCl, respectively. We clamped the neurons at –80 mV for cell-attached recordings. The three internal solutions used had junction potentials of –12.5 mV (E_{Cl}: –60 mV), –13.2 mV (E_{Cl}: –70 mV), and –13.7 mV (E_{Cl}: –80 mV). Junction potentials were corrected offline. In a subset of experiments, KCC2 was blocked by bath application of the selective antagonist, VU 0463271 (100 µM, Sigma-Aldrich, SML2333).

For perforated-patch recordings, the internal solution contained 130 mM KCl, 10 mM HEPES, 10 mM EGTA, 1 mM $MgCl_2$, 1 mM $CaCl_2$, pH adjusted to 7.3 with KOH (290 mOsm/kg). The internal solution was first warmed to 37°C, and combined with a stock solution of gramicidin A (dissolved in DMSO, Sigma-Aldrich, no. 50845) to achieve a final concentration of 100 µg/mL. The solution was then vortexed and sonicated for 1 min to ensure complete dissolution of gramicidin. Patch pipettes were prepared first by tip-filling with a gramicidin-free solution, and then back-filled with the gramicidin solution. To minimize gramicidin precipitation, the internal solution was vortexed every hour during experiments. Patch pipettes with a blunt taper were used to facilitate diffusion of gramicidin to the tip. After initial seal formation, perforation was then monitored by tracking Raccess, which was determined from the current response to a −10 mV voltage drop. Mean Raccess at the start of E_{Cl} measurement was 71.28 ± 3.30 MΩ. Recordings that failed to reach these Raccess values within the first 10 minutes rarely achieved sufficient quality. Rupture or breakthrough of the patch was determined by a supraphysiological cell E_{Cl}. Pipette E_{Cl} was estimated to be about 0 mV based on the Nernst equation, which is not physiologically plausible. Junction potential was –2.8 mV and left uncorrected. To account for voltage errors introduced by large Raccess, offline correction was performed. The voltage drop across the Raccess was calculated by multiplying the measured current response by the Raccess, and this value was subtracted from the command voltage to estimate the actual membrane potential.

Fiber photometry

Fiber photometry was performed two weeks after optical fiber implantations. Behavioral tests were performed in a standard lit room between 10:00 am and 7:00 pm. Mice were tested in a white plastic open-field cylinder (diameter 30 cm), which was cleaned with 70% ethanol between sessions. On the day before the experimental session, each mouse was allowed to acclimate to the open field for 20 min, with a low-autofluorescence fiber optic cable attached to the implant via a rotary joint (Doric Lenses).

Recordings were performed on an RZ10X processor (Tucker-Davis Technologies) with 405 and 465 LEDs. LED drivers were calibrated such that light power was approximately 15 µW for 405 nm and 20 µW for 465 nm at the tip of the optical fiber. For axon-GCaMP6s excitation, 405 nm and 465 nm LEDs were sinusoidally modulated at distinct frequencies (210 Hz and 330 Hz, respectively). Fluorescence signals and mouse behavior were recorded for 1 h. An overhead camera (Allied Vision) was used to acquire mouse behavior in the open field at 10 fps, 640 x 480 px per frame. Mouse position was tracked using DeepLabCut. After the completion of behavioral experiments, transgene expression and optical fiber locations were histologically verified *post hoc*. Only histologically validated subjects were included in this study. Mice with baseline locomotor activity less than 1 cm/s were excluded, as this is indicative of abnormal motor behavior, possibly caused by injury during surgical procedures.

In vivo optogenetics

In vivo optogenetic interrogation was performed two weeks after optical fiber implantations. Behavioral tests were performed in a standard lit room between 10:00 am and 7:00 pm. Mice were tested in a white plastic open-field cylinder (diameter 30 cm), which was cleaned with 70% ethanol between sessions. On the day before the experimental session, each mouse was allowed to acclimate to the open field for 20 min, with the fiber optic cable attached to the

implant via a rotary joint (Doric Lenses). Pre-trial, basal ambulatory activity was recorded for 5 min at the beginning of the behavioral session.

For ChR2 activation, mice were subjected to either a single, sustained light pulse or a patterned pulse train (5 ms pulses at 20 Hz) delivered for 10 s. For eNpHR3.0 activation, only the sustained protocol was used. A blue, 450 nm laser (SLOC) was used to activate ChR2, and a green, 532 nm laser (SLOC) was used to activate eNpHR3.0. Lasers were triggered externally using the RZ5 processor (Tucker-Davis Technologies). The light power used for opsin activation was 16–20 mW measured at the fiber tip. Stimuli were delivered with a 1-min intertrial interval, and 20 trials were run for each mouse. An overhead camera (Allied Vision) was used to acquire mouse behavior in the open field at 10 fps, 640 x 480 px per frame. Mouse position was tracked using Deeplabcut. After the completion of behavioral experiments, transgene expression and optical fiber locations were histologically verified *post hoc*. Only histologically validated subjects were included in this study. Mice with baseline locomotor activity less than 1 cm/s were excluded, as this is indicative of abnormal motor behavior, possibly caused by injury during surgical procedures.

Markerless pose estimation

Behavioral videos were analyzed using DeepLabCut (*88*) (DLC) for markerless tracking of mouse body parts. DLC version 3.0.0rc9 was used with default parameters and a pretrained ResNet50. Seven body parts (nose, left ear, right ear, body center, left lateral, right lateral, tail base) were manually labelled. A total of 809 frames from 22 videos were extracted and used to train the network, achieving a final train error of 2.08 pixels and a test error of 2.70 pixels. Raw DLC trajectories were further processed to reduce tracking noise. Frames with likelihood values below 0.3 were excluded and temporarily assigned as missing values. Missing coordinates were subsequently interpolated linearly between adjacent valid frames. To remove isolated tracking spikes, a nearest-neighbor outlier correction algorithm was applied. Individual frames were

identified as artifacts when neighboring frames remained spatially similar while the intermediate frame exhibited a large displacement. In these cases, coordinates were replaced by the average of the adjacent frames. To further constrain implausible tracking jumps, maximum frame-to-frame displacement was limited to 30 pixels per frame. Finally, trajectories were smoothed using a median filter with a kernel size of 5 frames to reduce high-frequency noise. Mouse speed was calculated from the frame-to-frame displacement of the body center, and the maximum speed value was capped at 20 cm/s. Mouse angular velocity was calculated from vectors connecting the body center to the nose and tail base. DLC network is available.

Immunohistochemistry and Microscopy

Mice were perfused with ice-cold 4% paraformaldehyde in phosphate-buffered saline. Serial horizontal or sagittal sections (50 μm) were cut on a sliding microtome (Leica SM2000R). Sections were first incubated in a blocking solution containing Normal Goat Serum (10%, Jackson) and TritonX-100 (0.05%, Sigma) for 2 h at room temperature. They were then incubated with primary antibodies overnight at 4°C. nRT cells were labeled with mouse anti-PV antibody (1:1000, Swant, PV27). KCC2 protein was stained with rabbit anti-KCC2 antibody (1:500, Sigma-Aldrich, 07-432). After washing, sections were further incubated with secondary antibodies for 2 h at room temperature. Secondary antibodies used were goat anti-mouse-Alexa 594 (1:1000, Invitrogen, A11032) and goat anti-rabbit-Alexa 488 (1:1000, Invitrogen, A11008). Sections were mounted in an antifade medium (Vectashield) and images were obtained with a Keyence BZ-9000 microscope. Image analyses were performed with ImageJ.

Quantification

Ex vivo Slice electrophysiology

Characterization of minimal oPSCs: To identify evoked minimal oPSCs, we first applied a Gaussian filter to smooth the raw traces, using a convolution kernel with a 5 ms standard deviation. Traces containing events that preceded the stimulus onset or exhibited unstable

baselines were excluded. Successful events were identified in the smoothed traces using a dynamic threshold set at five times the standard deviation of the pre-stimulus baseline. Only these successful traces were used to compute the mean trace, using the raw (unsmoothed) data. From the mean trace, the following synaptic current features were extracted:

Latency: The time from stimulus onset to 10% rise of the oPSC.

Amplitude: The peak oPSC amplitude.

Rise time: The time between 10% and 90% of the oPSC rise.

Charge: The integral of the oPSC from 10% of the oPSC rise to the return to baseline.

Decay tau (double-exponential, weighted): Obtained by fitting a double-exponential decay function to the oPSC waveform and calculating the weighted time constant:

$$\tau_{D,W} = \frac{A_1\tau_1 + A_2\tau_2}{A_1 + A_2}$$

where A_1 and A_2 are the slow and fast amplitude components, and τ_1 and τ_2 are the slow and fast decay-time constants, respectively.

Detection of extracellular spikes in cell-attached configuration: To isolate negative-going voltage deflections corresponding to extracellular spikes, the voltage trace was inverted to convert troughs to peaks, and peaks were detected using the find_peaks function from the SciPy library. The peaks were detected based on a dynamic threshold set to 70% of the maximum data point in each sweep.

Detection of action potentials in whole-cell configuration: Action potentials were detected based on the first derivative of the voltage trace. Action potential onsets were identified as time points where dV/dt first exceeded 50 V/s.

Fiber photometry

Preprocessing: The first 10 seconds of each recording were discarded to avoid onset artifacts. Signals were low-pass filtered (Butterworth, 2nd order, 2 Hz cutoff) to reduce high-frequency noise, then fit with a double exponential function to capture and remove slow baseline

drift. To correct for motion artifacts, we performed linear regression between the detrended 405 nm and 465 nm signals. The scaled 405 nm trace (motion estimate) was subtracted from the detrended 465 nm signal to yield a motion-corrected GCaMP trace. This corrected signal was then z-scored for normalization across sessions. To align fiber signals with movement, the corrected and z-scored GCaMP trace was temporally resampled to match the movement trace by computing the mean GCaMP signal within each video frame interval.

Detection of movement bouts: To identify discrete movement bouts, we applied a two-threshold algorithm. First, a low threshold of 2 cm/s was used to detect movement onset and offset. Onsets were defined as time points where speed rose above this threshold, and offsets as time points where speed subsequently fell below it. To ensure that only robust movements were captured, a secondary criterion required that the peak speed within each detected bout exceed 5 cm/s. Bouts not meeting this criterion were excluded from analysis.

Detection of left/right turns: To identify discrete turning events, angular velocity traces were thresholded at ±π/2 rad/s. Left turns were defined as timepoints in which angular velocity fell below −π/2 rad/s, whereas right turns were defined as periods in which angular velocity exceeded +π/2 rad/s.

Linear mixed-effects model

For optogenetic interrogations, trial-by-trial behavioral responses were analyzed using linear mixed-effects models implemented in Python with the statsmodels package. To account for repeated measurements within individual animals, mouse identity was included as a random effect with both random intercepts and random slopes. Fixed effects included experimental conditions (eYFP versus ChR2 or eNpHR), prestimulus speed, and their interaction. Prestimulus speed and stimulation-induced speed fold change (Stimulation speed/prestimulus speed) were log-transformed prior to modeling. The primary model was defined as:

$$log_{10}(Speed\ fold\ change_{ij})$$
$$= \beta_0 + \beta_1 Condition_{ij} + \beta_2 log_{10}(PreSpeed_{ij})$$
$$+ \beta_3(Condition_{ij} \times log_{10}(PreSpeed_{ij})) + b_{0j} + b_{1j} log_{10}(PreSpeed_{ij}) + \varepsilon_{ij}$$

Where i denotes individual trials and j denotes individual mice; β terms represent fixed effects; b_{0j} and b_{1j} represent mouse-specific random intercepts and slopes, respectively; and ε_{ij} represents residual error. The eYFP group serves as the reference condition.

Model fitting was performed using restricted maximum likelihood estimation with the LBFGS optimizer. Population-level fit lines were derived from the fixed effects, whereas individual mouse fits incorporated both fixed and random effects. Fit lines were evaluated over the 2.5th to 97.5th percentile range of prestimulus values to exclude extreme outliers.

Two summary metrics were extracted from the fitted regression lines. The slope quantified the degree of behavioral state dependence, with steeper negative slopes indicating stronger suppression of movement at higher prestimulus speeds and stronger promotion at lower prestimulus speeds. In contrast, the signed area quantified the net integrated behavioral effect across the full range of prestimulus speeds, providing a measure of net movement change.

Statistical analyses

General graphing and statistical analyses were performed using Python and Prism (GraphPad). Sample size is defined by the number of observations (i.e., cells or mice). No statistical method was used to predetermine sample size. Data are presented as mean ± standard error of means, unless specified otherwise. Normal distributions of data were not assumed. Animal subjects and cell recordings were randomized within experimental blocks to yield approximately equal sampling of experimental conditions. Statistical significance values and sample sizes are described in the figure legends. Statistical thresholds used were as follows: * $P < 0.05$; ** $P < 0.01$; *** $P < 0.001$; **** $P < 0.0001$; *ns* Not Significant.

2.6. Figures

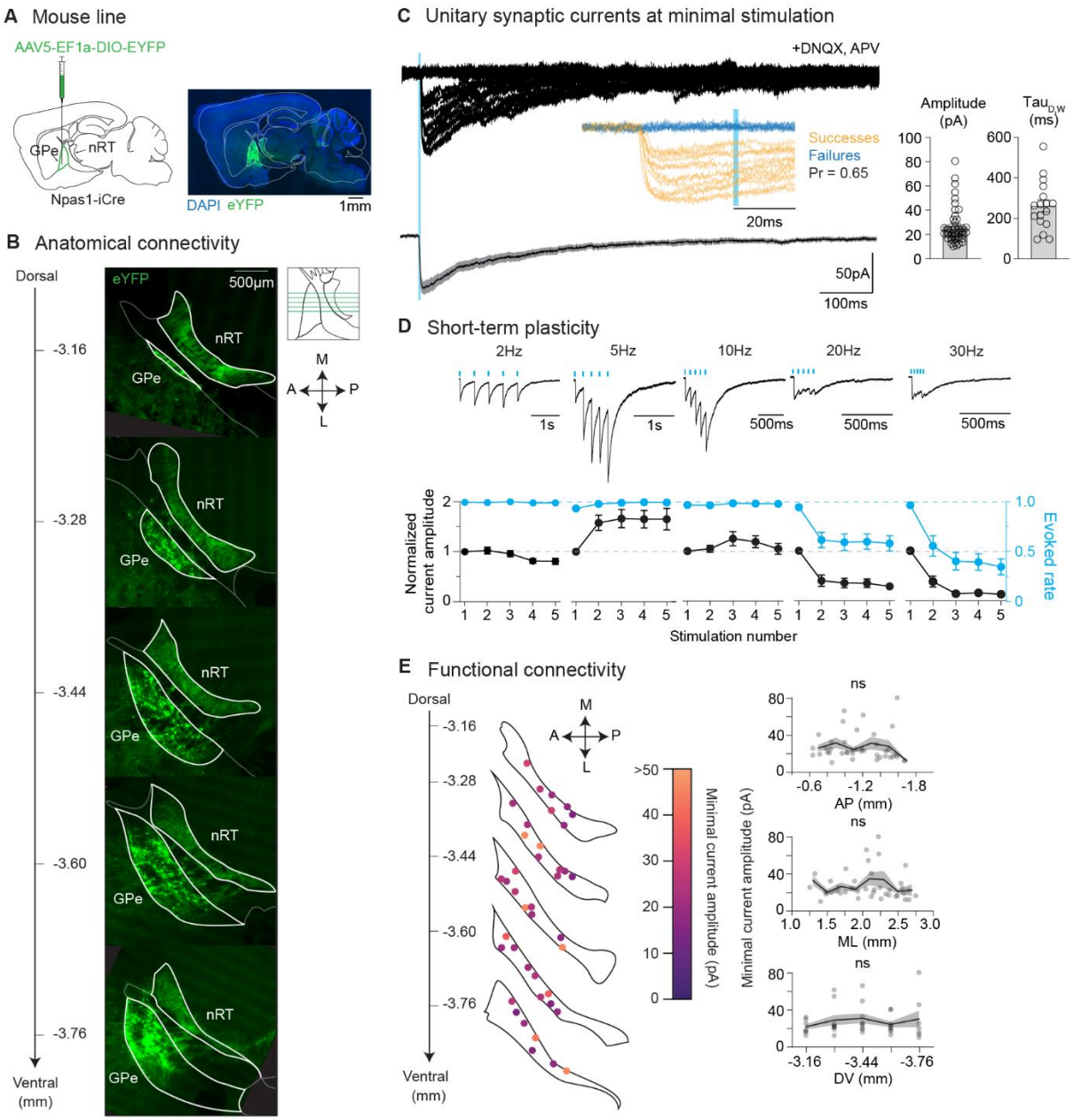

Figure 2.1. GPe sends widespread projections to the entire nRT

(A) Injection schematics. **(B)** Representative images of horizontal brain sections showing the presence of eYFP⁺ GPe axons throughout the entire nRT. Scale bar applies to all panels. **(C)** Top, Representative traces of minimal oPSCs recorded from an nRT neuron in response to activation of a single GPe axon. Inset, expanded view of the traces. Stimulation intensity was adjusted to achieve a ~50% success rate. Bottom, Mean trace ± SEM. Right, Electrophysiological features of minimal oPSCs: Amplitude (*n* = 47 cells) and weighted tau (*n* = 17 cells)**. (D)** Top, Representative traces of oPSCs in an nRT neuron evoked by a train of light pulses delivered at 2 Hz (*n* = 20

(Figure caption continued on the next page.)

(Figure caption continued from the previous page.)
cells), 5 Hz (*n* = 19 cells), 10 Hz (*n* = 19 cells), 20 Hz (*n* = 18 cells), and 30 Hz (*n* = 18 cells) at 1.5× the minimal stimulation intensity. Traces are scaled such that the amplitudes of the first evoked oPSC are the same. Bottom, Normalized current amplitudes and evoked rates across stimulation numbers. **(E)** Left, Connectivity map showing the locations of recorded cells (*n* = 41 cells) and their corresponding amplitudes of minimal oPSCs. Right, Amplitudes of minimal oPSCs across the anterior-posterior (AP), medio-lateral (ML), and dorso-ventral (DV) axes. Note the uniformity of synaptic strength across all three axes. Linear regression (AP: $P = 0.60$; ML: $P = 0.99$; DV: $P = 0.60$).

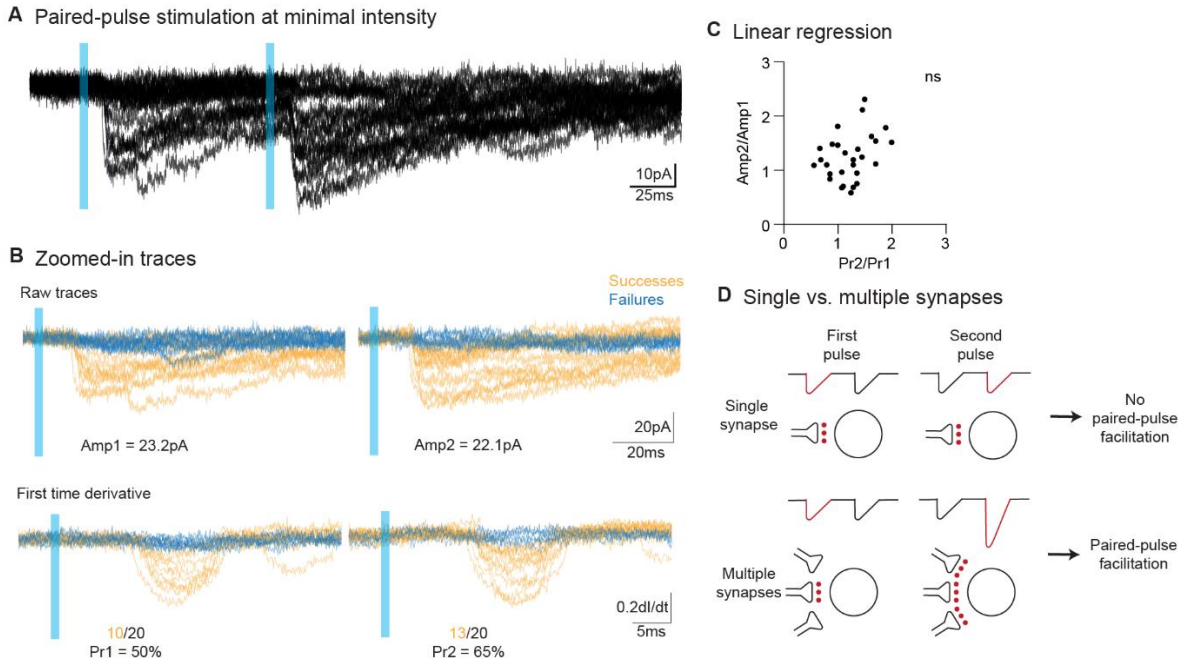

Figure 2.2. Minimal stimulation protocol reflects unitary transmission at GPe→nRT synapse

(A) Representative traces of minimal oPSCs recorded from an nRT neuron in response to paired-pulse stimulation of a single GPe axon. **(B)** Top, Expanded view of raw traces, colored by successes (yellow) and failures (blue). Bottom, Same as Top, but for the first time derivative. **(C)** Scatter plot showing the correlation between the paired-pulse ratio (second oPSC amplitude/first oPSC amplitude) and paired-pulse facilitation (second release probability/first release probability). Linear regression (n = 29 cells, P = 0.11). **(D)** Illustration of the principle of minimal stimulation. For two or more synapses, as release probability increases, both synapses tend to release quanta simultaneously, resulting in a higher amplitude for the second oPSC. However, for a single synapse, the amplitude of the second oPSC remains unchanged despite increasing release probability. For reference, see (*47*).

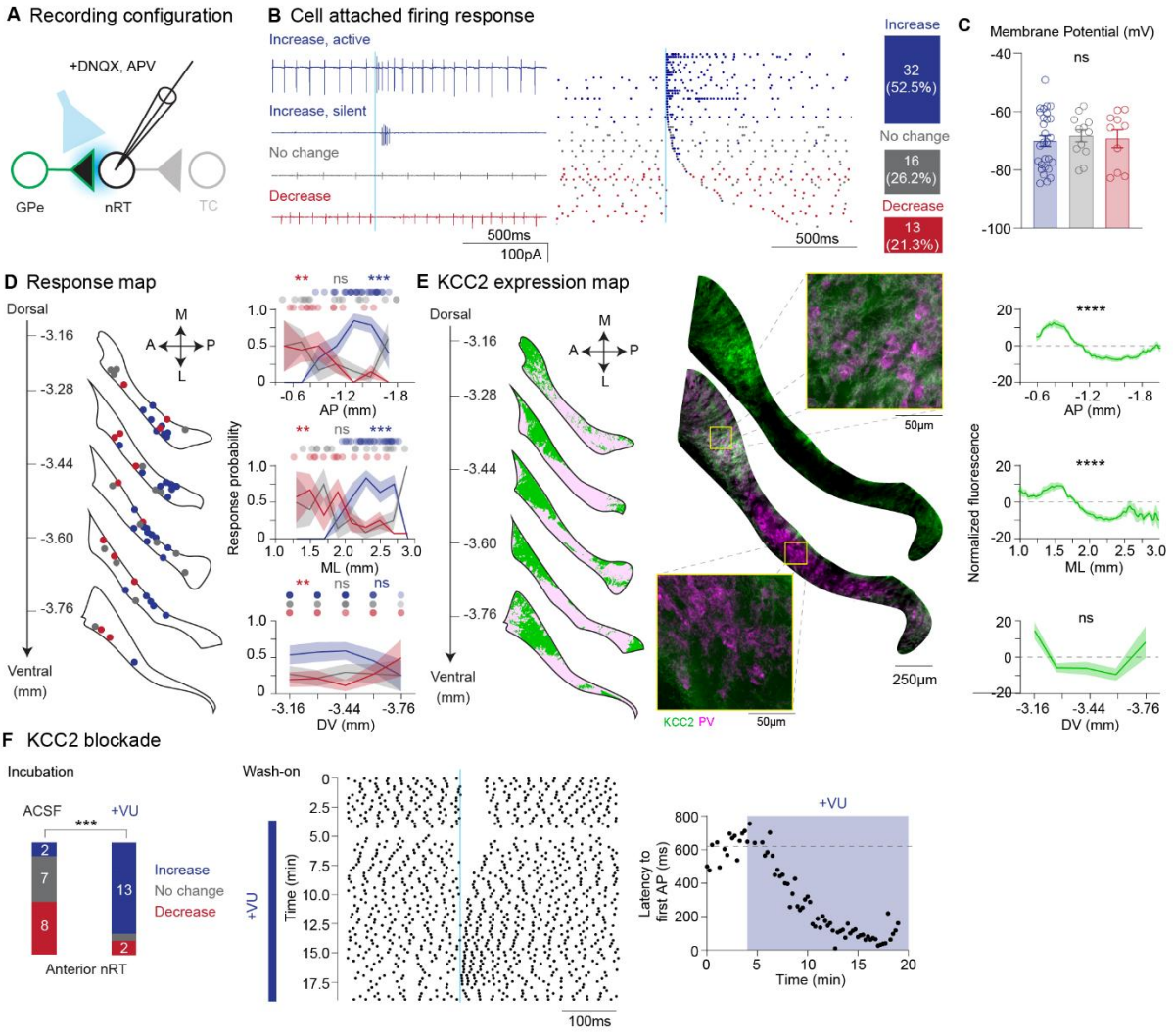

Figure 2.3. Region-specific KCC2 expression drives opposing GABAergic GPe→nRT signaling

(A) Recording configuration. **(B)** Left, Representative traces of cell-attached recordings of nRT neurons in response to GPe axon stimulation. Middle, Raster plot showing spiking activity of all cells recorded, sorted based on the latency to the first spike after stimulation. Right, Numbers and percentages of response types. **(C)** Resting membrane potential values across responders. Kruskal-Wallis test (n = 50 cells, P = 0.94). **(D)** Left, Response map showing the locations of recorded cells (n = 61 cells) and their corresponding firing response. Right, Response probability across the AP, ML, and DV axes. Cells were predominantly inhibited in the anterior-medial regions and excited in the posterior-lateral regions of the nRT. Logistic regression (AP: Increase $P = 1.34 \times 10^{-4}$, No change $P = 0.17$, Decrease $P = 2.68 \times 10^{-3}$; ML: Increase $P = 2.41 \times 10^{-4}$, No change $P = 0.18$, Decrease $P = 5.10 \times 10^{-3}$; DV: Increase $P = 0.39$, No change $P = 0.88$, Decrease $P = 7.44 \times 10^{-3}$). **(E)** Left, KCC2 expression map based on immunohistochemical signal from a representative animal. Middle, Representative images of horizontal brain sections. High-magnification image shows that KCC2 localizes to the perisomatic region and dendrites. Right, KCC2 fluorescence signal, normalized to the average signal of that section (n = 5 mice). KCC2 is restricted to the anterior nRT. Linear regression (AP: $P = <1.00 \times 10^{-10}$; ML: $P = <1.00 \times 10^{-10}$;
(Figure caption continued on the next page.)

(Figure caption continued from the previous page.)
DV: $P = 0.50$). **(F)** Left, Number of response types with and without VU incubation in the anterior nRT. Fisher's exact test (no VU vs. with VU: $n = 33$ cells, $P = 1.91 \times 10^{-4}$). Middle, Raster plot showing the effect of washing on VU 0463721 (KCC2 antagonist) on GPe-evoked response in an nRT neuron. Spiking was initially inhibited by GPe stimulation, and pharmacological blockade of KCC2 transformed GPe inhibition to excitation. Right, Effect of VU as quantified by the latency to the first spike after stimulation. Horizontal dashed line indicates the baseline latency.

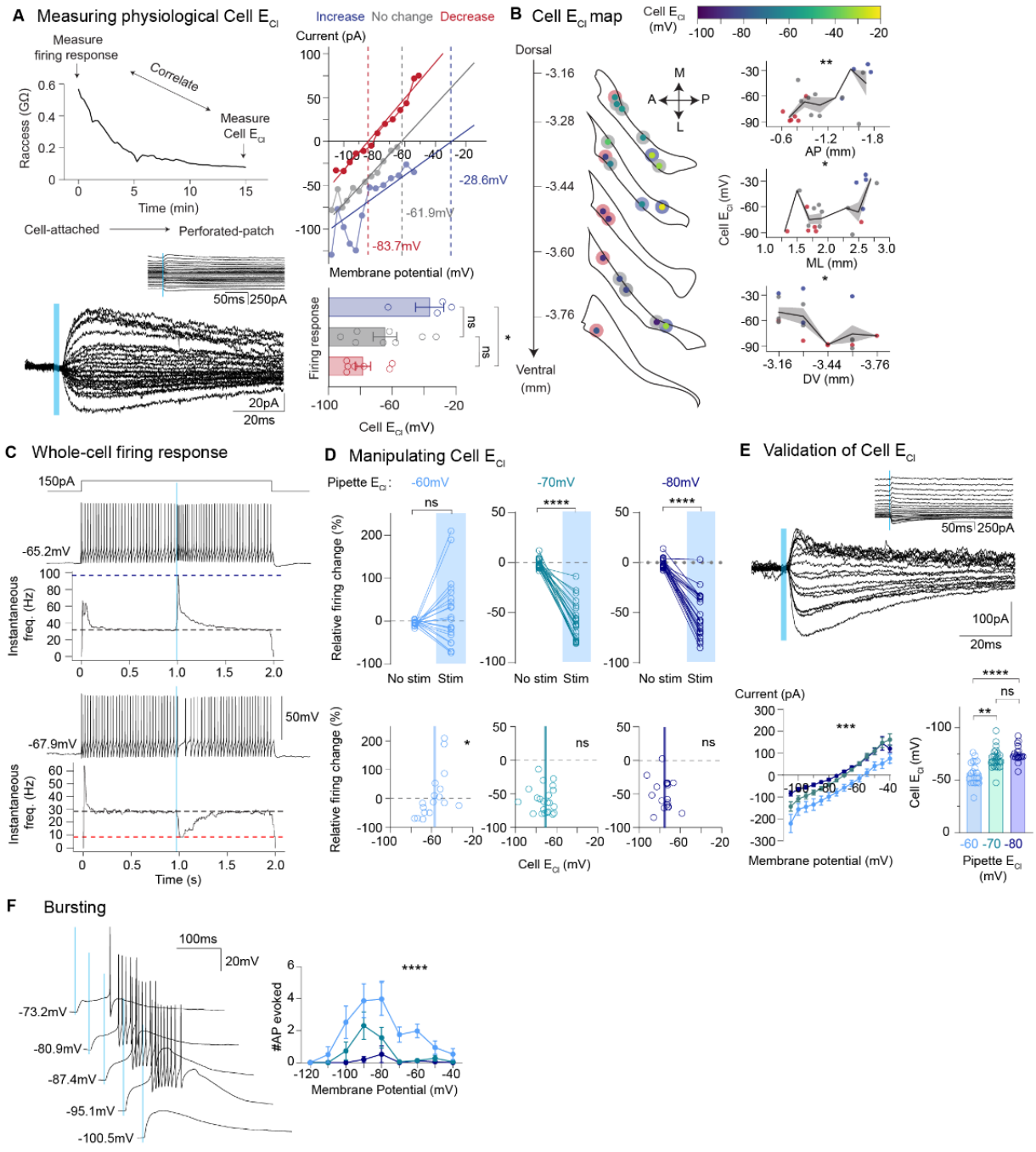

Figure 2.4. E_{Cl} governs the polarity of GPe-evoked response in nRT neurons

(A) Top left, Recording protocol to assess physiological cell E_{Cl} and GPe-evoked firing response within the same cell. Access resistance was continuously monitored every 15 s after seal formation until desirable perforation was achieved. Bottom left, Representative traces of a gramicidin perforated-patch recording. Inset, same traces shown on a longer timescale and without baseline subtraction. Top right, Current–voltage relationship curves of three representative cells that showed a firing decrease (red), no change (gray), or firing increase (blue) prior to E_{Cl} measurement. Vertical dashed lines indicate the x-intercepts. Numbers correspond to (Figure caption continued on the next page.)

(Figure caption continued from the previous page.)
the measured cell E_{Cl} values. Bottom right, Cell E_{Cl} values across responders. Kruskal-Wallis test (n = 19 cells, P = 2.31× 10^{-2}). Dunn's multiple comparisons test (Increase vs. No change: P = 0.23; Increase vs. Decrease: P = 2.54 × 10^{-2}; No change vs. Decrease: P = 0.83). **(B)** Left, Cell E_{Cl} map showing the locations of recorded cells (n = 19 cells) and the correlation between cell E_{Cl} and firing response. Inner circles are color-coded to E_{Cl} values. Outer circles are color-coded to the firing response. Right, Cell E_{Cl} values across the AP, ML, and DV axes. Dots are color-coded to their firing response. Linear regression (AP: P = 4.42 × 10^{-3}; ML: P = 2.10 × 10^{-2}; DV: P = 2.21 × 10^{-2}). **(C)** Top, Representative trace of a whole-cell recording of an nRT neuron in response to GPe axonal stimulation during firing. The cell was recorded with an E_{Cl} = –60 mV pipette internal, which, upon GPe stimulation, increased in firing. Bottom, same as Top, but for a cell that was recorded with an E_{Cl} = –80 mV pipette internal, which decreased firing upon stimulation. Black horizontal dashed line indicates the baseline firing rate. Blue or red horizontal dashed line indicates the poststimulus firing rate. **(D)** Top, Firing responses of cells recorded with different internals: E_{Cl} = –60 mV, –70 mV, –80 mV. Wilcoxon test (–60 mV: n = 21 cells, P = 0.43; –70 mV: n = 23 cells, P = 2.38 × 10^{-7}; –80 mV: n = 22 cells, P = 4.77 × 10^{-7}). Bottom, Correlation between firing rate, shown in Top, and experimentally measured Cell E_{Cl} shown in E. Linear regression (–60 mV: n = 17 cells, P = 1.61 × 10^{-2}; –70 mV: n = 22 cells, P = 0.80; –80 mV: n = 19 cells, P = 0.77). **(E)** Top, Representative traces of oPSCs recorded at different command potentials. Inset, same traces shown on a longer timescale and without baseline subtraction. Bottom left, I-V curves. Mixed ANOVA (n = 60 cells, P = 5.54 × 10^{-4}). Bottom right, Experimentally measured cell E_{Cl} values, which closely match their respective pipette E_{Cl} values. Kruskal-Wallis test (n = 64 cells, P = 1.15 × 10^{-5}). Dunn's multiple comparisons test (–60 mV vs. –70 mV: P = 2.23 × 10^{-3}; –60 mV vs. –80 mV: P = 9.62 × 10^{-6}; –70 mV vs. –80 mV: P = 0.31). **(F)** Left, Representative traces showing evoked burst firing in an nRT neuron in response to GPe stimulation. Right, Number of action potentials evoked across different membrane potentials in the three pipette E_{Cl} conditions. RM two-way ANOVA (n = 68 cells, P = 2.68 × 10^{-5}).

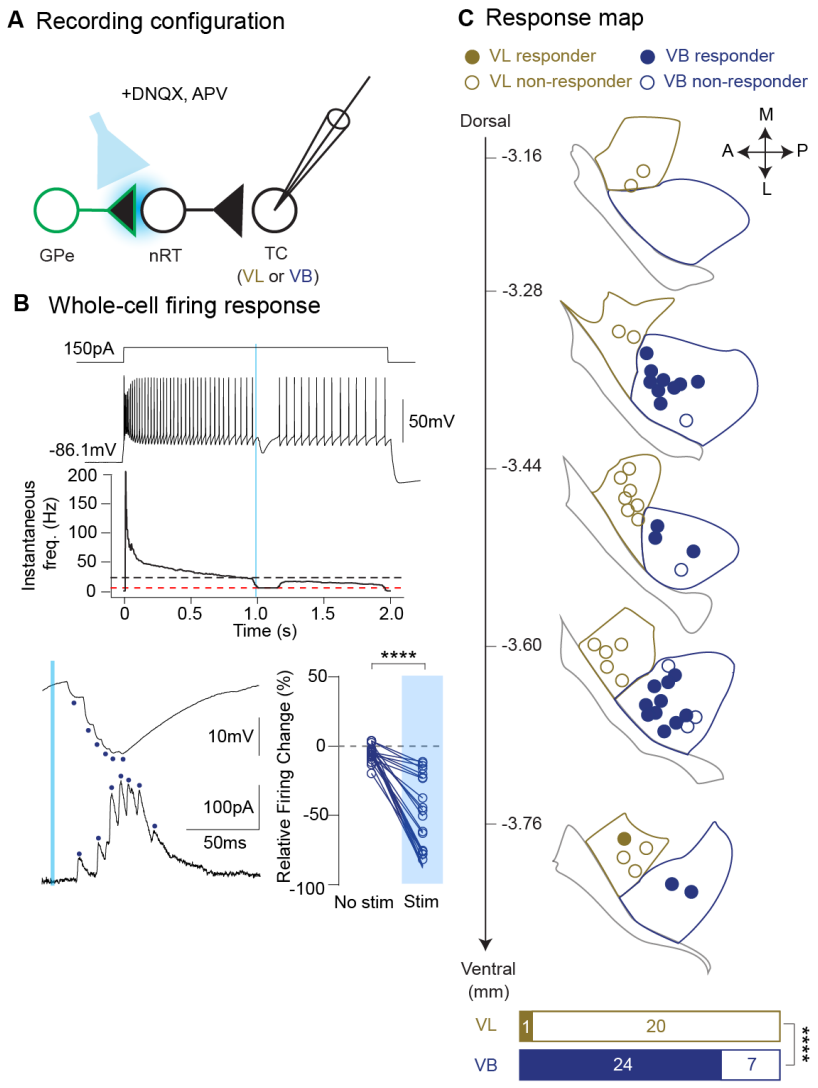

Figure 2.5. GPe differentially regulates downstream thalamocortical activity through feedforward inhibition

(A) Recording configuration. **(B)** Top, Representative trace of a whole-cell recording of a VB neuron in response to GPe axonal stimulation during firing. The cell was recorded with an E_{Cl} = –80 mV pipette internal, which, upon GPe stimulation, decreased in firing. Black horizontal dashed line indicates the baseline firing rate. Red horizontal dashed line indicates the poststimulus firing rate. Bottom left, expanded view of the traces showing evoked burst IPSPs. Blue dots denote the timing of individual IPSPs. In a separate cell, GPe evoked similar burst IPSCs in voltage clamp. Bottom right, Firing response. Wilcoxon test (n = 24 cells, $P = 1.19 \times 10^{-7}$). **(C)** Response map showing the locations of recorded cells (n = 64 cells). Virtually no responders were observed in the VL nucleus. Fisher's exact test (VL vs. VB: $P = 2.67 \times 10^{-7}$).

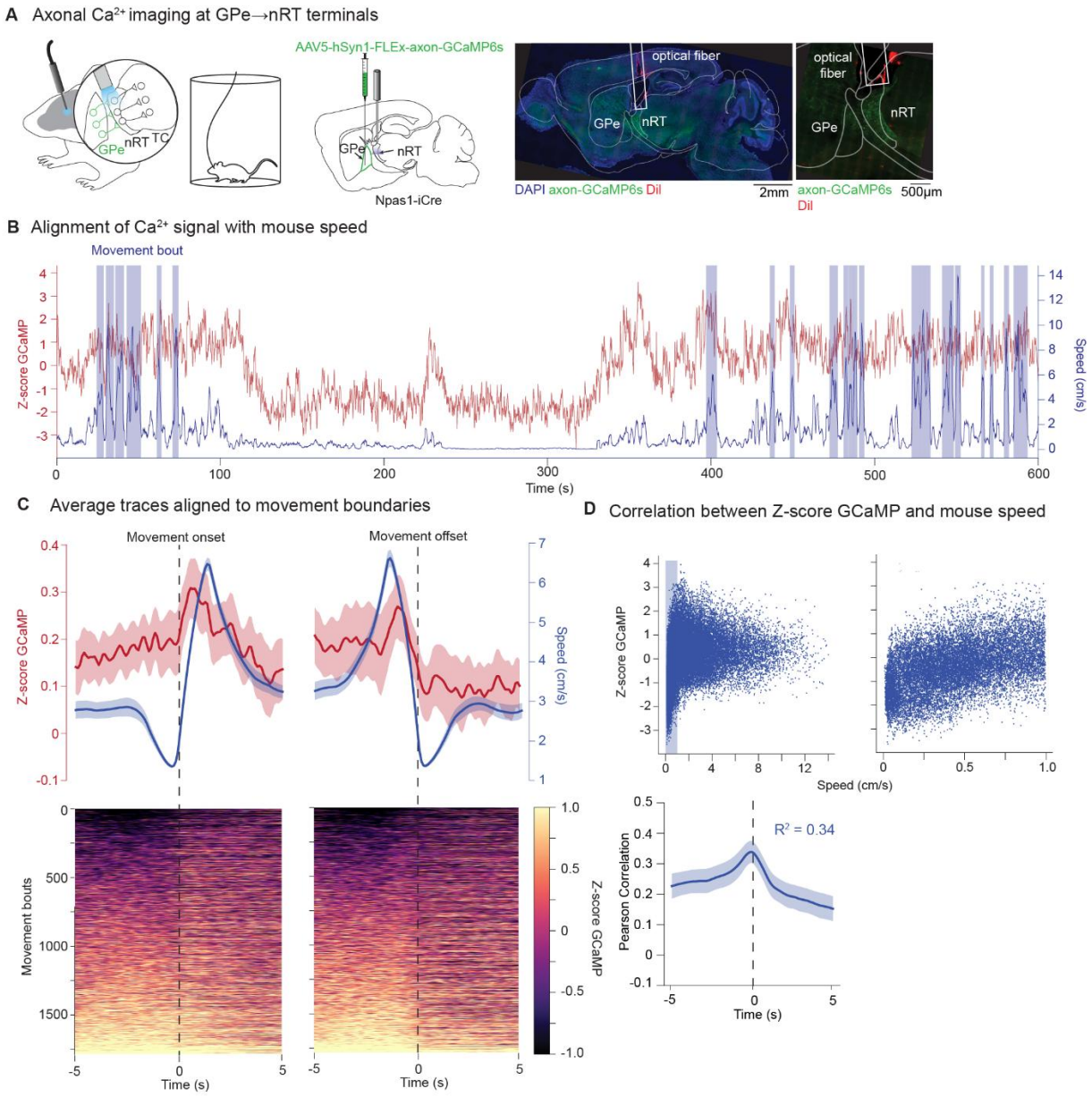

Figure 2.6. ***In vivo*** **activity of GPe→anterior nRT pathway tracks movement states and transitions**

(A) Experimental design. **(B)** Representative trace of mouse speed and Z-score GCaMP over time. Blue boxes indicate individual movement bouts. **(C)** Z-score GCaMP aligned with movement onset (left, *n* = 1812 bouts, *N* = 10 mice) and offset (right, *n* = 1811 bouts, *N* = 10 mice). Top, Mean traces ± SEM. Bottom, Heatmaps of Z-score GCaMP sorted based on pre-onset/offset activity. **(D)** Top, Scatter plot showing the relationship between Z-score GCaMP and mouse speed from one recording. Each marker is one frame (1/10 s). Blue rectangle indicates the speed window (0–1 cm/s) expanded on the right. Bottom, Time-resolved correlation between Z-score GCaMP and mouse speed for the chosen speed window. Mean traces ± SEM.

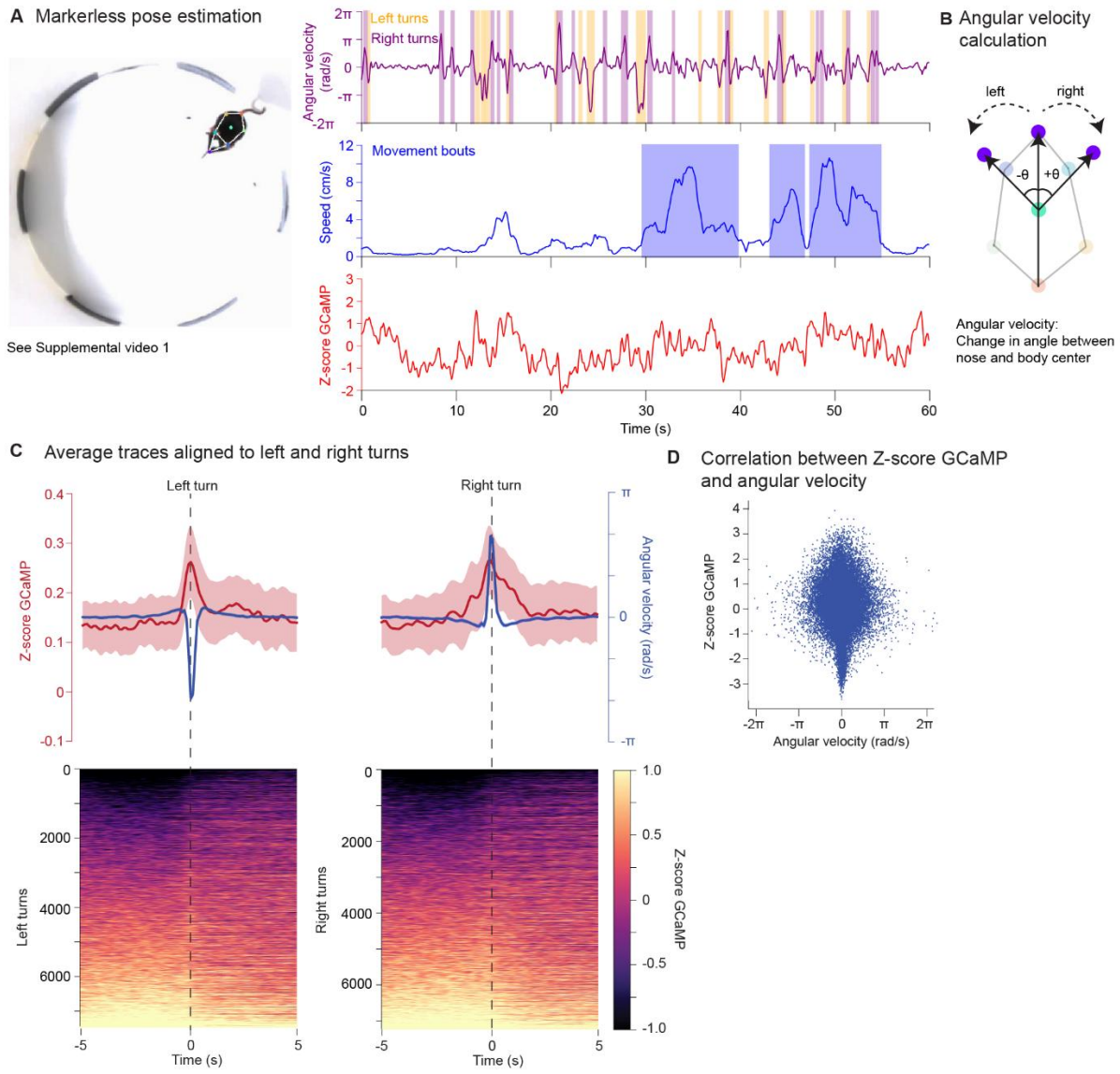

Figure 2.7. Turn-related Ca^{2+} activity at GPe→anterior nRT terminals

(A) Video snapshot of a mouse in an open-field arena tethered to patch cords for fiber photometry. Color circles represent pose estimation markers. Right, Simultaneous tracking of angular velocity, speed, and Ca^{2+} activity in GPe→anterior nRT terminals. **(B)** Illustration of the calculation of angular velocity. **(C)** Z-score GCaMP aligned with left turns (left, *n* = 7434 bouts, *N* = 10 mice) and right turns (right, *n* = 7225 bouts, *N* = 10 mice). Top, Mean traces ± SEM. Bottom, Heatmaps of Z-score GCaMP sorted based on pre-left/right-turn activity. **(D)** Top, Scatter plot showing the relationship between Z-score GCaMP and angular velocity from one recording. Each marker is one frame (1/10 s).

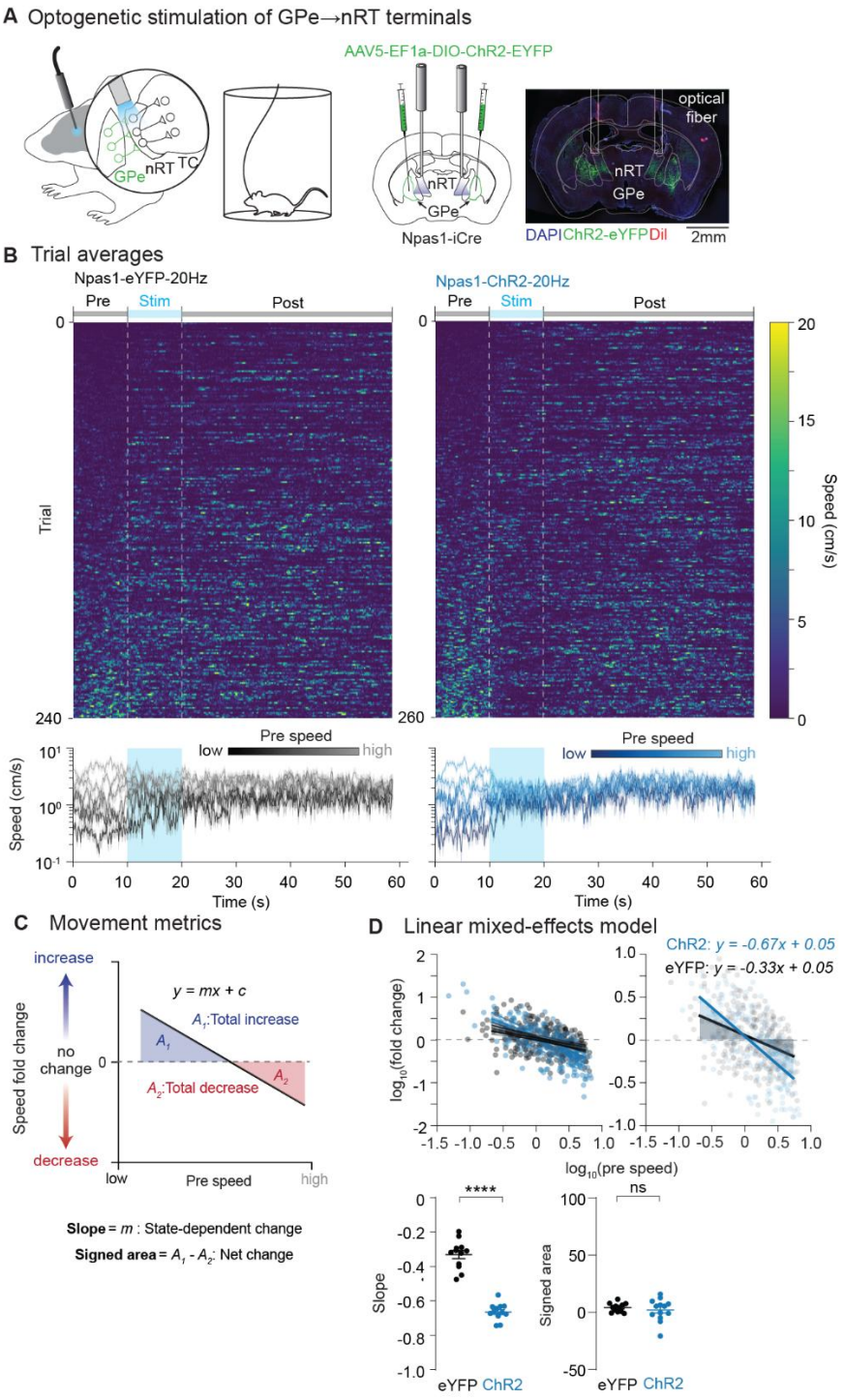

Figure 2.8. Optogenetic stimulation of GPe→anterior nRT terminals bidirectionally modulates speed in a state-dependent manner

(A) Experimental design. **(B)** Top, Heatmaps showing mouse speed across optogenetic manipulation trials of eYFP controls (left, *n* = 240 trials, *N* = 12 mice) and ChR2 groups (right, *n* = 260 trials, *N* = 13 mice), sorted based on prestimulus speed. Vertical lines indicate the timing of light stimulation. Bottom, Mean traces ± SEM grouped by prestimulus speed into six bins:
(Figure caption continued on the next page.)

(Figure caption continued from the previous page.)
[$x<10^{-0.3}$, $[10^{-0.3}\leq x<10^{-0.1}]$, $[10^{-0.1}\leq x<10^{0.1}]$, $[10^{0.1}\leq x<10^{0.3}]$, $[10^{0.3}\leq x<10^{0.5}]$, $[10^{0.5}\leq x]$ (or equivalently, [x<0.50], [0.50≤x<0.79], [0.79≤x<1.26], [1.26≤x<2.00], [2.00≤x<3.16], [3.16≤x]. **(C)** Illustration of speed analysis. We derive two metrics, slope and signed area, from linear mixed-effects models to quantify state-dependent modulation and net change in speed, respectively. **(D)** Top left, Scatter plot showing the relationship between speed fold change ($\log_{10}$ stim/pre speed) and prestimulus speed ($\log_{10}$ pre speed). Each marker is a trial. Lines represent individual mouse fits derived from linear mixed-effects models (see Methods). Lines are plotted over the range spanning the 2.5^{th} to 97.5^{th} percentiles of prestimulus speed. Top right, Same as left, but with an expanded y-axis range. Lines now represent the population-average fit. Bottom, Slopes and signed areas for individual mouse fits. Each marker is a mouse. Statistical results are provided in Table 2.3.

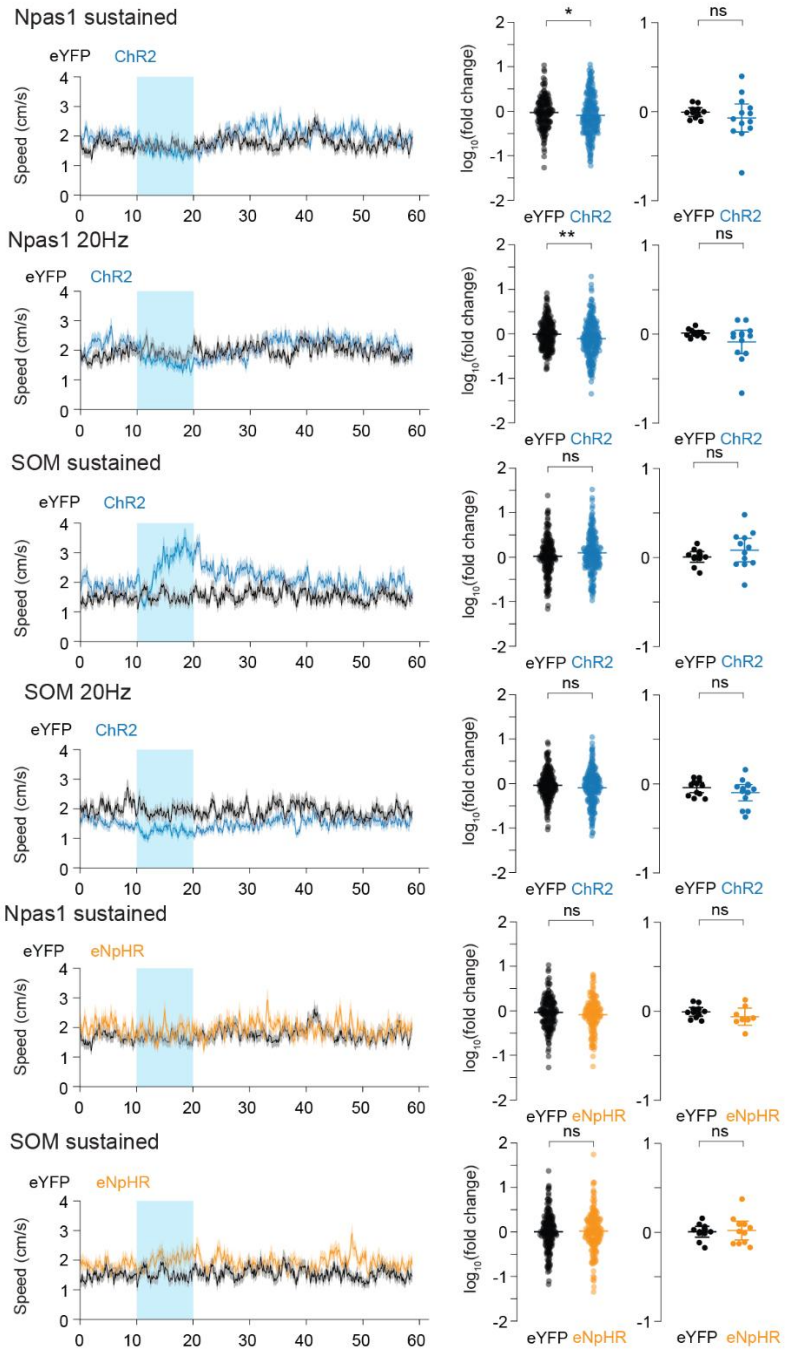

Figure 2.9. Conventional quantification of optogenetic manipulations

Left, Mean traces ± SEM showing mouse speed during optogenetic manipulation trials. Middle, Speed fold changes. Each marker is a trial. Right, Speed fold changes. Each marker is a mouse. Statistical results are provided in Table 2.2.

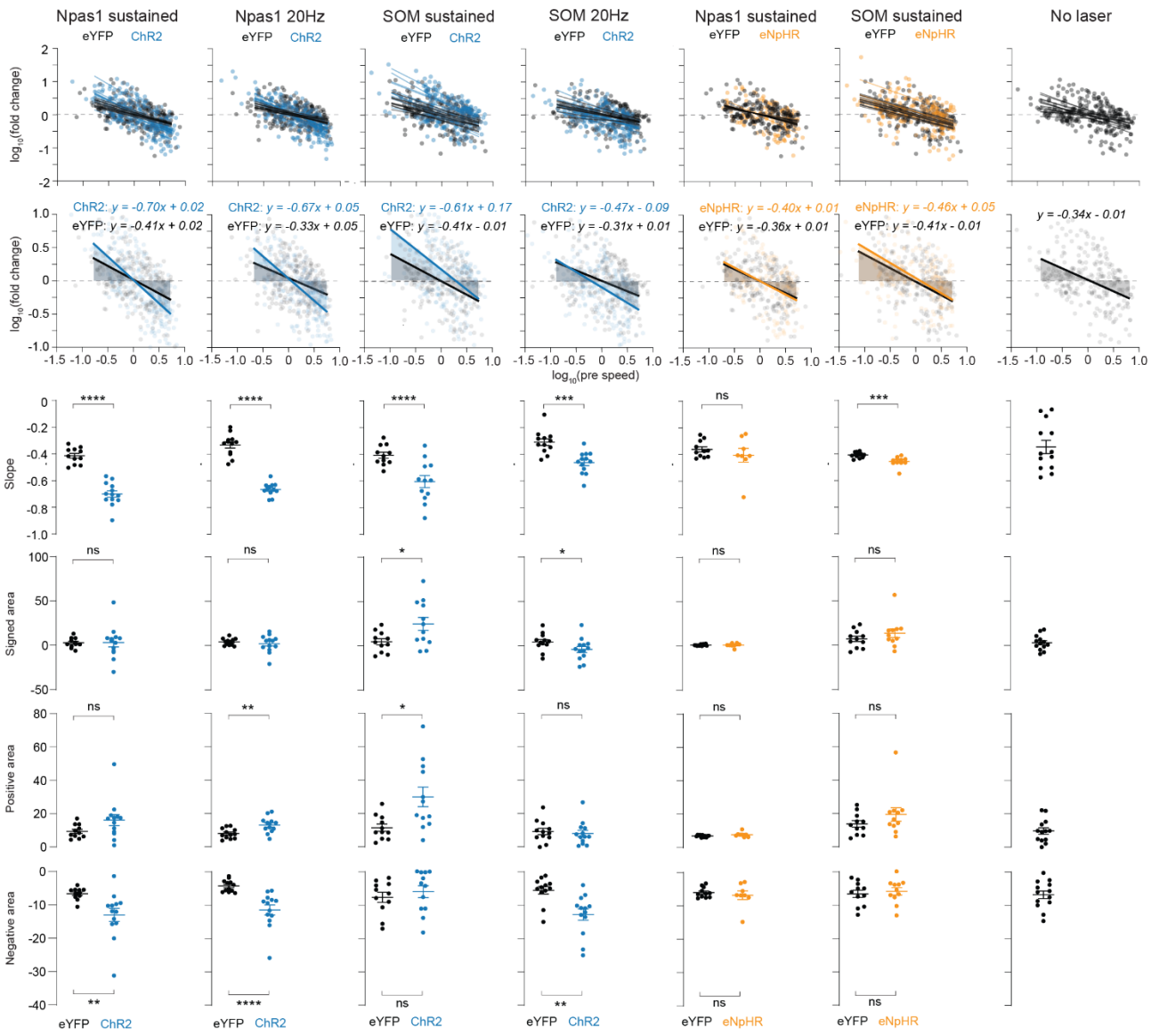

Figure 2.10. State-dependent quantification of optogenetic manipulations

Top row, Scatter plots showing the relationship between speed fold change (log_{10} stim/pre speed) and prestimulus speed (log_{10} pre speed). Each marker is a trial. Lines represent individual mouse fits derived from linear mixed-effects models (see Methods). Lines are plotted over the range spanning the 2.5th to 97.5th percentiles of prestimulus speed. Second row, Same as top, but with an expanded y-axis range. Lines now represent the population-average fit. Third to sixth rows, Slopes, signed areas, positive area, and negative area for individual mouse fits. Each marker is a mouse. Statistical results are provided in Table 2.3

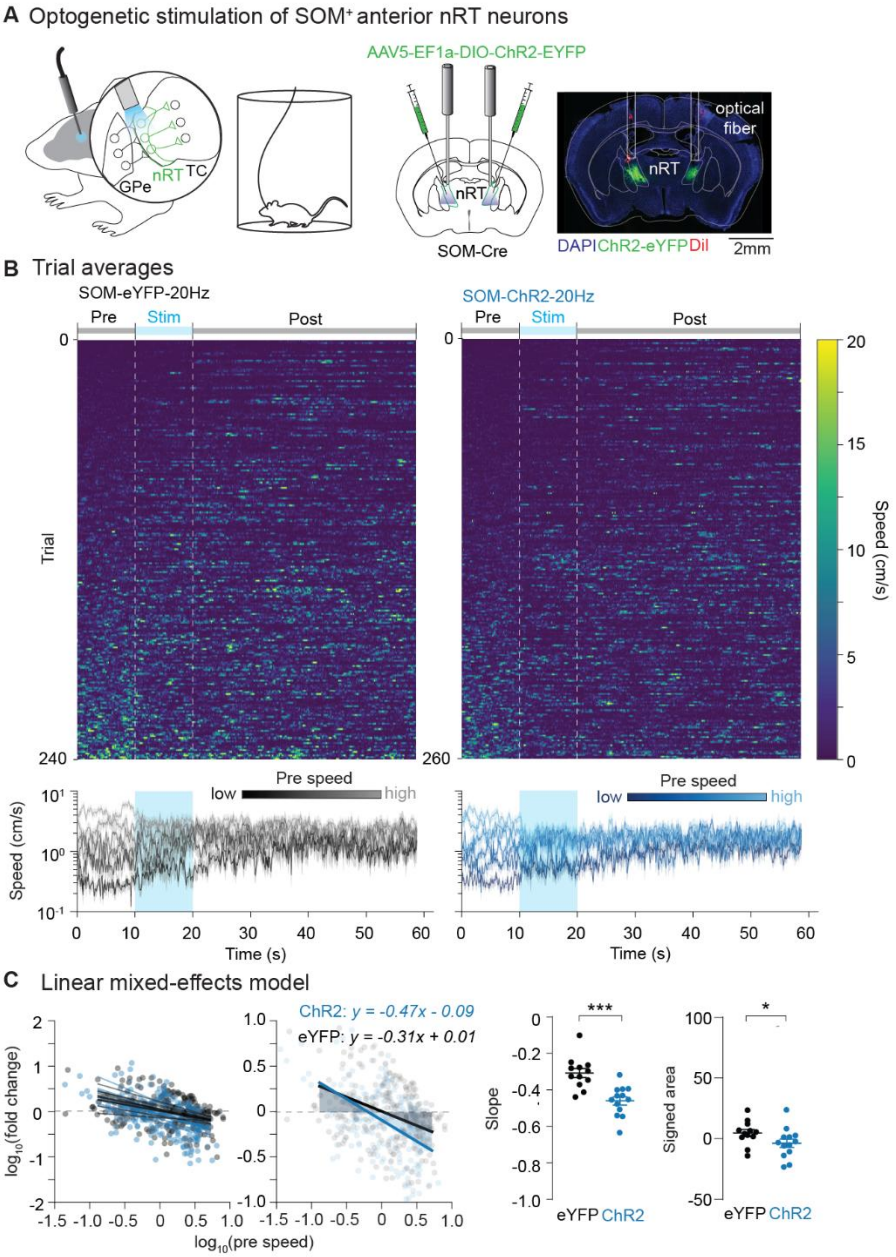

Figure 2.11. Patterned optogenetic stimulation of SOM⁺ anterior nRT neurons suppresses movement

(A) Experimental design. **(B)** Top, Heatmaps showing mouse speed across optogenetic manipulation trials of eYFP controls (left, *n* = 240 trials, *N* = 12 mice) and ChR2 groups (right, *n* = 260 trials, *N* = 13 mice), sorted based on prestimulus speed. Vertical lines indicate the timing of light stimulation. Bottom, Mean traces ± SEM grouped by prestimulus speed into six bins: [$x<10^{-0.3}$, [$10^{-0.3}\leq x<10^{-0.1}$], [$10^{-0.1}\leq x<10^{0.1}$], [$10^{0.1}\leq x<10^{0.3}$], [$10^{0.3}\leq x<10^{0.5}$], [$10^{0.5}\leq x$] (or equivalently, [x<0.50], [0.50≤x<0.79], [0.79≤x<1.26], [1.26≤x<2.00], [2.00≤x<3.16], [3.16≤x]. **(C)** Top left, Scatter plot showing the relationship between speed fold change ($\log_{10}$ stim/pre speed) and prestimulus speed ($\log_{10}$ pre speed). Each marker is a trial. Lines represent individual mouse fits derived from linear mixed-effects models (see Methods). Lines are plotted over the range
(Figure caption continued on the next page.)

(Figure caption continued from the previous page.)
spanning the 2.5th to 97.5th percentiles of prestimulus speed. Top right, Same as left, but with an expanded y-axis range. Lines now represent the population-average fit. Bottom, Slopes and signed areas for individual mouse fits. Each marker is a mouse. Statistical results are provided in Table 2.3

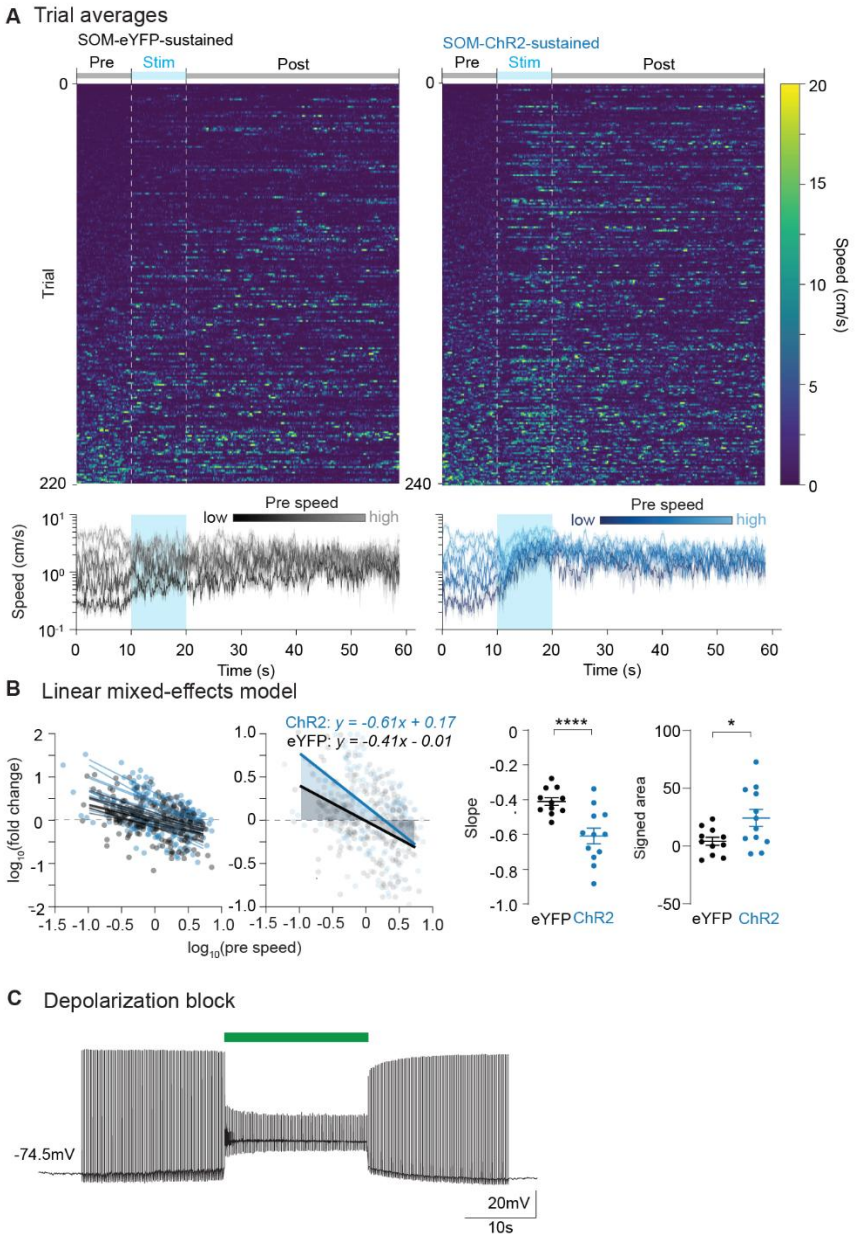

Figure 2.12. Sustained optogenetic stimulation of SOM⁺ anterior nRT neurons promotes movement

(A) Top, Heatmaps showing mouse speed across optogenetic manipulation trials of eYFP controls (left, *n* = 220 trials, *N* = 11 mice) and ChR2 groups (right, *n* = 240 trials, *N* = 12 mice), sorted based on prestimulus speed. Vertical lines indicate the timing of light stimulation. Bottom, Mean traces ± SEM grouped by prestimulus speed into six bins: [$x<10^{-0.3}$, [$10^{-0.3}\leq x<10^{-0.1}$], [$10^{-0.1}\leq x<10^{0.1}$], [$10^{0.1}\leq x<10^{0.3}$], [$10^{0.3}\leq x<10^{0.5}$], [$10^{0.5}\leq x$] (or equivalently, [x<0.50], [0.50≤x<0.79], [0.79≤x<1.26], [1.26≤x<2.00], [2.00≤x<3.16], [3.16≤x]. **(B)** Top left, Scatter plot showing the relationship between speed fold change ($\log_{10}$ stim/pre speed) and prestimulus speed ($\log_{10}$ pre speed). Each marker is a trial. Lines represent individual mouse fits derived from linear mixed-effects models (see Methods). Lines are plotted over the range spanning the 2.5th to 97.5th
(Figure caption continued on the next page.)

(Figure caption continued from the previous page.)
percentiles of prestimulus speed. Top right, Same as left, but with an expanded y-axis range. Lines now represent the population-average fit. Bottom, Slopes and signed areas for individual mouse fits. Each marker is a mouse. Statistical results are provided in Table 2.3. **(C)** Representative trace showing depolarization block in an active SOM^+ anterior nRT neuron subject to sustained ChR2 activation.

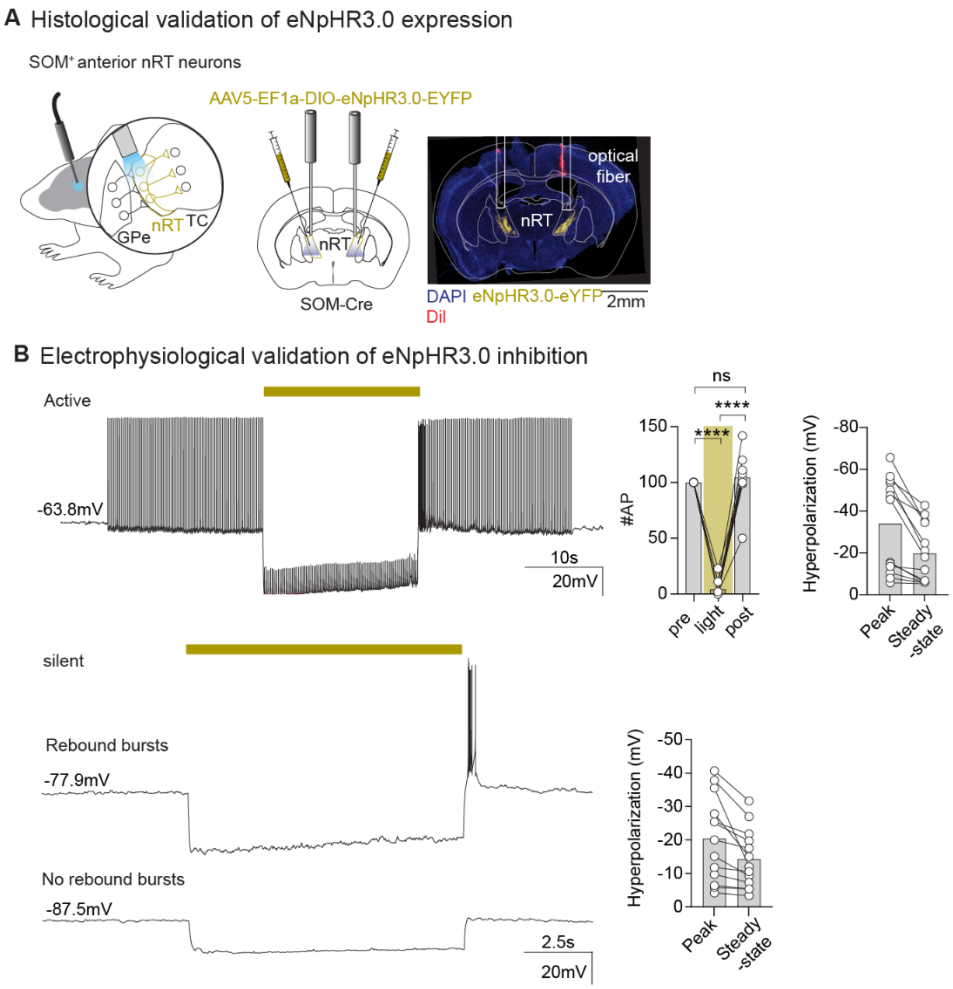

Figure 2.13. Histological and electrophysiological assessment of eNpHR3.0 expression and function

(A) Experimental design for optogenetic inhibition of SOM$^+$ anterior nRT neurons. **(B)** Top left, Representative traces showing suppression of firing in an active SOM$^+$ anterior nRT neuron in response to eNpHR3.0 inhibition. Top Right, Reduction of action potentials and membrane hyperpolarization by eNpHR3.0 inhibition. Friedman test (n = 13 cells, $P = 4.45 \times 10^{-5}$). Dunn's multiple comparisons test (pre vs. light: $P = 8.56 \times 10^{-4}$; pre vs. post: $P > 0.99$; light vs. post: $P = 1.74 \times 10^{-4}$). Bottom left, Representative traces showing hyperpolarization in a silent SOM$^+$ anterior nRT neuron in response to eNpHR3.0 inhibition. Rebound bursts were observed in some cells. Bottom right, membrane hyperpolarization induced by eNpHR3.0 inhibition.

2.7. Tables

Table 2.1. Summary statistics

Figure	Group analysis	P-value	Comparisons	Pairwise analysis	P-value	Sample size
1e Right	–	–	AP	Linear regression	0.5961	n = 41 cells
			ML		0.9900	
			DV		0.6047	
2c	–	–	Pr2/Pr1	Linear regression	0.1097	n =29 cells
3c	Kruskal-Wallis test with firing response (Increase, No change, Decrease) as column factors	0.9362	Increase vs. No change	Dunn's multiple comparisons test	>0.9999	n = 50 cells
			Increase vs. Decrease		>0.9999	
			No change vs. Decrease		>0.9999	
3d Top Right	–	–	AP: Increase	Linear regression	1.337×10^{-4}	n = 61 cells
			AP: No change		0.1650	
			AP: Decrease		2.680×10^{-3}	
3d Middle Right	–	–	ML: Increase		2.410×10^{-4}	
			ML: No change		0.1805	
			ML: Decrease		5.100×10^{-3}	
3d Bottom Right	–	–	DV: Increase		0.3863	
			DV: No change		0.8839	
			DV: Decrease		7.442×10^{-3}	
3e Right	–	–	AP	Linear regression	$<1.00 \times 10^{-10}$	n = 5 mice
			ML		$<1.00 \times 10^{-10}$	
			DV		0.4971	
3f Left	–	–	no VU vs. with VU	Fisher's exact test	1.908×10^{-4}	n = 33 cells
4a Bottom Right	Kruskal-Wallis test with firing response (Increase, No change, Decrease) as column factors	2.305×10^{-2}	Increase vs. No change	Dunn's multiple comparisons test	0.2265	n = 19 cells
			Increase vs. Decrease		2.541×10^{-2}	
			No change vs. Decrease		0.8334	
4b Right	–	–	AP	Linear regression	4.420×10^{-3}	n = 19 cells
			ML		2.098×10^{-2}	
			DV		2.213×10^{-2}	
4d Top	–	–	-60mV, No stim vs. Stim	Wilcoxon test	0.4319	n = 21 cells
			-70mV, No stim vs. Stim		2.384×10^{-7}	n = 23 cells
			-80mV, No stim vs. Stim		4.768×10^{-7}	n = 22 cells
4d Bottom	–	–	-60mV	Linear regression	1.607×10^{-2}	n = 17 cells
			-70mV		0.7981	n = 22 cells
			-80mV		0.7740	n = 19 cells
4e Bottom Left	Mixed ANOVA with command voltage (-105mV to -40 mV) as row factors and ECl internals (-60mV, -70mV, -80mV) as column factors	Command voltage: $< 1.000 \times 10^{-10}$ ECl internals: 5.541×10^{-4}	–	–	–	n = 60 cells
4e Bottom Right	Kruskal-Wallis test with ECl internals (-60mV, -70mV, -80mV) as column factors	1.146×10^{-5}	-60mV vs. -70mV	Dunn's multiple comparisons test	2.227×10^{-3}	n = 64 cells
			-60mV vs. -80mV		9.621×10^{-6}	
			-70mV vs. -80mV		0.3075	
4f Bottom	RM two-way ANOVA with membrane potential (-120mV to -40mV) as row factors and ECl internals as (-60mV, -70mV, -80mV) as column factors	command voltage: 6.047×10^{-6} ECl internals: 2.681×10^{-5}	–	–	–	n = 68 cells
5b Bottom Right	–	–	-80mV, No stim vs. Stim	Wilcoxon test	1.192×10^{-7}	n = 24 cells
5c Bottom	–	–	VL vs. VB	Fisher's exact test	2.669×10^{-7}	n = 52 cells
8	See Table 3					
9	See Table 2					
10	See Table 3					
11						
12						
13b Top Right	Friedman test	4.452×10^{-5}	pre vs. light	Dunn's multiple comparisons test	8.564×10^{-4}	n = 13 cells
			pre vs. post		>0.9999	
			light vs. post		1.743×10^{-4}	

Table 2.2. Conventional quantification of optogenetic manipulations

Data are presented as geometric mean [Lower 95% confidence interval – Upper 95% confidence interval]. P-values indicate significance from a Mann–Whitney test.

Mouse line	Npas1-iCre				SOM-Cre				Npas1-iCre		SOM-Cre	
Stimulation site	GPe->nRT axons				nRT cell bodies				GPe->nRT axons		nRT cell bodies	
Stim paradigm	Sustained		20Hz		Sustained		20Hz		Sustained			
Conditon	eYFP	ChR2	eYFP	ChR2	eYFP	ChR2	eYFP	ChR2	eYFP	eNpHR	eYFP	eNpHR
Trial averages												
Log(Speed fold change)	0.99 [0.89 – 1.11]	0.85 [0.75 – 0.97]	1.04 [0.95 – 1.14]	0.83 [0.74 – 0.93]	1.03 [0.91 – 1.16]	1.22 [1.08 – 1.39]	0.92 [0.83 – 1.01]	0.80 [0.72 – 0.90]	0.99 [0.89 – 1.11]	0.88 [0.77 – 1.01]	1.03 [0.91 – 1.16]	1.06 [0.93 – 1.21]
p-value	**4.34×10^{-2}**		**3.68×10^{-3}**		0.13		0.22		0.24		0.77	
n, trials	220	260	240	260	220	240	240	260	160	260	220	220
Mouse averages												
Comparison	eYFP(reference) vs ChR2								eYFP(reference) vs eNpHR			
Log(Speed fold change)	0.99 [0.89 – 1.11]	0.85 [0.59 – 1.23]	1.04 [0.98 – 1.11]	0.83 [0.61 – 1.12]	1.03 [0.89 – 1.18]	1.22 [0.90 – 1.66]	0.92 [0.80 – 1.04]	0.80 [0.65 – 0.99]	0.99 [0.89 – 1.11]	0.88 [0.70 – 1.10]	1.03 [0.89 – 1.18]	1.06 [0.83 – 1.35]
p-value	0.28		0.17		0.38		0.41		0.27		0.85	
N, mice	11	13	12	13	11	12	12	13	8	13	11	11

Table 2.3. State-dependent quantification of optogenetic manipulations

Data are presented as mean ± SEM.
* Indicates significance for whether the slope/intercept differs from zero.
† Indicates significance for whether the slope/intercept differs from the eYFP group.
‡ Indicates significance from a Mann–Whitney test.

Mouse line	Npas1-iCre				SOM-Cre				Npas1-iCre		SOM-Cre	
Stimulation site	GPe->nRT axons				nRT cell bodies				GPe->nRT axons		nRT cell bodies	
Stim paradigm	Sustained		20Hz		Sustained		20Hz		Sustained			
Conditon	eYFP	ChR2	eYFP	ChR2	eYFP	ChR2	eYFP	ChR2	eYFP	eNpHR	eYFP	eNpHR
Input data												
Pre speed (cm/s)	1.67 ± 0.10	1.96 ± 0.10	1.85 ± 0.09	2.20 ± 0.10	1.48 ± 0.10	1.89 ± 0.10	2.04 ± 0.11	1.54 ± 0.08	1.67 ± 0.10	2.02 ± 0.11	1.48 ± 0.10	1.83 ± 0.10
Log(Pre speed)	0.03 ± 0.03	0.12 ± 0.03	0.11 ± 0.03	0.19 ± 0.03	-0.05 ± 0.03	0.12 ± 0.03	0.12 ± 0.03	0.01 ± 0.03	0.03 ± 0.03	0.17 ± 0.03	-0.05 ± 0.03	0.03 ± 0.03
Log(Speed fold change)	-0.00 ± 0.02	-0.07 ± 0.03	0.02 ± 0.02	-0.08 ± 0.03	0.01 ± 0.03	0.09 ± 0.03	-0.04 ± 0.02	-0.09 ± 0.02	-0.00 ± 0.02	-0.06 ± 0.03	0.01 ± 0.03	0.03 ± 0.03
β fixed-effects coefficients from LMM												
Comparison	eYFP(reference) vs ChR2								eYFP(reference) vs eNpHR			
β0 (eYFP intercept)	0.018 ± 0.051		0.052 ± 0.033		-0.010 ± 0.067		0.011 ± 0.044		0.010 ± 0.027		-0.009 ± 0.051	
p-value*	0.722		0.113		0.883		0.798		0.703		0.855	
β1 (intercept shift relative to eYFP)	-0.003 ± 0.069		-0.006 ± 0.047		0.178 ± 0.093		-0.097 ± 0.059		0.000 ± 0.039		0.055 ± 0.072	
p-value†	0.966		0.899		0.056		0.999		0.992		0.447	
β2 (eYFP slope)	-0.415 ± 0.065		-0.333 ± 0.059		-0.411 ± 0.074		-0.313 ± 0.067		-0.360 ± 0.073		-0.409 ± 0.052	
p-value*	**<0.001**		**<0.001**		**<0.001**		**<0.001**		**<0.001**		**<0.001**	
β3 (slope shift relative to eYFP)	-0.288 ± 0.087		-0.335 ± 0.082		-0.197 ± 0.110		-0.153 ± 0.089		-0.044 ± 0.112		-0.048 ± 0.077	
p-value†	**0.001**		**<0.001**		0.073		0.085		0.085		0.530	
Mouse-level derived metrics												
Conditon	eYFP	ChR2	eYFP	ChR2	eYFP	ChR2	eYFP	ChR2	eYFP	eNpHR	eYFP	eNpHR
Slope	-0.41 ± 0.02	-0.33 ± 0.02	-0.33 ± 0.02	-0.67 ± 0.01	-0.41 ± 0.02	-0.61 ± 0.05	-0.31 ± 0.02	-0.47 ± 0.02	-0.36 ± 0.02	-0.40 ± 0.05	-0.41 ± 0.01	-0.46 ± 0.01
p value‡	**8.01×10^{-7}**		**3.84×10^{-7}**		**9.81×10^{-8}**		**1.94×10^{-4}**		0.66		**3.94×10^{-4}**	
Signed area	2.79 ± 1.69	3.17 ± 5.07	3.77 ± 1.12	1.71 ± 2.69	3.91 ± 3.49	24.09 ± 7.34	3.72 ± 2.89	-4.72 ± 3.45	0.90 ± 0.29	0.93 ± 0.79	7.22 ± 3.01	13.65 ± 4.99
p value‡	>0.99		0.65		**4.39×10^{-2}**		**4.57×10^{-2}**		0.40		0.37	
Positive area	9.45 ± 1.23	16.20 ± 3.30	8.14 ± 0.88	13.25 ± 1.28	11.66 ± 2.16	30.14 ± 5.88	9.36 ± 1.88	8.79 ± 1.95	6.87 ± 0.18	7.70 ± 0.51	13.92 ± 1.95	19.61 ± 4.05
p value‡	5.48×10^{-2}		**4.50×10^{-3}**		**1.05×10^{-2}**		0.61		6.20×10^{-2}		0.33	
Negative area	-6.66 ± 0.54	-13.02 ± 1.97	-4.37 ± 0.51	-11.54 ± 1.49	-7.75 ± 1.53	-6.05 ± 1.81	-5.64 ± 1.15	-12.90 ± 1.70	-5.96 ± 0.54	-6.78 ± 1.30	-6.70 ± 1.09	-5.96 ± 1.10
p value‡	**1.20×10^{-3}**		**1.15×10^{-6}**		0.38		**1.94×10^{-3}**		0.97		0.70	
n, trials	220	260	240	260	220	240	240	260	160	260	220	220
N, mice	11	13	12	13	11	12	12	13	8	13	11	11

Chapter 3: Distinct Firing Responses to Synthetic Synaptic Currents in the Adult Murine Reticular and Relay Thalamus

3.1. Abstract

Numerous cortical and subcortical inputs innervate the thalamus and robustly control thalamic activity. These synaptic inputs differ in shape and undergo dynamic changes throughout development and disease conditions. How the shape of postsynaptic currents regulates thalamic neuronal firing has been studied mainly in young rodents with immature neural development and function. Here, we use adult mice with mature intrinsic excitability to address this question in two compartments of the thalamus—the nucleus reticularis thalami (nRT) and thalamocortical (TC) relay nuclei. Using whole-cell patch-clamp electrophysiology, we simulated synthetic inhibitory (IPSCs) and synthetic excitatory postsynaptic currents (EPSCs), injected them in nRT and TC neurons, and examined how changes in their shape parameters regulated neuronal firing in different electrical states. We found that in response to synthetic IPSCs, TC neurons initiate low-threshold spikes (LTSs) earlier than nRT neurons, and the amplitude of IPSCs regulates the probability of initiating an LTS while the duration of IPSCs regulates the timing at which the LTS initiates. These results show that in the adult thalamus, LTS is regulated by IPSCs similarly to what has been reported for the immature thalamus. In addition, sharp driver-like EPSCs evoke more firing when nRT and TC neurons are silent; whereas slow modulator-like EPSCs evoke more firing when nRT and TC neurons are active. Critically, we have generated a quantitative map of how features of synaptic currents shape neuronal firing in relationship with activity states.

3.2. Introduction

Known as the “Gateway to the Cortex” (*25*), the thalamus is a key brain structure that integrates visual, auditory, sensory, motor, and limbic inputs from subcortical structures and transmits them to the cortex. The thalamus consists of a GABAergic shell (*89*), termed the nucleus

reticularis thalami (nRT), wrapped around glutamatergic nuclei that project to cortical regions, termed thalamocortical (TC) relay nuclei. The nRT and TC neurons receive synaptic inputs from both cortical and subcortical origins. Notably, nRT neurons send powerful GABAergic inhibitory inputs to TC neurons and receive glutamatergic excitatory inputs from TC neurons (*90*). These reciprocal connections regulate oscillatory activity in the thalamus (*57*). In addition, nRT neurons receive glutamatergic excitatory inputs from the cortex and amygdala (*57*), GABAergic input from the external globus pallidus (*57*), and the substantia nigra pars reticulata (*91*–*93*). TC neurons receive excitatory glutamatergic inputs from the neocortex and ascending inputs from their respective modalities [e.g., excitatory retinal input for the visual thalamus (*94*) and inhibitory basal ganglia input for the motor thalamus (*95*)].

Kinetic properties of synaptic currents can impact neuronal firing. For glutamatergic synapses, fast (5–10 ms) synaptic currents produced by ionotropic receptors are typically associated with driver roles; slow synaptic currents (hundreds of milliseconds to seconds) are typically associated with modulator roles (*96*–*98*). Drivers are inputs that synapse onto proximal dendrites and reliably evoke spikes in thalamic neurons; modulators are inputs that synapse primarily onto distal dendrites and control the probability of cortical transmission (for review, see Refs. 10, 12). Driver inputs such as those mediated by ionotropic AMPA receptors in the nRT have a decay time constant as fast as 0.76 ms (*99*). On the other hand, modulator inputs activated through mGluR (*100*) or AChR (*101*) in the nRT produce slow depolarizations for up to minutes.

The kinetics of synaptic currents can change during development and disease conditions. For example, fast glutamatergic currents at the cortico-nRT synapse, mediated by the GluR4 AMPA receptor, play a key role in the feedforward inhibition in the cortico-nRT-TC circuit (*99*). The loss of these fast currents at the cortico-nRT synapse leads to neurodevelopmental disorders associated with absence epilepsy (*99*). Understanding how changes in synaptic currents regulate neuronal firing provides crucial insights into rhythmogenesis in the thalamus in both normal and pathological conditions.

Careful studies using dynamic clamp or programmed current clamp protocols showed how distinct synaptic conductances [e.g., GABA (*102*–*107*), AMPA (*106*), NMDA (*106*)] and intrinsic conductances [e.g., transient Ca2+ current (IT) and hyperpolarization-activated cation current (Ih) (*108*)] affect neuronal firing in the developing thalamus. All these conductances were found to regulate different aspects of the timing and features (e.g., duration) of low-threshold spike (LTS) activation in both the nRT and TC neurons and modulate thalamic network oscillations. However, most studies were conducted in young rodents, not adult mice.

In this study, we investigated how the shape parameters (i.e., amplitude, duration, and charge) of synthetic synaptic currents regulate the activity patterns of nRT and TC neurons in adult mice and how their responses vary depending on the state of neuronal activity.

3.3. Results

A postsynaptic current can be simplified as a triangular waveform characterized by two main parameters: amplitude (height) and duration (width). Charge (area) is a function of amplitude and duration. We describe a sharp brief current (high amplitude, low duration) as a driver-like current; a slow prolonged current (low amplitude, high duration) as a modulator-like current; negative hyperpolarizing currents as inhibitory postsynaptic currents (IPSCs); and positive depolarizing currents as excitatory postsynaptic currents (EPSCs). Triangular current waveforms can be used to simulate synaptic currents with rapid onset and gradual decay. For example, in the nRT, a train of consecutive GABAA currents can be modeled as a triangle with an onset of ~10 ms and a decay of ~500 ms with a peak current ~180 pA (*109*), and a train of GABAB currents as a triangle with an onset of ~100 ms and a decay of ~1,000 ms with a peak current of ~150 pA (*102*). The triangular current waveforms used in this study in current clamp have instantaneous onsets, amplitudes, and decay durations in these ranges. These waveforms result in hyperpolarizations (or depolarizations), similar to those evoked by dynamic clamp in the studies cited above. To quantify how changes in shape parameters of IPSCs and EPSCs affect neuronal

firing, we simulated synthetic synaptic currents by injecting currents of triangular waveforms during the recording of nRT and TC neurons **(Fig. 3.1A)**. To isolate the effect on firing by the synthetic synaptic currents without contamination of spontaneous postsynaptic currents, we applied DNQX to block AMPA receptor-mediated currents, APV to block NMDA receptor-mediated currents, and picrotoxin to block GABAA receptor-mediated currents.

We sampled TC neurons across the somatosensory ventrobasal (VB) nucleus and the motor ventrolateral (VL) nucleus and found no significant differences in the firing response characteristics **(Fig. 3.5)**, passive membrane properties, and action potential characteristics between VB and VL neurons **(Table 3.1)**. As such, for comparison with nRT neurons, data from VB and VL neurons are combined into a single group (i.e., TC neurons) for all analyses.

TC Neurons Initiate LTS Earlier than nRT Neurons in Response to IPSCs

To mimic the effect of firing inhibition from an incoming synaptic IPSC during activity, we first injected synthetic IPSCs amid sustained suprathreshold depolarizing current injections. Synthetic IPSCs inhibited firing in nRT neurons, similar to activating afferents from local inhibitory collaterals in the nRT (*110*) **(Fig. 3.1, A to D)**. The amplitudes of synthetic IPSCs used range from 0 to 450 pA and are capable of generating hyperpolarizations up to –100 mV, reaching the physiological K^+-dependent $GABA_B$ reversal potential in the nRT (*111*) and TC (*112*) neurons. We varied the amplitude and duration of synthetic IPSCs and used the time to the first action potential recovery to measure the duration of the firing inhibition. The duration of firing inhibition scaled with the duration of synthetic IPSCs in both nRT and TC neurons **(Fig. 3.1E, Middle)**. However, the duration of firing inhibition scaled with the amplitude of synthetic IPSCs in nRT neurons, but not in TC neurons, which initiated LTS before the full decay of the synthetic IPSC, beyond a certain amplitude threshold during firing **(Fig. 3.1E, Left)**. This finding in adult mice aligns with previous studies in young rats showing that, in response to simulated GABA conductances, the onset of LTS is considerably delayed in nRT neurons compared with TC neurons (*102*, *103*). At small and

moderate synthetic IPSC amplitudes where LTS are not initiated, TC neurons exhibit more delayed action potential resumption compared with nRT neurons, suggesting that TC neurons are more susceptible to firing inhibition.

What could account for the earlier initiation of LTS in TC neurons, compared with nRT neurons? We quantified the passive membrane properties and action potential characteristics of nRT and TC neurons **(Table 3.1)** and found no significant correlations between these properties and the time to LTS **(Table 3.2)**, suggesting that differences in these properties do not explain why TC neurons initiate LTS earlier than nRT neurons. We speculate that the most likely mechanism underlying this phenomenon is the differential expression of intrinsic membrane currents, i.e., I_h and I_T currents in nRT and TC neurons, as they have been shown to critically regulate the timing and features of LTS generation (*113*) (see Discussion).

Next, we varied the amplitude and duration of synthetic IPSCs but kept the total charge of the synthetic IPSCs constant. We asked, given the same total charge, what parameters of synthetic IPSCs most effectively inhibit firing in nRT and TC neurons. We found that a duration/amplitude ratio of 3.31 ± 0.38 and 3.53 ± 0.68 (or, when considering duration alone, 450.00 ± 21.89 ms and 462.50 ± 33.39 ms) maximally inhibited firing in both nRT and TC neurons, respectively **(Fig. 3.1E, Right)**. The duration/amplitude ratio can be interpreted as a metric for the shape of the synthetic current. An optimal ratio signifies a preferred shape that maximally inhibits firing given the same total charge. The optimal ratios were not significantly different between nRT and TC neurons (Mann–Whitney test, $P = 0.72$ for duration/amplitude ratio, $P = 0.75$ for duration alone). Deviations from this optimal ratio may signify inefficiency in charge transfer.

IPSC Amplitude Controls The Probability of LTS Initiation; IPSC Duration Controls The Timing of LTS Initiation

Next, we sought to characterize how nRT and TC neurons respond to synthetic IPSCs at rest (i.e., when they are silent). nRT and TC neurons were generally quiet in brain slices, and no

specific manipulation was needed to maintain cells in a state of silence. Similar to the approach described above for active states, we measured the time to LTS in nRT and TC neurons while varying the amplitude and duration of synthetic IPSCs **(Fig. 3.2A and B)**. We first varied the synthetic IPSC amplitude. The probability of initiating an LTS increased with increasing synthetic IPSC amplitude in both cell types **(Fig. 3.2C)**. However, the timing of the LTS remained the same regardless of IPSC amplitude **(Fig. 3.2D)**. A small percentage of nRT (3/20, 15%) and TC (1/18, 5.56%) neurons did not initiate an LTS even when strongly hyperpolarized by synthetic IPSCs of large amplitudes. The nonresponding cells in the nRT were presumably somatostatin-positive nRT neurons, which exhibit smaller peak I_T compared with parvalbumin-positive nRT neurons (*57*).

Next, we varied the synthetic IPSC duration in the same cells. The onset of LTS was delayed with increasing synthetic IPSC duration in both cell types **(Fig. 3.2D)**. Consistent with our previous experiment, in both conditions, TC neurons produced LTS before the full decay of synthetic IPSCs, whereas nRT neurons produced LTS after the synthetic IPSC had fully decayed **(Fig. 3.2D)**. The times to LTS in nRT neurons and TC neurons are 465.37 ± 26.47 ms and 378.75 ± 11.41 ms and are significantly different (Mann–Whitney test, $P = 1.00 \times 10^{-3}$).

Altogether, our results suggest that the initiation of LTS in response to synthetic IPSCs happens earlier in TC neurons than in nRT neurons, and this is a conserved feature across activity states.

Sharp Driver-Like EPSCs Evoke More Firing When nRT and TC Neurons are Silent; Slow Modulator-Like EPSCs Evoke More Firing When nRT and TC Neurons are Active

Finally, we asked how nRT and TC neurons respond to depolarizing synthetic EPSCs during activity and silence. During firing, the number of action potentials evoked increased with injections of synthetic EPSCs of increasing amplitude and duration in nRT neurons, and to a lesser extent, in TC neurons **(Fig. 3.3A, B and D)**. The same phenomenon was observed when

nRT and TC responded to synthetic EPSCs at rest **(Fig. 3.4 A, B and D)**. The lower excitability of TC neurons compared with nRT neurons could be explained in part by the fact that TC neurons exhibit lower input resistance and more hyperpolarized membrane potential **(Table 3.1)** due to the expression of K^+ channels such as TWIK-related acid-sensitive K^+ channel 1 (TASK1) and TASK3 (*114*, *115*).

When the total charge of the synthetic EPSC was kept constant, while varying the synthetic EPSC amplitude and duration, we found that, at rest, fast, driver-like EPSCs evoked more firing than slow, modulator-like EPSCs in both nRT and TC neurons **(Fig. 3.3B and D)**. Notably, the opposite was true when neurons were active—a slow modulator-like EPSC was more efficient in evoking firing than a fast, driver-like EPSC in both nRT and TC neurons during activity **(Fig. 3.4B and D)**. A potential explanation for these results is that when the neuron is silent and resting relatively hyperpolarized, a driver-like EPSC of large amplitude activates T-type Ca^{2+} channels more efficiently than a modulator-like EPSC of small amplitude, leading to more LTS crowned with Na^+ action potentials.

3.4. Discussion

Our first finding, that TC neurons initiate LTS earlier than nRT neurons in adult mice, corroborates with previous work in young rodents (*102*, *103*), suggesting this is a broadly conserved feature across ages. This observation remains true across activity states, regardless of whether the neuron is active or at rest. Two possible mechanisms could underlie this phenomenon: *1*) activation of I_h in TC neurons, which accelerates membrane depolarization to initiate LTS. The possibility of I_h is excluded in earlier work, which shows that bath application of Cs^{2+}, which blocks I_h, does not affect the onset of LTS in TC or nRT neurons (*103*). *2*) A depolarizing shift in the voltage threshold for LTS generation in nRT neurons. Indeed, nRT neurons exhibit distinct T-type Ca^{2+} channel (i.e., $Ca_V3.3$), which exhibits slower activation and inactivation kinetics (approximately twice as slow within the LTS generation range of –60 mV to –

40 mV), and a more depolarized activation threshold (–50 mV vs. –59 mV) compared with those of TC neurons (i.e., $Ca_V3.1$) (*55*). Therefore, the differential expression of T-type Ca^{2+} channels, but not I_h, likely explains the difference in the onset of LTS between TC and nRT neurons. An important implication of this difference is that IPSCs generated from intra-nRT and nRT-TC connections could result in different oscillatory frequencies in the nRT and TC nuclei. When an active nRT neuron evokes an IPSC in a connected nRT neuron and TC neuron, the resulting LTS will be considerably delayed in the nRT neuron than in the TC neuron. At a network level, this implies that oscillations within intra-nRT connections would be slower than oscillations within nRT-TC connections due to the longer interval between the IPSCs and LTS generation. Previous in vivo studies in rats showed that the deafferented nRT could generate 7–14 Hz spindle-like oscillations in the slow frequency range via its intra-nRT connections (*116*). This spindle oscillation in nRT, according to modeling studies, could initiate spindle oscillations in the nRT-TC network (*117*). However, it remains to be determined empirically whether intra-nRT and nRT-TC networks could operate at distinct frequencies.

We also showed that at rest, IPSC amplitude and duration separately control LTS initiation probability and timing. Contrary to this, a previous study in young rodents has shown that injecting spindle-like trains of IPSCs in TC neurons with increasing amplitude and duration increases LTS initiation probability and decreases time to LTS in response to those trains (*105*), suggesting that IPSC amplitude and duration interact to control both LTS initiation probability and timing. This difference might be attributed to injections of different IPSC waveforms, as we injected only a single IPSC, while the previous study used trains of IPSCs.

Finally, we found that at rest, sharp driver-like EPSCs evoke more firing when cells are at rest, whereas slow modulator-like EPSCs evoke more firing during activity. Modulatory-like EPSCs can emerge from several sources—application of noradrenaline or acetylcholine induces slow depolarizations in TC neurons (*118*). Pharmacological activation of mGluR in nRT neurons produces a long-lasting excitatory response (*100*). Another possible source of modulator-like

EPSCs in the nRT is depolarizing GABA. Although still controversial, there is evidence to support that GABA is depolarizing in the nRT in certain conditions (*76*). The nRT shows reduced expression of the Cl^- exporter, KCC2, compared with other brain regions in adults, and its physiological ECl^- is elevated (*53*, *76*–*78*). Synaptically released GABA appears to be capable of triggering action potentials in nRT neurons (*76*). This, coupled with the exceptionally slow decay time constants for GABAergic currents in nRT neurons (τ_{fast} = 38 ms; τ_{slow} = 186 ms) (*48*), supports the existence of these modulator-like EPSCs in the nRT.

Biological variables such as species, temperature, sex, and age are important determinants of thalamic physiology. For instance, recording at physiological temperature (i.e., 32 °C), compared with room temperature, reduces synaptically driven spiking in TC neurons in response to trains of optical stimulation (*119*). Although our study did not examine the effects of temperature, species differences, or specific thalamic neuron types (e.g., first-order vs. higher-order nuclei), it provides a valuable reference for interpreting synaptic current changes in future studies. Furthermore, neurons in vivo are continuously bombarded by intense synaptic background activity (*120*). Here, we used a simple paradigm to investigate how a single incoming synthetic synaptic current influences neuronal firing, which does not account for the complex interactions that arise when multiple synaptic currents act in concert to influence spiking behavior. Future studies could expand upon our findings by examining how these factors collectively modulate neuronal activity.

A limitation of the synthetic currents used in our study is that these currents do not account for the reduction of the driving force that would happen with natural synaptic currents as the membrane potential approaches the reversal potential. This would be captured by dynamic clamp. Furthermore, we did not examine how changes in membrane conductance, which would normally be associated with the opening of ion channels, affect firing. Therefore, the effects of conductance changes that could result, for instance, in shunting inhibition were not examined.

In conclusion, we present a comparative study showing how nRT and TC neurons from the adult murine thalamus respond to synthetic EPSCs and IPSCs of different shapes. Our study provides a quantitative map to relate changes in shape parameters of synthetic synaptic currents to neuronal firing in the thalamus, with important implications for interpreting synaptic current changes in normal and pathological conditions.

3.5. Methods

Animals

All protocols were approved by the Institutional Animal Care and Use Committees at the University of California, San Francisco, and Gladstone Institutes. Precautions were taken to minimize stress and the number of animals used in each set of experiments. Adult male (*n* = 4) and female (*n* = 9) (8–16-wk-old) wild-type C57BL/6J mice (ISMR_JAX: 000664) were used for all experiments.

Ex Vivo Patch-Clamp Electrophysiology

Mice were deeply anesthetized with 4% isoflurane and perfused transcardially with ice-cold sucrose cutting solution (234 mM sucrose, 26 mM $NaHCO_3$, 11 mM glucose, 10 mM $MgSO_4$, 2.5 mM KCl, 1.25 mM NaH_2PO_4, and 0.5 mM $CaCl_2$, equilibrated with 95% O_2 and 5% CO_2). Brains were rapidly extracted and dissected in ice-cold sucrose cutting solution. For thalamic recordings, 250-μm-thick horizontal slices were prepared. Slices were incubated at 32°C for 30 min and then at 24–26°C for 1 h in artificial cerebrospinal fluid (ACSF) (126 mM NaCl, 26 mM $NaHCO_3$, 10 mM glucose, 2.5 mM KCl, 2 mM $CaCl_2$, 1.25 mM NaH_2PO_4, and 1 mM $MgSO_4$, equilibrated with 95% O_2 and 5% CO_2).

Recordings were performed as previously described (*57*, *99*, *121*, *122*). Briefly, slices were transferred to a chamber perfused at a rate of 1.5–2.0 mL/min with ACSF at 24–26°C. nRT and TC neurons were visually identified by differential contrast optics with an Olympus microscope (×60 objective; numerical aperture, 1.1; working distance 1.5 mm; SKU 1-U2M592). nRT neurons

were randomly sampled across the entirety of nRT; TC neurons were sampled across the ventrobasal and ventrolateral nucleus of the thalamus. Electrophysiological data were acquired at 100 kHz and filtered at 3 kHz using a Multiclamp 700B amplifier (Molecular Devices) and the pClamp11 software suite (Molecular Devices). Current clamp recordings were made using glass pipettes with resistance 5–8 MΩ, filled with an internal solution (120 mM potassium gluconate, 11 mM KCl, 11 mM EGTA, 10 mM HEPES,1 mM $MgCl_2$, and 1 mM $CaCl_2$, pH adjusted to 7.4 with KOH, 290 mosmol/kgH_2O). E_{Cl} was calculated to be −55.6 mV based on the Nernst equation. Liquid junction potentials were calculated to be −12.5 mV and corrected offline. Recordings were done in the presence of DNQX (30 μM, Sigma-Aldrich, no. D0540), dl-2-Amino-5-phosphonopentanoic acid (APV) (100 μM, Sigma-Aldrich, no. A5282), and picrotoxin (100 μM, Sigma-Aldrich, no. P1675).

Statistical Analyses

General graphing and statistical analyses were performed using Python and Prism (GraphPad). Sample size is defined by the number of observations (i.e., cells). No statistical method was used to predetermine sample size. Data are presented as mean ± standard error of means. Normal distributions of data were not assumed. Animal subjects and cell recordings were randomized within experimental blocks to yield approximately equal sampling of experimental conditions. Repeated measurements were analyzed using two-way repeated-measures ANOVA in Prism. Statistical significance values and sample sizes are described in the figure legends.

3.6. Figures

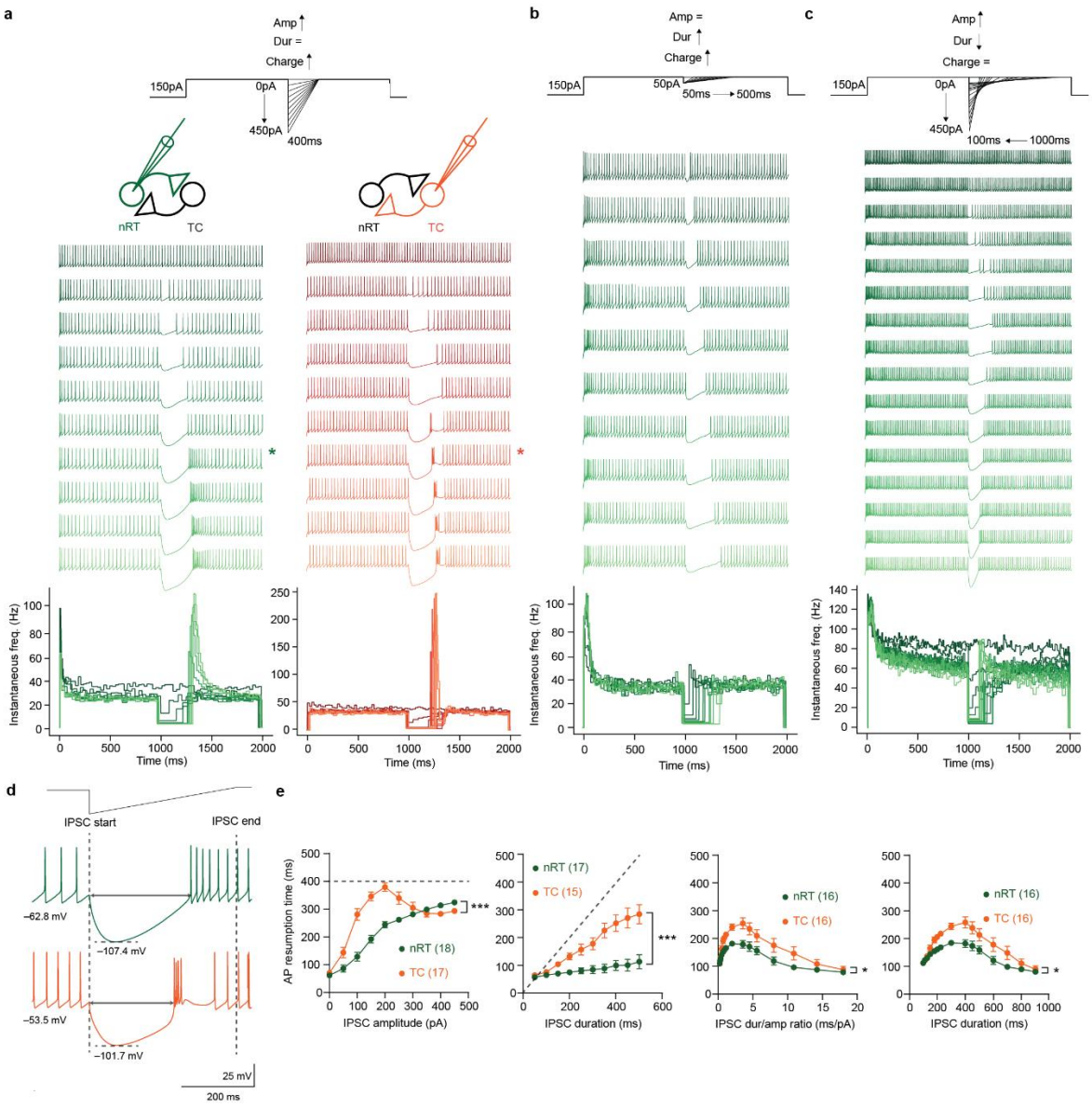

Figure 3.1. Firing inhibition by synthetic IPSCs during ongoing activity.

(A) Top, Current injection protocol and recording configuration. Middle, Representative traces of nRT (green) and TC (orange) neurons in response to synthetic IPSCs of increasing amplitude and charge, with the duration held constant at 400 ms. *Traces selected for D. Bottom, instantaneous firing rate plots. **(B)** Top, Current injection protocol. Middle, Representative traces of nRT neurons in response to synthetic IPSCs of increasing duration and charge, with the amplitude held constant at 50 pA. Bottom, Instantaneous firing rate plots. **(C)** Top, Current injection protocol. Middle, Representative traces of nRT neurons in response to synthetic IPSCs of increasing amplitude and decreasing duration, with the charge held constant at 22,500 fC. Bottom, Instantaneous firing rate plots. **(D)** Zoomed-in traces showing responses to synthetic
(Figure caption continued on the next page.)

(Figure caption continued from the previous page.)
IPSCs. Dashed lines indicate the start and end of synthetic IPSCs. Arrows indicate the time to LTS. **(E)** Summary data for results shown in B (left), C (middle), and D (right). Dashed lines indicate the duration of synthetic IPSCs used in the protocols. Two-way RM ANOVA comparing the mean action potential resumption time between nRT (green) and TC (orange) neurons while varying different IPSC shape parameters. IPSC amplitude (left) (nRT: n = 18 cells, TC: n = 17 cells, $P = 1.30 \times 10^{-4}$); IPSC duration (middle) (nRT: n = 17 cells, TC: n = 15 cells, $P = 1.58 \times 10^{-4}$); IPSC duration/amplitude ratio (right) (nRT: n = 16 cells, TC: n = 16 cells, $P = 1.48 \times 10^{-2}$). IPSCs, inhibitory postsynaptic currents; LTS, low-threshold spike; nRT, nucleus reticularis thalami; TC, thalamocortical nuclei. Statistical thresholds used were as follows: *$P < 0.05$; ***$P < 0.001$.

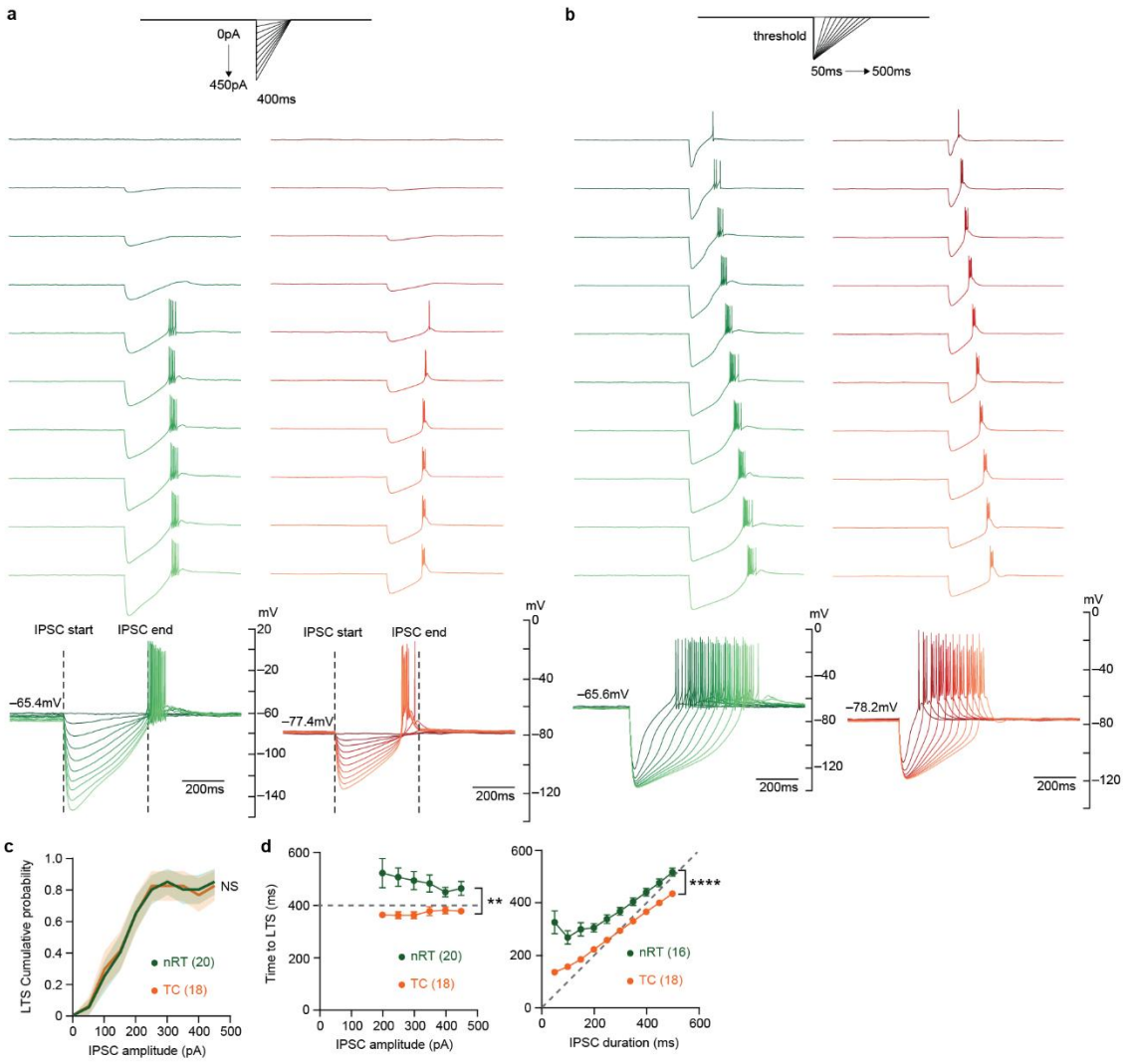

Figure 3.2. LTS evoked by synthetic IPSCs from rest.

(A) Top, Current injection protocol. Middle, Representative traces of nRT (green) and TC (orange) neurons in response to synthetic IPSCs of increasing amplitude and charge, with the duration held constant at 400 ms. Bottom, Traces overlaid. Dashed lines indicate the start and end of synthetic IPSCs. **(B)**, Top, Current injection protocol. Middle, Representative traces of nRT (green) and TC (orange) neurons in response to synthetic IPSCs of increasing duration and charge, with the amplitude set at the threshold current, which is defined as the current that evokes LTS at all steps. Bottom, Traces overlaid. **(C)** Cumulative probability of evoking LTS with increasing synthetic IPSC amplitude. Two-way RM ANOVA comparing the two cumulative probability curves between nRT (green) and TC (orange) neurons (nRT: n = 20 cells, TC: n = 18 cells, $P = 6.57 \times 10^{-1}$). **(D)** Summary data for results shown in A and B. Dashed lines indicate the duration of synthetic IPSCs used in the protocols. Two-way RM ANOVA comparing the mean time to LTS from the start of synthetic IPSC between nRT (green) and TC (orange) neurons while varying different IPSC shape parameters. IPSC amplitude (left) (nRT: n = 20 cells, TC: n = 18 cells, $P = 4.42 \times 10^{-3}$); IPSC duration (right) (nRT: n = 16 cells, TC: n = 18 cells, $P = 6.23 \times 10^{-6}$). IPSCs, inhibitory postsynaptic currents; LTS, low-threshold spike; nRT, nucleus reticularis thalami; NS,
(Figure caption continued on the next page.)

(Figure caption continued from the previous page.)
not significant; TC, thalamocortical nuclei. Statistical thresholds used were as follows: $^{**}P < 0.01$; $^{****}P < 0.0001$.

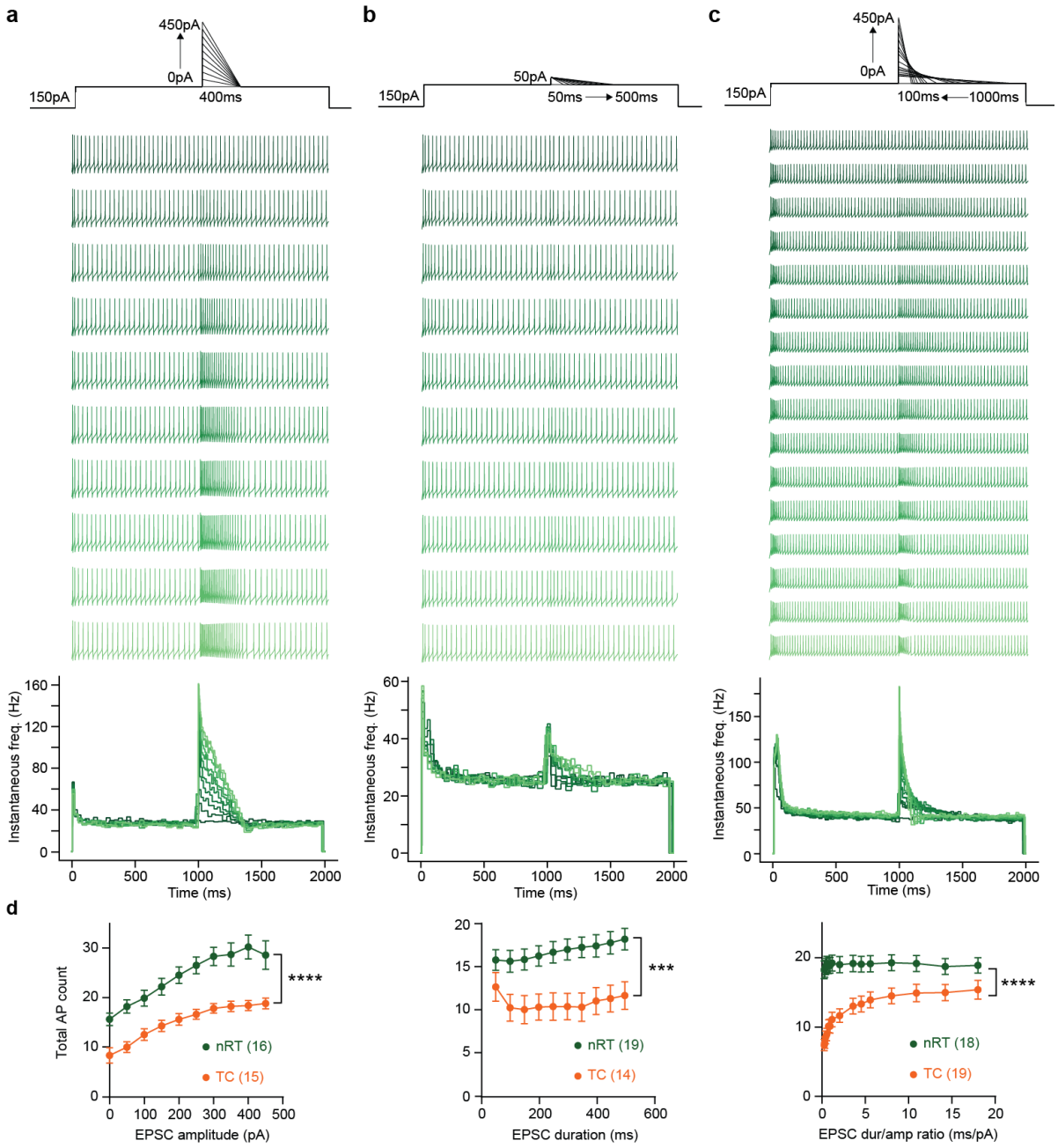

Figure 3.3. Firing evoked by synthetic EPSCs during ongoing activity.

(A) Top, Current injection protocol. Middle, Representative traces of nRT neurons in response to synthetic EPSCs of increasing amplitude and charge, with the duration held constant at 400 ms. Bottom, Instantaneous firing rate plots. **(B)** Top, Current injection protocol. Middle, Representative traces of nRT neurons in response to synthetic EPSCs of increasing duration and charge, with the amplitude held constant at 50 pA. Bottom, Instantaneous firing rate plots. **(C)** Top, Current injection protocol. Middle, Representative traces of nRT neurons in response to synthetic EPSCs of increasing amplitude and decreasing duration, with the charge held constant at 22,500 fC. Bottom, Instantaneous firing rate plots. **(D)** Summary data for results shown in A (left), B(middle), (Figure caption continued on the next page.)

(Figure caption continued from the previous page.)
and C (right). Two-way RM ANOVA comparing the mean number of action potentials evoked between nRT (green) and TC (orange) neurons while varying different EPSC shape parameters. The total count of action potentials evoked from the start of the synthetic EPSC to 500 ms after is shown. The start of a synthetic EPSC is 1 s after the start of the depolarizing current injection. EPSC amplitude (left) (nRT: $n = 16$ cells, TC: $n = 15$ cells, $P = 2.75 \times 10^{-5}$); EPSC duration (middle) (nRT: $n = 19$ cells, TC: $n = 14$ cells, $P = 4.34 \times 10^{-3}$); EPSC duration/amplitude ratio (right) (nRT: $n = 18$ cells, TC: $n = 19$ cells, $P = 2.62 \times 10^{-5}$). EPSCs, excitatory postsynaptic currents; LTS, low-threshold spike; nRT, nucleus reticularis thalami; TC, thalamocortical nuclei. Statistical thresholds used were as follows: ***$P < 0.001$; ****$P < 0.0001$.

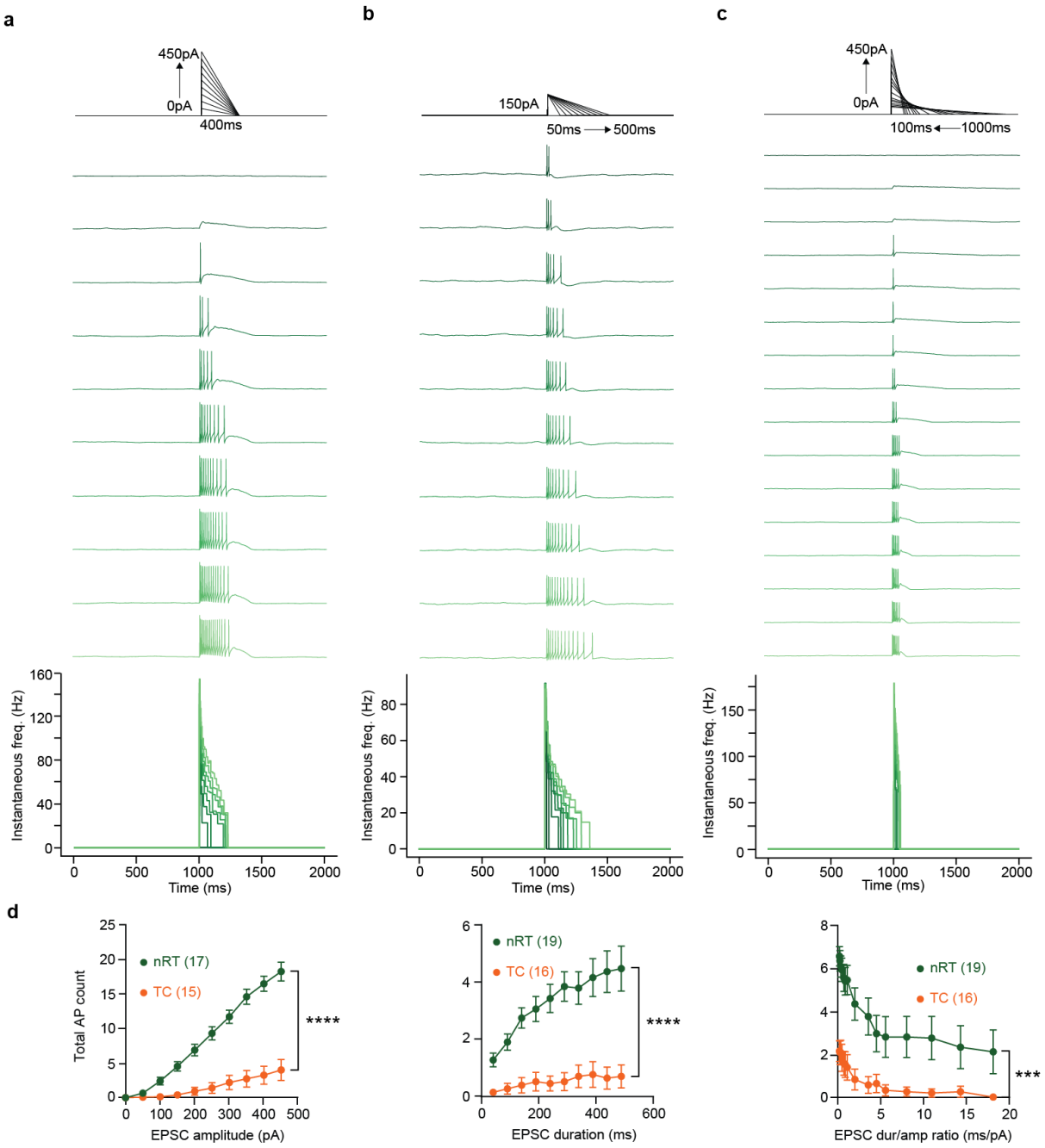

Figure 3.4. Firing evoked by synthetic EPSCs from rest.

(A) Top, Current injection protocol. Middle, Representative traces of nRT neurons in response to synthetic EPSCs of increasing amplitude and charge, with the duration held constant at 400 ms. Bottom, Instantaneous firing rate plots. **(B)** Top, Current injection protocol. Middle, Representative traces of nRT neurons in response to synthetic EPSCs of increasing duration and charge, with the amplitude held constant at 150 pA. Bottom, Instantaneous firing rate plots. **(C)** Top, Current injection protocol. Middle, Representative traces of nRT neurons in response to synthetic EPSCs of increasing amplitude and decreasing duration, with the charge held constant at 22,500 fC. Bottom, Instantaneous firing rate plots. **(D)** Summary data for results shown in A (left), B (middle), (Figure caption continued on the next page.)

(Figure caption continued from the previous page.)
and C (right). Two-way RM ANOVA comparing the mean number of action potentials evoked between nRT (green) and TC (orange) neurons while varying different EPSC shape parameters. EPSC amplitude (left) (nRT: $n = 17$ cells, TC: $n = 15$ cells, $P = 7.95 \times 10^{-8}$); EPSC duration (middle) (nRT: $n = 19$ cells, TC: $n = 16$ cells, $P = 4.39 \times 10^{-5}$); EPSC duration/amplitude ratio (right) (nRT: $n = 19$ cells, TC: $n = 16$ cells, $P = 2.75 \times 10^{-4}$). EPSCs, excitatory postsynaptic currents; LTS, low-threshold spike; nRT, nucleus reticularis thalami; TC, thalamocortical nuclei. Statistical thresholds used were as follows: ***$P < 0.001$; ****$P < 0.0001$.

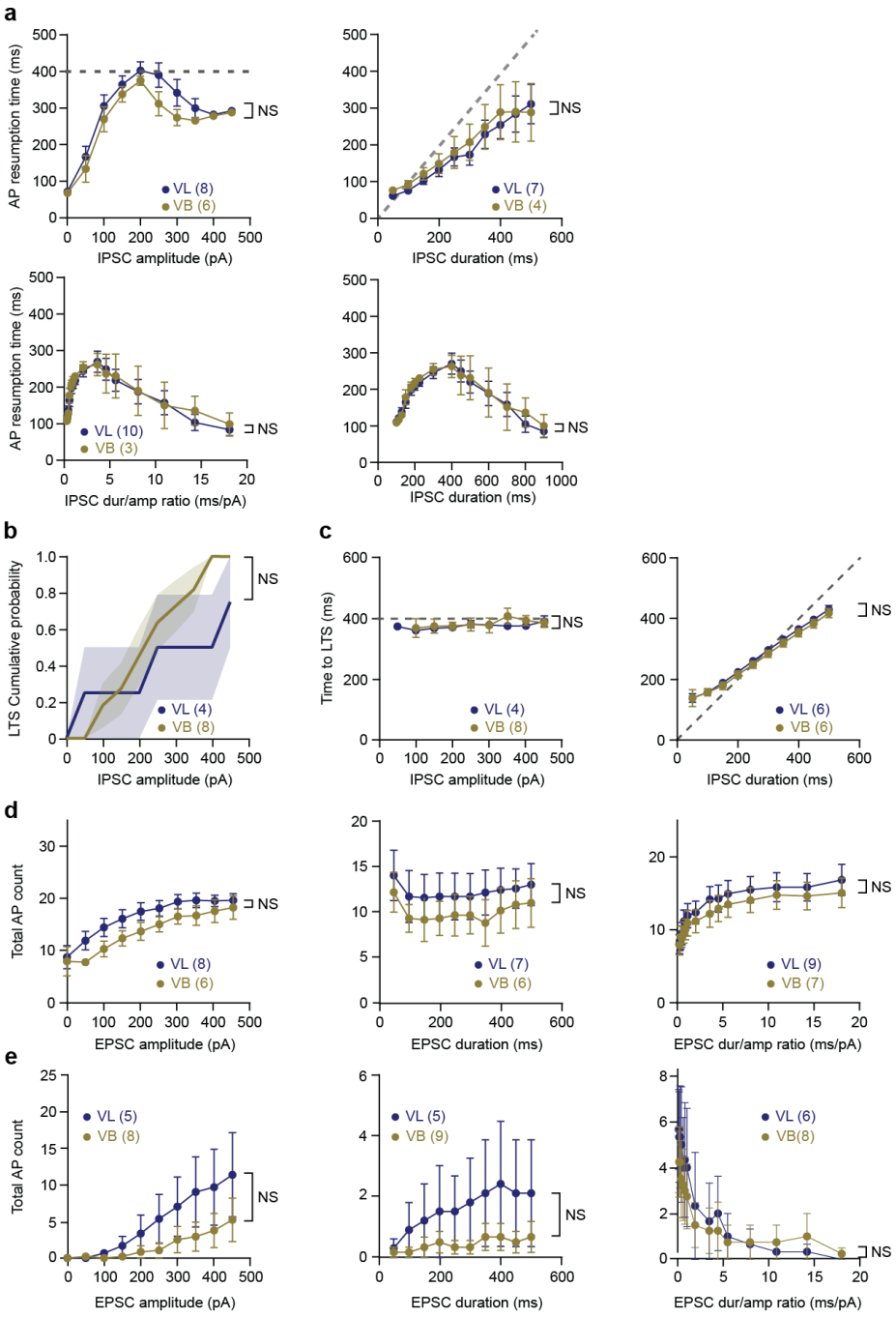

Figure 3.5. No difference in firing response to synthetic currents between VB and VL neurons.

(A) Summary data for results shown in Fig. 4.1D with TC data split into VB and VL groups. Dashed lines indicate the duration of synthetic IPSCs used in the protocols. Two-way RM ANOVA comparing the mean action potential resumption time between VB (copper) and VL (blue) neurons while varying different IPSC shape parameters. IPSC amplitude (top left) (VB: n = 6 cells, VL: n = 8 cells, P = 0.17); IPSC duration (top right) (VB: n = 4 cells, VL: n = 7 cells, P = 0.75); IPSC
(Figure caption continued on the next page.)

(Figure caption continued from the previous page.)
duration/amplitude ratio (bottom) (VB: *n* = 3 cells, VL: *n* = 10 cells, *P* = 0.89). **(B)**: Summary data for results shown in Fig. 4.2C with TC data split into VB and VL groups. Two-way RM ANOVA comparing the two cumulative probability curves between VB (copper) and VL (blue) neurons (VB: *n* = 8 cells, VL: *n* = 4 cells, *P* = 0.41). **(C)** Summary data for results shown in Fig. 4.2D with TC data split into VB and VL groups. Dashed lines indicate the duration of synthetic IPSCs used in the protocols. Two-way RM ANOVA comparing the mean time to LTS from the start of synthetic IPSC between VB (copper) and VL (blue) neurons while varying different IPSC shape parameters. IPSC amplitude (left) (VB: *n* = 8 cells, VL: *n* = 4 cells, *P* = 0.97); IPSC duration (right) (VB: *n* = 6 cells, VL: *n* = 6 cells, *P* = 0.53). **(D)** Summary data for results shown in Fig. 4.3D with TC data split into VB and VL groups. Two-way RM ANOVA comparing the mean number of action potentials evoked between VB (copper) and VL (blue) neurons while varying different EPSC shape parameters. EPSC amplitude (left) (VB: *n* = 6 cells, VL: *n* = 8 cells, *P* = 0.15); EPSC duration (middle) (VB: *n* = 6 cells, VL: *n* = 7 cells, *P* = 0.51); EPSC duration/amplitude ratio (right) (VB: *n* = 7 cells, VL: *n* = 9 cells, *P* = 0.65). **(E)** Summary data for results shown in Fig. 2.4D with TC data split into VB and VL groups. Two-way RM ANOVA comparing the mean number of action potentials evoked between VB (copper) and VL (blue) neurons while varying different EPSC shape parameters. EPSC amplitude (left) (VB: *n* = 8 cells, VL: *n* = 5 cells, *P* =0.23); EPSC duration (middle) (VB: *n* = 9 cells, VL: *n* = 5 cells, *P* = 0.30); EPSC duration/amplitude ratio (right) (VB: *n* = 8 cells, VL: *n* = 6 cells, *P* = 0.74). EPSCs, excitatory postsynaptic currents; IPSCs, inhibitory postsynaptic currents; LTS, low-threshold spike; nRT, nucleus reticularis thalami; NS, not significant; TC, thalamocortical nuclei; VB, ventrobasal nucleus; VL, ventrolateral nucleus.

3.7. Tables

Table 3.1. Intrinsic properties of nRT and TC neurons

Sample size N (cells) is included in brackets.
* Measured in response to a 100 ms +5 mV test pulse.
# Atypically high membrane resistance due to the presence of synaptic blockers (i.e., DNQX, APV, picrotoxin) in the bath
† Action potentials were evoked with a 2 s 150 pA injection. Action potential measurements were taken 1 s after the start of injection. Action potential threshold was defined as the Vm when dV/dt measurements first exceeded 15 V/s.
§The bolded p-values are significant when considering the Bonferroni-corrected thresholds for multiple comparisons, which is $0.05/9 = 5.56\times10^{-3}$.

	Membrane potential Vm (mV)	Input resistance Rm (MΩ)*#	Membrane capacitance Cm (pF)*	Tau (ms)*	Action potential threshold (mV)†	Action potential amplitude (mV)†	Action potential width (ms)†	Action potential half-width (ms)†	Tonic Firing rate (Hz)†
nRT	−66.07 ± 0.93 (51)	912.03 ± 155.69 (50)	54.70 ± 2.37 (52)	1.12 ± 0.05 (52)	−48.06 ± 0.48 (42)	42.80 ± 1.00 (42)	1.57 ± 0.06 (42)	0.76 ± 0.03 (42)	35.81 ± 2.11 (42)
TC	−69.08 ± 0.69 (54)	362.54 ± 41.20 (51)	99.94 ± 3.95 (51)	2.07 ± 0.09 (51)	−47.87 ± 0.71 (47)	55.32 ± 1.26 (47)	3.04 ± 0.09 (47)	1.51 ± 0.09 (47)	22.89 ± 1.54 (47)
p-value§ (Mann-Whitney test)	**1.75×10^{-3}**	**$<1.00\times10^{-3}$**	**$<1.00\times10^{-3}$**	**$<1.00\times10^{-3}$**	0.75	**$<1.00\times10^{-3}$**	**$<1.00\times10^{-3}$**	**$<1.00\times10^{-3}$**	**$<1.00\times10^{-3}$**
VB	−69.71 ± 0.97 (18)	382.35 ± 83.85 (17)	100.73 ± 6.16 (17)	2.09 ± 0.19 (17)	−47.07 ± 1.27 (17)	54.73 ± 2.10 (17)	2.71 ± 0.11 (17)	1.31 ± 0.05 (17)	20.88 ± 2.66 (17)
VL	−69.50 ± 1.12 (25)	360.85 ± 59.76 (23)	102.17 ± 5.44 (23)	2.15 ± 0.10 (23)	−48.51 ± 0.97 (24)	55.58 ± 1.76 (24)	3.34 ± 0.10 (24)	1.69 ± 0.07 (24)	23.75 ± 2.30 (24)
p-value§ (Mann-Whitney test)	0.94	0.43	0.63	0.52	0.47	0.63	**4.67×10^{-4}**	**$<1.00\times10^{-3}$**	0.55

Table 3.2. Spearman correlation coefficients of time to LTS and intrinsic properties of thalamic neurons

Sample size N (cells) is included in brackets.
* Measured in response to a 100 ms +5 mV test pulse.
† Action potentials were evoked with a 2 s 150 pA injection. Action potential measurements were taken 1 s after the start of injection. Action potential threshold was defined as the Vm when dV/dt measurements first exceeded 15 V/s.
§The bolded p-values are significant when considering the Bonferroni-corrected thresholds for multiple comparisons, which is $0.05/9 = 5.56\times10^{-3}$.

	Membrane potential Vm (mV)	Membrane resistance Rm (MΩ)*	Membrane capacitance Cm (pF)*	Tau (ms)*	Action potential threshold (mV)†	Action potential amplitude (mV)†	Action potential width (ms)†	Action potential half-width (ms)†	Tonic Firing rate (Hz)†
nRT	-8.96×10^{-2} (17)	0.17 (17)	0.35 (17)	0.50 (17)	0.82 (7)	0.54 (7)	0.25 (7)	−0.32 (7)	0.32 (7)
p-value§	0.73	0.54	0.17	4.30×10^{-2}	3.41×10^{-2}	0.24	0.60	0.48	0.48
TC	−0.18 (17)	5.39×10^{-2} (17)	0.27 (17)	0.28 (17)	0.31 (12)	0.36 (12)	0.14 (12)	0.27 (12)	−0.38 (12)
p-value§	0.48	0.84	0.30	0.28	0.33	0.25	0.67	0.40	0.25

Chapter 4: Discussion

4.1. Summary

The studies presented in this dissertation aimed to investigate how GABAergic signaling from the GPe is organized and integrated within the nRT, a structure that occupies a central position in thalamocortical circuits. In **Chapter 2**, we provided the first comprehensive functional characterization of an extrinsic GABAergic input from the GPe to the nRT. We revealed a novel form of GABAergic signaling in which GABA can exert either excitation or inhibition based on regional differences in chloride homeostasis. We provided evidence that this pathway is modulated during movement, indicating the GPe→nRT projection may be a new route through which the basal ganglia can influence thalamic activity and motor behavior. In **Chapter 3**, we investigated how nRT and TC neurons transform synaptic inputs into spiking outputs using synthetic current injections. We found that identical synthetic currents elicited distinct firing responses in nRT and TC neurons, highlighting the importance of intrinsic cellular properties in shaping activity output.

Collectively, these studies reveal multiple levels of transformation of GABAergic transmissions in thalamic networks. The ultimate effect of GABA depends not only on the source of the input, but also on chloride homeostasis and intrinsic cellular properties. Together, these mechanisms provide a framework for understanding how GABAergic signaling contributes to the flexible control of thalamic activity and behavior.

4.2. Short-term chloride dynamics as a substrate for state-dependent movement modulation

In **Chapter 2,** we raised the possibility that short-term chloride plasticity could underlie the state-dependent movement modulation of the GPe→nRT pathway. During periods of sustained GABAe release from the GPe, chloride influx through $GABA_A$ receptors could transiently

overwhelm chloride extrusion mechanisms, resulting in intracellular chloride accumulation and a depolarizing shift in E_{GABA}. Under such conditions, GPe input may become excitatory, thereby altering the effect of this pathway on downstream thalamic circuits. Conversely, during periods of lower activity, chloride extrusion through KCC2 could restore a more hyperpolarizing chloride gradient, shifting the effects of GABA back toward inhibition.

A critical question surrounding this state-dependent mechanism is that it remains unclear whether chloride dynamics occur rapidly enough to influence neural activity on the timescale of ongoing behavior. Intracellular chloride has been documented to vary across developmental stages (*123*), brain states (*124–127*), and conditions (*128*), but these processes typically occur over timescales of hours to days. Whether substantial fluctuations in intracellular chloride can occur within milliseconds to seconds remains less clear.

Experimental and computational studies indicate that chloride extrusion is substantially slower than chloride influx through $GABA_A$ receptor channels, making transient shifts in E_{Cl} theoretically possible (*129–131*). High-frequency activation of GABAergic synapses has been shown to produce transient chloride accumulation (*132*, *133*), particularly within small neuronal compartments such as dendrites (*134*), where diffusion is restricted, and the surface-area-to-volume ratio is high.

More recently, chloride-loading experiments in nRT neurons demonstrated that somatic chloride accumulation can occur and that restoration of hyperpolarized $E_{Çl}$ by extrusion mechanisms can take place within seconds (*53*). However, these experiments relied on brief puffs of muscimol to the soma and do not recapitulate physiological activation of GABAergic synapses. Whether comparable chloride dynamics can occur under activation of GPe→nRT synapses remains unknown. In particular, it is unclear whether repetitive activation of GPe inputs can induce sufficient chloride accumulation to shift GABAergic responses from inhibition to excitation.

If chloride dynamics can occur on behaviorally relevant timescales, the more speculative question is whether they contribute to the state-dependent behavioral effects of the GPe→nRT

pathway. At present, direct evidence linking intracellular chloride concentration to movement state is largely absent. Indeed, we are unaware of studies demonstrating rapid movement-associated fluctuations in intracellular chloride concentration in any brain region. Consequently, the proposed framework that chloride dynamics underlie the behavioral effects observed in **Chapter 2** remains highly speculative. To test this possibility, future studies will require direct measurements of intracellular chloride during behavior and selective manipulation of chloride homeostasis within nRT neurons.

Despite these uncertainties, the potential implications are substantial. If intracellular chloride can fluctuate dynamically during ongoing behavior and directly influence motor output, this would reshape our understanding of chloride homeostasis from a largely cellular and synaptic property to a dynamic mechanism for circuit and behavioral computation.

4.3. Functional organization of the GPe→nRT pathway *in vivo*

Much of the circuit logic of the GPe→nRT pathway presented in **Chapter 2** was derived from circuit studies performed in *ex vivo* slices. *Ex vivo* slices cannot fully capture the complexity of neuronal activity in the intact brain. Further experiments will need to be performed to validate whether the circuit effects of GPe stimulation hold during natural behavior.

Another unresolved question concerns the organizational principles of the GPe→nRT projection itself. Our preliminary data suggest that the GPe→nRT pathway is organized topographically, with anterior GPe targeting the anterior nRT and posterior GPe targeting the posterior nRT. If both GPe populations are synchronously active during behavior, GPe could simultaneously suppress activity in anterior nRT while promoting activity in posterior nRT. Such a mechanism would generate opposing effects across distinct nRT subnetworks and downstream thalamocortical nuclei. The experiments presented in **Chapter 2** focused on the anterior nRT, and therefore do not address how simultaneous engagement of anterior and posterior GPe→nRT pathways influences circuit function or behavior. Future studies combining large-scale recordings

with pathway-specific manipulations will be necessary to determine how the GPe→anterior nRT and GPe→posterior nRT streams are coordinated *in vivo* and how their interactions shape thalamic information processing and motor control. Understanding the spatiotemporal organization of activity across the GPe→nRT pathway will ultimately reveal circuit functions that cannot be predicted from studying individual pathway components in isolation.

4.4. Relevance to movement disorders

The GPe→nRT pathway characterized in **Chapter 2** occupies a unique circuit node at the interface between the basal ganglia and thalamus, two networks that are heavily implicated in a wide range of neurological and neuropsychiatric disorders. In particular, alterations in this pathway may contribute to movement disorders such as Parkinson's disease. Classical models of Parkinson's disease pathophysiology focus on abnormal activity involving the canonical basal ganglia output nuclei, the GPi and SNr. The discovery of this previously unappreciated pathway opens new lines of investigation as to whether it could be altered in disease conditions and contribute to motor and non-motor symptoms in Parkinson's Disease. The GPe has emerged as a potential target for deep brain stimulation, with studies showing long-lasting therapeutic effects that persist beyond the stimulation period (*135*). The GPe→nRT pathway may contribute to some of the therapeutic effects or may itself be leveraged as a future target for intervention.

At present, the clinical relevance of the GPe→nRT pathway remains speculative. The studies presented here represent only the first step towards the functional and pathological significance of this circuit.

References

1. M. DeLong, T. Wichmann, Update on models of basal ganglia function and dysfunction. *Parkinsonism Relat Disord* **15**, S237–S240 (2009).

2. A. B. Nelson, A. C. Kreitzer, Reassessing models of basal ganglia function and dysfunction. *Annu Rev Neurosci* **37**, 117–135 (2014).

3. R. L. Albin, A. B. Young, J. B. Penney, The functional anatomy of basal ganglia disorders. *Trends Neurosci* **12**, 366–375 (1989).

4. M. R. DeLong, Primate models of movement disorders of basal ganglia origin. *Trends Neurosci* **13**, 281–285 (1990).

5. J. A. Obeso, M. Jahanshahi, L. Alvarez, R. Macias, I. Pedroso, L. Wilkinson, N. Pavon, B. Day, S. Pinto, M. C. Rodríguez-Oroz, J. Tejeiro, J. Artieda, P. Talelli, O. Swayne, R. Rodríguez, K. Bhatia, M. Rodriguez-Diaz, G. Lopez, J. Guridi, J. C. Rothwell, What can man do without basal ganglia motor output? The effect of combined unilateral subthalamotomy and pallidotomy in a patient with Parkinson's disease. *Exp Neurol* **220**, 283–292 (2009).

6. M. Inase, J. A. Buford, M. E. Anderson, Changes in the control of arm position, movement, and thalamic discharge during local inactivation in the globus pallidus of the monkey. *J Neurophysiol* **75**, 1087–1104 (1996).

7. M. Desmurget, R. S. Turner, Testing basal ganglia motor functions through reversible inactivations in the posterior internal globus pallidus. *J Neurophysiol* **99**, 1057–1076 (2008).

8. C. D. Courtney, A. Pamukcu, C. S. Chan, Cell and circuit complexity of the external globus pallidus. *Nat Neurosci* **26**, 1147–1159 (2023).

9. G. E. Alexander, M. D. Crutcher, Functional architecture of basal ganglia circuits: neural substrates of parallel processing. *Trends Neurosci* **13**, 266–271 (1990).

10. J. W. Crabtree, Functional Diversity of Thalamic Reticular Subnetworks. *Front Syst Neurosci* **12**, 41 (2018).

11. N. Hádinger, E. Bősz, B. Tóth, G. Vantomme, A. Lüthi, L. Acsády, Region-selective control of the thalamic reticular nucleus via cortical layer 5 pyramidal cells. *Nat Neurosci* **26**, 116–130 (2023).

12. M. M. McGregor, A. B. Nelson, Circuit Mechanisms of Parkinson's Disease. *Neuron* **101**, 1042–1056 (2019).

13. D. J. Hegeman, E. S. Hong, V. M. Hernandez, C. S. Chan, The external globus pallidus: progress and perspectives. *Eur J Neurosci* **43**, 1239–65 (2016).

14. Z. A. Abecassis, B. L. Berceau, P. H. Win, D. Garcia, H. S. Xenias, Q. Cui, A. Pamukcu, S. Cherian, V. M. Hernandez, U. Chon, B. K. Lim, Y. Kim, N. J. Justice, R. Awatramani, B. M. Hooks, C. R. Gerfen, S. M. Boca, C. S. Chan, Npas1(+)-Nkx2.1(+) Neurons Are an Integral Part of the Cortico-pallido-cortical Loop. *J Neurosci* **40**, 743–768 (2020).

15. A. Saunders, I. A. Oldenburg, V. K. Berezovskii, C. A. Johnson, N. D. Kingery, H. L. Elliott, T. Xie, C. R. Gerfen, B. L. Sabatini, A direct GABAergic output from the basal ganglia to frontal cortex. *Nature* **521**, 85–9 (2015).

16. V. M. Hernandez, D. J. Hegeman, Q. Cui, D. A. Kelver, M. P. Fiske, K. E. Glajch, J. E. Pitt, T. Y. Huang, N. J. Justice, C. S. Chan, Parvalbumin+ Neurons and Npas1+ Neurons Are Distinct Neuron Classes in the Mouse External Globus Pallidus. *J Neurosci* **35**, 11830–47 (2015).

17. A. Abdi, N. Mallet, F. Y. Mohamed, A. Sharott, P. D. Dodson, K. C. Nakamura, S. Suri, S. V. Avery, J. T. Larvin, F. N. Garas, S. N. Garas, F. Vinciati, S. Morin, E. Bezard, J. Baufreton, P. J. Magill, Prototypic and arkypallidal neurons in the dopamine-intact external globus pallidus. *J Neurosci* **35**, 6667–6688 (2015).

18. K. E. Glajch, D. A. Kelver, D. J. Hegeman, Q. Cui, H. S. Xenias, E. C. Augustine, V. M. Hernandez, N. Verma, T. Y. Huang, M. Luo, N. J. Justice, C. S. Chan, Npas1+ Pallidal Neurons Target Striatal Projection Neurons. *J Neurosci* **36**, 5472–88 (2016).

19. Q. Cui, A. Pamukcu, S. Cherian, I. Y. M. Chang, B. L. Berceau, H. S. Xenias, M. H. Higgs, S. Rajamanickam, Y. Chen, X. Du, Y. Zhang, H. McMorrow, Z. A. Abecassis, S. M. Boca, N. J. Justice, C. J. Wilson, C. S. Chan, Dissociable Roles of Pallidal Neuron Subtypes in Regulating Motor Patterns. *J Neurosci* **41**, 4036–4059 (2021).

20. N. Mallet, B. R. Micklem, P. Henny, M. T. Brown, C. Williams, J. P. Bolam, K. C. Nakamura, P. J. Magill, Dichotomous organization of the external globus pallidus. *Neuron* **74**, 1075–86 (2012).

21. D. Pinault, The thalamic reticular nucleus: structure, function and concept. *Brain Res Brain Res Rev* **46**, 1–31 (2004).

22. M. Nakajima, L. I. Schmitt, M. M. Halassa, Prefrontal Cortex Regulates Sensory Filtering through a Basal Ganglia-to-Thalamus Pathway. *Neuron* **103**, 445-458.e10 (2019).

23. M. M. Halassa, Z. Chen, R. D. Wimmer, P. M. Brunetti, S. Zhao, B. Zikopoulos, F. Wang, E. N. Brown, M. A. Wilson, State-dependent architecture of thalamic reticular subnetworks. *Cell* **158**, 808–821 (2014).

24. R. D. Wimmer, L. I. Schmitt, T. J. Davidson, M. Nakajima, K. Deisseroth, M. M. Halassa, Thalamic control of sensory selection in divided attention. *Nature* **526**, 705–709 (2015).

25. F. Crick, Function of the thalamic reticular complex: the searchlight hypothesis. *Proc Natl Acad Sci U S A* **81**, 4586–90 (1984).

26. C. M. Severin, P. A. Young, L. C. Massapust, Pallidothalamic projections in the rat. *J Comp Neurol* **166**, 491–502 (1976).

27. D. A. Carter, H. C. Fibiger, The projections of the entopeduncular nucleus and globus pallidus in rat as demonstrated by autoradiography and horseradish peroxidase histochemistry. *J Comp Neurol* **177**, 113–123 (1978).

28. H. J. W. Nauta, Projections of the pallidal complex: An autoradiographic study in the cat. *Neuroscience* **4**, 1853–1873 (1979).

29. S. N. Haber, H. J. Groenewegen, E. A. Grove, W. J. Nauta, Efferent connections of the ventral pallidum: evidence of a dual striato pallidofugal pathway. *J Comp Neurol* **235**, 322–335 (1985).

30. C. Asanuma, Axonal arborizations of a magnocellular basal nucleus input and their relation to the neurons in the thalamic reticular nucleus of rats. *Proc Natl Acad Sci U S A* **86**, 4746–4750 (1989).

31. C. Asanuma, L. L. Porter, Light and electron microscopic evidence for a GABAergic projection from the caudal basal forebrain to the thalamic reticular nucleus in rats. *J Comp Neurol* **302**, 159–172 (1990).

32. J. Cornwall, J. D. Cooper, O. T. Phillipson, Projections to the rostral reticular thalamic nucleus in the rat. *Exp Brain Res* **80**, 157–71 (1990).

33. L. N. Hazrati, A. Parent, Projection from the external pallidum to the reticular thalamic nucleus in the squirrel monkey. *Brain Res* **550**, 142–146 (1991).

34. J. A. Gandia, S. De Las Heras, M. García, J. M. Giménez-Amaya, Afferent projections to the reticular thalamic nucleus from the globus pallidus and the substantia nigra in the rat. *Brain Res Bull* **32**, 351–358 (1993).

35. M. E. Bickford, A. E. Günlük, S. C. Van Horn, S. M. Sherman, GABAergic projection from the basal forebrain to the visual sector of the thalamic reticular nucleus in the cat. *J Comp Neurol* **348**, 481–510 (1994).

36. C. Asanuma, GABAergic and pallidal terminals in the thalamic reticular nucleus of squirrel monkeys. *Exp Brain Res* **101**, 439–451 (1994).

37. T. Kayahara, K. Nakano, The globus pallidus sends axons to the thalamic reticular nucleus neurons projecting to the centromedian nucleus of the thalamus: a light and electron microscope study in the cat. *Brain Res Bull* **45**, 623–630 (1998).

38. T. Yamamoto, R. Hassler, C. Huber, A. Wagner, K. Sasaki, Electrophysiologic studies on the pallido- and cerebellothalamic projections in squirrel monkeys (Saimiri sciureus). *Exp Brain Res* **51**, 77–87 (1983).

39. J. H. Pazo, A. C. Barceló, E. Bellantonio, V. C. Pazo, N. Almarares, Electrophysiologic study of globus pallidus projections to the thalamic reticular nucleus. *Brain Res Bull* **94**, 82–89 (2013).

40. N. Villalobos, A. Oviedo-Chavez, A. Alatorre, A. Rios, R. Barrientos, A. Delgado, E. Querejeta, Striatum and globus pallidus control the electrical activity of reticular thalamic nuclei. *Brain Res* **1644**, 258–66 (2016).

41. N. Villalobos, S. Almazán-Alvarado, V. M. Magdaleno-Madrigal, Elevation of GABA levels in the globus pallidus disinhibits the thalamic reticular nucleus and desynchronized cortical beta oscillations. *J Physiol Sci* **72**, 17 (2022).

42. N. Villalobos, V. M. Magdaleno-Madrigal, Pallidal GABA B receptors: involvement in cortex beta dynamics and thalamic reticular nucleus activity. *J Physiol Sci* **73**, 14 (2023).

43. A. Parent, L. N. Hazrati, Functional anatomy of the basal ganglia. I. The cortico-basal ganglia-thalamo-cortical loop. *Brain Res Brain Res Rev* **20**, 91–127 (1995).

44. N. N. Foster, J. Barry, L. Korobkova, L. Garcia, L. Gao, M. Becerra, Y. Sherafat, B. Peng, X. Li, J.-H. Choi, L. Gou, B. Zingg, S. Azam, D. Lo, N. Khanjani, B. Zhang, J. Stanis, I. Bowman, K. Cotter, C. Cao, S. Yamashita, A. Tugangui, A. Li, T. Jiang, X. Jia, Z. Feng, S. Aquino, H.-S. Mun, M. Zhu, A. Santarelli, N. L. Benavidez, M. Song, G. Dan, M. Fayzullina, S. Ustrell, T. Boesen, D. L. Johnson, H. Xu, M. S. Bienkowski, X. W. Yang, H. Gong, M. S. Levine, I. Wickersham, Q. Luo, J. D. Hahn, B. K. Lim, L. I. Zhang, C. Cepeda, H. Hintiryan, H.-W. Dong, The mouse cortico-basal ganglia-thalamic network. *Nature* **598**, 188–194 (2021).

45. P. M. Fogerson, J. R. Huguenard, Tapping the Brakes: Cellular and Synaptic Mechanisms that Regulate Thalamic Oscillations. *Neuron* **92**, 687–704 (2016).

46. B. Crompe, A. Aristieta, A. Leblois, S. Elsherbiny, T. Boraud, N. P. Mallet, The globus pallidus orchestrates abnormal network dynamics in a model of Parkinsonism. *Nat Commun* **11**, 1570 (2020).

47. C. F. Stevens, Y. Wang, Facilitation and depression at single central synapses. *Neuron* **14**, 795–802 (1995).

48. S. J. Zhang, J. R. Huguenard, D. A. Prince, GABAA receptor-mediated Cl- currents in rat thalamic reticular and relay neurons. *J Neurophysiol* **78**, 2280–2286 (1997).

49. V. Stein, R. A. Nicoll, GABA generates excitement. *Neuron* **37**, 375–378 (2003).

50. J. Szabadics, C. Varga, G. Molnár, S. Oláh, P. Barzó, G. Tamás, Excitatory effect of GABAergic axo-axonic cells in cortical microcircuits. *Science* **311**, 233–235 (2006).

51. H. J. Choi, C. J. Lee, A. Schroeder, Y. S. Kim, S. H. Jung, J. S. Kim, D. Y. Kim, E. J. Son, H. C. Han, S. K. Hong, C. S. Colwell, Y. I. Kim, Excitatory actions of GABA in the suprachiasmatic nucleus. *J Neurosci* **28**, 5450–5459 (2008).

52. P. Barthó, J. A. Payne, T. F. Freund, L. Acsády, Differential distribution of the KCl cotransporter KCC2 in thalamic relay and reticular nuclei. *Eur J Neurosci* **20**, 965–975 (2004).

53. P. M. Klein, A. C. Lu, M. E. Harper, H. M. McKown, J. D. Morgan, M. P. Beenhakker, Tenuous Inhibitory GABAergic Signaling in the Reticular Thalamus. *J Neurosci* **38**, 1232–1248 (2018).

54. A. Kyrozis, D. B. Reichling, Perforated-patch recording with gramicidin avoids artifactual changes in intracellular chloride concentration. *J Neurosci Methods* **57**, 27–35 (1995).

55. J. Huguenard, D. Prince, A novel T-type current underlies prolonged Ca(2+)-dependent burst firing in GABAergic neurons of rat thalamic reticular nucleus. *J Neurosci* **12**, 3804–3817 (1992).

56. Y. Li, V. G. Lopez-Huerta, X. Adiconis, K. Levandowski, S. Choi, S. K. Simmons, M. A. Arias-Garcia, B. Guo, A. Y. Yao, T. R. Blosser, R. D. Wimmer, T. Aida, A. Atamian, T. Naik, X. Sun, D. Bi, D. Malhotra, C. C. Hession, R. Shema, M. Gomes, T. Li, E. Hwang, A. Krol, M. Kowalczyk, J. Peça, G. Pan, M. M. Halassa, J. Z. Levin, Z. Fu, G. Feng, Distinct subnetworks of the thalamic reticular nucleus. *Nature* **583**, 819–824 (2020).

57. A. Clemente-Perez, S. R. Makinson, B. Higashikubo, S. Brovarney, F. S. Cho, A. Urry, S. S. Holden, M. Wimer, C. David, L. E. Fenno, L. Acsady, K. Deisseroth, J. T. Paz, Distinct Thalamic Reticular Cell Types Differentially Modulate Normal and Pathological Cortical Rhythms. *Cell Rep* **19**, 2130–2142 (2017).

58. M. R. DeLong, Activity of pallidal neurons during movement. *J Neurophysiol* **34**, 414–427 (1971).

59. A. Nambu, S. Yoshida, K. Jinnai, Discharge patterns of pallidal neurons with input from various cortical areas during movement in the monkey. *Brain Res* **519**, 183–191 (1990).

60. J. W. Mink, W. T. Thach, Basal ganglia motor control. II. Late pallidal timing relative to movement onset and inconsistent pallidal coding of movement parameters. *J Neurophysiol* **65**, 301–329 (1991).

61. J. W. Mink, W. T. Thach, Basal ganglia motor control. I. Nonexclusive relation of pallidal discharge to five movement modes. *J Neurophysiol* **65**, 273–300 (1991).

62. H. Mushiake, P. L. Strick, Pallidal neuron activity during sequential arm movements. *J Neurophysiol* **74**, 2754–2758 (1995).

63. D. Arkadir, G. Morris, E. Vaadia, H. Bergman, Independent coding of movement direction and reward prediction by single pallidal neurons. *J Neurosci* **24**, 10047–10056 (2004).

64. R. Schmidt, D. K. Leventhal, N. Mallet, F. Chen, J. D. Berke, Canceling actions involves a race between basal ganglia pathways. *Nat Neurosci* **16**, 1118–1124 (2013).

65. P. D. Dodson, J. T. Larvin, J. M. Duffell, F. N. Garas, N. M. Doig, N. Kessaris, I. C. Duguid, R. Bogacz, S. J. B. Butt, P. J. Magill, Distinct developmental origins manifest in the specialized

encoding of movement by adult neurons of the external globus pallidus. *Neuron* **86**, 501–513 (2015).

66. V. Marlinski, M. G. Sirota, I. N. Beloozerova, Differential gating of thalamocortical signals by reticular nucleus of thalamus during locomotion. *J Neurosci* **32**, 15823–15836 (2012).

67. V. Marlinski, I. N. Beloozerova, Burst firing of neurons in the thalamic reticular nucleus during locomotion. *J Neurophysiol* **112**, 181–192 (2014).

68. Y. Saga, Y. Nakayama, K.-I. Inoue, T. Yamagata, M. Hashimoto, L. Tremblay, M. Takada, E. Hoshi, Visuomotor signals for reaching movements in the rostro-dorsal sector of the monkey thalamic reticular nucleus. *Eur J Neurosci* **45**, 1186–1199 (2017).

69. M. Sunahara, A. Rios, M. Kawabata, S. Kato, S. Hamada, T. Ohtsuka, K. Kobayashi, H. Takahashi, Y. Isomura, Temporally Coordinated Activity among Motor Cortex, Thalamus, and Thalamic Reticular Nucleus Neurons during Rat Forelimb Movements. *J Neurosci* **46**, e1827252026 (2026).

70. G. J. Broussard, Y. Liang, M. Fridman, E. K. Unger, G. Meng, X. Xiao, N. Ji, L. Petreanu, L. Tian, In vivo measurement of afferent activity with axon-specific calcium imaging. *Nat Neurosci* **21**, 1272–1280 (2018).

71. F. Ali, A. C. Kwan, Interpreting in vivo calcium signals from neuronal cell bodies, axons, and dendrites: a review. *Neurophotonics* **7**, 011402 (2020).

72. Y. Brun, C. Karachi, S. Fernandez-Vidal, N. Jodoin, D. Grabli, E. Bardinet, L. Mallet, Y. Agid, J. Yelnik, M.-L. Welter, Does unilateral basal ganglia activity functionally influence the contralateral side? What we can learn from STN stimulation in patients with Parkinson's disease. *J Neurophysiol* **108**, 1575–1583 (2012).

73. V. H. Scholz, A. W. Flaherty, E. Kraft, J. R. Keltner, K. K. Kwong, Y. I. Chen, B. R. Rosen, B. G. Jenkins, Laterality, somatotopy and reproducibility of the basal ganglia and motor cortex during motor tasks. *Brain Res* **879**, 204–215 (2000).

74. N. Mallet, R. Schmidt, D. Leventhal, F. Chen, N. Amer, T. Boraud, J. D. Berke, Arkypallidal Cells Send a Stop Signal to Striatum. *Neuron* **89**, 308–16 (2016).

75. A. Pamukcu, Q. Cui, H. S. Xenias, B. L. Berceau, E. C. Augustine, I. Fan, S. Chalasani, A. W. Hantman, T. N. Lerner, S. M. Boca, C. S. Chan, Parvalbumin(+) and Npas1(+) Pallidal Neurons Have Distinct Circuit Topology and Function. *J Neurosci* **40**, 7855–7876 (2020).

76. Y.-G. Sun, C.-S. Wu, J. J. Renger, V. N. Uebele, H.-C. Lu, M. Beierlein, GABAergic Synaptic Transmission Triggers Action Potentials in Thalamic Reticular Nucleus Neurons. *J Neurosci* **32**, 7782–7790 (2012).

77. D. Ulrich, J. R. Huguenard, Nucleus-Specific Chloride Homeostasis in Rat Thalamus. *J Neurosci* **17**, 2348–2354 (1997).

78. T. Schmidt, N. Ghaffarian, C. Philippot, G. Seifert, C. Steinhäuser, H.-C. Pape, P. Blaesse, Differential regulation of chloride homeostasis and GABAergic transmission in the thalamus. *Sci Rep* **8**, 13929 (2018).

79. F. S. Cho, J. R. Huguenard, J. T. Paz, A Dual Inhibitory Network in the Thalamic Reticular Nucleus Delineated by Pallidal and Intra-Reticular Inhibition. bioRxiv [Preprint] (2025). https://doi.org/10.1101/2025.10.05.680571.

80. H. Kwak, W. Koh, S. Kim, K. Song, J.-I. Shin, J. M. Lee, E. H. Lee, J. Y. Bae, G. E. Ha, J.-E. Oh, Y. M. Park, S. Kim, J. Feng, S. E. Lee, J. W. Choi, K. H. Kim, Y. S. Kim, J. Woo, D. Lee, T. Son, S. W. Kwon, K. D. Park, B.-E. Yoon, J. Lee, Y. Li, H. Lee, Y. C. Bae, C. J. Lee, E.

Cheong, Astrocytes Control Sensory Acuity via Tonic Inhibition in the Thalamus. *Neuron* **108**, 691-706.e10 (2020).

81. N. Doyon, L. Vinay, S. A. Prescott, Y. De Koninck, Chloride Regulation: A Dynamic Equilibrium Crucial for Synaptic Inhibition. *Neuron* **89**, 1157–1172 (2016).

82. P. Bregestovski, T. Waseem, M. Mukhtarov, Genetically encoded optical sensors for monitoring of intracellular chloride and chloride-selective channel activity. *Front Mol Neurosci* **2**, 15 (2009).

83. L. J. Herstel, C. Peerboom, S. Uijtewaal, D. Selemangel, H. Karst, C. J. Wierenga, Using SuperClomeleon to Measure Changes in Intracellular Chloride during Development and after Early Life Stress. *eNeuro* **9**, ENEURO.0416-22.2022 (2022).

84. F. M. Zhou, “Chapter 15 - The Substantia Nigra Pars Reticulata” in *Handbook of Behavioral Neuroscience*, H. Steiner, K. Y. Tseng, Eds. (Elsevier, 2016; https://www.sciencedirect.com/science/article/pii/B9780128022061000155)vol. 24 of *Handbook of Basal Ganglia Structure and Function, Second Edition*, pp. 293–316.

85. H. Kita, D. Jaeger, “Chapter 13 - Organization of the Globus Pallidus” in *Handbook of Behavioral Neuroscience*, H. Steiner, K. Y. Tseng, Eds. (Elsevier, 2016; https://www.sciencedirect.com/science/article/pii/B9780128022061000131)vol. 24 of *Handbook of Basal Ganglia Structure and Function, Second Edition*, pp. 259–276.

86. M. R. DeLong, T. Wichmann, Circuits and circuit disorders of the basal ganglia. *Arch Neurol* **64**, 20–4 (2007).

87. A. M. Graybiel, The basal ganglia. *Curr Biol* **10**, R509-511 (2000).

88. A. Mathis, P. Mamidanna, K. M. Cury, T. Abe, V. N. Murthy, M. W. Mathis, M. Bethge, DeepLabCut: markerless pose estimation of user-defined body parts with deep learning. *Nat Neurosci* **21**, 1281–1289 (2018).

89. C. R. Houser, J. E. Vaughn, R. P. Barber, E. Roberts, GABA neurons are the major cell type of the nucleus reticularis thalami. *Brain Res* **200**, 341–354 (1980).

90. L. J. Gentet, D. Ulrich, Strong, reliable and precise synaptic connections between thalamic relay cells and neurones of the nucleus reticularis in juvenile rats. *J Physiol* **546**, 801–811 (2003).

91. D. Paré, L. N. Hazrati, A. Parent, M. Steriade, Substantia nigra pars reticulata projects to the reticular thalamic nucleus of the cat: a morphological and electrophysiological study. *Brain Res* **535**, 139–146 (1990).

92. V. Anaya-Martinez, A. Martinez-Marcos, D. Martinez-Fong, J. Aceves, D. Erlij, Substantia nigra compacta neurons that innervate the reticular thalamic nucleus in the rat also project to striatum or globus pallidus: Implications for abnormal motor behavior. *Neuroscience* **143**, 477–486 (2006).

93. M. Antal, B. M. Beneduce, W. G. Regehr, The substantia nigra conveys target-dependent excitatory and inhibitory outputs from the basal ganglia to the thalamus. *J Neurosci* **34**, 8032–8042 (2014).

94. M. Román Rosón, Y. Bauer, A. H. Kotkat, P. Berens, T. Euler, L. Busse, Mouse dLGN Receives Functional Input from a Diverse Population of Retinal Ganglion Cells with Limited Convergence. *Neuron* **102**, 462-476.e8 (2019).

95. I. C. Kilpatrick, M. S. Starr, A. Fletcher, T. A. James, N. K. MacLeod, Evidence for a GABAergic nigrothalamic pathway in the rat. I. Behavioural and biochemical studies. *Exp Brain Res* **40**, 45–54 (1980).

96. S. M. Sherman, R. W. Guillery, On the actions that one nerve cell can have on another: Distinguishing “drivers” from “modulators.” *Proceedings of the National Academy of Sciences of the United States of America* **95**, 7121 (1998).

97. C. C. Lee, S. M. Sherman, Modulator Property of the Intrinsic Cortical Projection from Layer 6 to Layer 4. *Frontiers in Systems Neuroscience* **3**, 3 (2009).

98. C. Varela, Thalamic neuromodulation and its implications for executive networks. *Front Neural Circuits* **8**, 69 (2014).

99. J. T. Paz, A. S. Bryant, K. Peng, L. Fenno, O. Yizhar, W. N. Frankel, K. Deisseroth, J. R. Huguenard, A new mode of corticothalamic transmission revealed in the Gria4(-/-) model of absence epilepsy. *Nat Neurosci* **14**, 1167–1173 (2011).

100. C. L. Cox, S. M. Sherman, Glutamate Inhibits Thalamic Reticular Neurons. *The Journal of Neuroscience* **19**, 6694 (1999).

101. D. A. McCormick, D. A. Prince, Acetylcholine induces burst firing in thalamic reticular neurones by activating a potassium conductance. *Nature* **319**, 402–405 (1986).

102. U. D, H. Jr, Gamma-aminobutyric acid type B receptor-dependent burst-firing in thalamic neurons: a dynamic clamp study. *Proceedings of the National Academy of Sciences of the United States of America* **93** (1996).

103. D. Ulrich, J. R. Huguenard, GABA(A)-receptor-mediated rebound burst firing and burst shunting in thalamus. *J Neurophysiol* **78**, 1748–1751 (1997).

104. D. Debay, J. Wolfart, Y. Le Franc, G. Le Masson, T. Bal, Exploring spike transfer through the thalamus using hybrid artificial-biological neuronal networks. *J Physiol Paris* **98**, 540–558 (2004).

105. V. S. Sohal, S. Pangratz-Fuehrer, U. Rudolph, J. R. Huguenard, Intrinsic and synaptic dynamics interact to generate emergent patterns of rhythmic bursting in thalamocortical neurons. *J Neurosci* **26**, 4247–4255 (2006).

106. S. R. Crandall, S. J. Cruikshank, B. W. Connors, A corticothalamic switch: controlling the thalamus with dynamic synapses. *Neuron* **86**, 768–782 (2015).

107. A. C. Lu, C. K. Lee, M. Kleiman-Weiner, B. Truong, M. Wang, J. R. Huguenard, M. P. Beenhakker, Nonlinearities between inhibition and T-type calcium channel activity bidirectionally regulate thalamic oscillations. *Elife* **9**, e59548 (2020).

108. S. W. Hughes, D. W. Cope, V. Crunelli, Dynamic clamp study of Ih modulation of burst firing and delta oscillations in thalamocortical neurons in vitro. *Neuroscience* **87**, 541–550 (1998).

109. D. W. Cope, S. W. Hughes, V. Crunelli, GABAA receptor-mediated tonic inhibition in thalamic neurons. *J Neurosci* **25**, 11553–11563 (2005).

110. Y. Shu, D. A. McCormick, Inhibitory interactions between ferret thalamic reticular neurons. *J Neurophysiol* **87**, 2571–2576 (2002).

111. D. Ulrich, J. R. Huguenard, GABAB receptor-mediated responses in GABAergic projection neurones of rat nucleus reticularis thalami in vitro. *J Physiol* **493 (Pt 3)**, 845–854 (1996).

112. J. R. Huguenard, D. A. Prince, Intrathalamic rhythmicity studied in vitro: nominal T-current modulation causes robust antioscillatory effects. *J Neurosci* **14**, 5485–5502 (1994).

113. D. A. McCormick, H. C. Pape, Properties of a hyperpolarization-activated cation current and its role in rhythmic oscillation in thalamic relay neurones. *J Physiol* **431**, 291–318 (1990).

114. S. G. Meuth, T. Kanyshkova, P. Meuth, P. Landgraf, T. Munsch, A. Ludwig, F. Hofmann, H.-C. Pape, T. Budde, Membrane resting potential of thalamocortical relay neurons is shaped by the interaction among TASK3 and HCN2 channels. *J Neurophysiol* **96**, 1517–1529 (2006).

115. S. G. Meuth, T. Budde, T. Kanyshkova, T. Broicher, T. Munsch, H.-C. Pape, Contribution of TWIK-Related Acid-Sensitive K+ Channel 1 (TASK1) and TASK3 Channels to the Control of Activity Modes in Thalamocortical Neurons. *J Neurosci* **23**, 6460–6469 (2003).

116. M. Steriade, L. Domich, G. Oakson, M. Deschênes, The deafferented reticular thalamic nucleus generates spindle rhythmicity. *J Neurophysiol* **57**, 260–273 (1987).

117. M. Bazhenov, I. Timofeev, M. Steriade, T. J. Sejnowski, Self-sustained rhythmic activity in the thalamic reticular nucleus mediated by depolarizing GABAA receptor potentials. *Nat Neurosci* **2**, 168–174 (1999).

118. D. A. McCormick, Cellular mechanisms underlying cholinergic and noradrenergic modulation of neuronal firing mode in the cat and guinea pig dorsal lateral geniculate nucleus. *J Neurosci* **12**, 278–289 (1992).

119. M. J. V. Hook, Temperature effects on synaptic transmission and neuronal function in the visual thalamus. *PLoS ONE* **15**, e0232451 (2020).

120. A. Destexhe, D. Paré, Impact of network activity on the integrative properties of neocortical pyramidal neurons in vivo. *J Neurophysiol* **81**, 1531–1547 (1999).

121. S. S. Holden, F. C. Grandi, O. Aboubakr, B. Higashikubo, F. S. Cho, A. H. Chang, A. O. Forero, A. R. Morningstar, V. Mathur, L. J. Kuhn, P. Suri, S. Sankaranarayanan, Y. Andrews-Zwilling,

A. J. Tenner, A. Luthi, E. Aronica, M. R. Corces, T. Yednock, J. T. Paz, Complement factor C1q mediates sleep spindle loss and epileptic spikes after mild brain injury. *Science* **373**, eabj2685 (2021).

122. F. S. Cho, I. D. Vainchtein, Y. Voskobiynyk, A. R. Morningstar, F. Aparicio, B. Higashikubo, A. Ciesielska, D. W. M. Broekaart, J. J. Anink, E. A. van Vliet, X. Yu, B. S. Khakh, E. Aronica, A. V. Molofsky, J. T. Paz, Enhancing GAT-3 in thalamic astrocytes promotes resilience to brain injury in rodents. *Sci Transl Med* **14**, eabj4310 (2022).

123. C. Rivera, J. Voipio, J. A. Payne, E. Ruusuvuori, H. Lahtinen, K. Lamsa, U. Pirvola, M. Saarma, K. Kaila, The K+/Cl- co-transporter KCC2 renders GABA hyperpolarizing during neuronal maturation. *Nature* **397**, 251–255 (1999).

124. R. J. Burman, P. J. N. Brodersen, J. V. Raimondo, A. Sen, C. J. Akerman, Active cortical networks promote shunting fast synaptic inhibition in vivo. *Neuron*, S0896-6273(23)00586-X (2023).

125. E. Pracucci, R. T. Graham, L. Alberio, G. Nardi, O. Cozzolino, V. Pillai, G. Pasquini, L. Saieva, D. Walsh, S. Landi, J. Zhang, A. J. Trevelyan, G.-M. Ratto, Daily rhythm in cortical chloride homeostasis underpins functional changes in visual cortex excitability. *Nature Communications* **14**, 7108 (2023).

126. H. Alfonsa, R. J. Burman, P. J. N. Brodersen, S. E. Newey, K. Mahfooz, T. Yamagata, M. C. Panayi, D. M. Bannerman, V. V. Vyazovskiy, C. J. Akerman, Intracellular chloride regulation mediates local sleep pressure in the cortex. *Nat Neurosci* **26**, 64–78 (2023).

127. H. Alfonsa, A. Chakrabarty, V. V. Vyazovskiy, C. J. Akerman, Sleep-wake-related changes in intracellular chloride regulate plasticity at glutamatergic cortical synapses. *Curr Biol* **35**, 1373-1381.e3 (2025).

128. J. Woo, A. Uprety, D. J. Reid, I. Chang, A. Ketema Samuel, H. de Carvalho Schuch, C. C. Swain, A. Ostroumov, Dynamic changes in chloride homeostasis coordinate midbrain inhibitory network activity during reward learning. *Nat Commun* **16**, 10903 (2025).

129. K. Kaila, Ionic basis of GABAA receptor channel function in the nervous system. *Prog Neurobiol* **42**, 489–537 (1994).

130. A. C. Brumback, K. J. Staley, Thermodynamic regulation of NKCC1-mediated Cl- cotransport underlies plasticity of GABA(A) signaling in neonatal neurons. *J Neurosci* **28**, 1301–1312 (2008).

131. N. Doyon, S. A. Prescott, A. Castonguay, A. G. Godin, H. Kröger, Y. De Koninck, Efficacy of synaptic inhibition depends on multiple, dynamically interacting mechanisms implicated in chloride homeostasis. *PLoS Comput Biol* **7**, e1002149 (2011).

132. J. R. Huguenard, B. E. Alger, Whole-cell voltage-clamp study of the fading of GABA-activated currents in acutely dissociated hippocampal neurons. *J Neurophysiol* **56**, 1–18 (1986).

133. S. M. Thompson, B. H. Gähwiler, Activity-dependent disinhibition. I. Repetitive stimulation reduces IPSP driving force and conductance in the hippocampus in vitro. *J Neurophysiol* **61**, 501–511 (1989).

134. K. J. Staley, W. R. Proctor, Modulation of mammalian dendritic GABA(A) receptor function by the kinetics of Cl- and HCO3- transport. *J Physiol* **519 Pt 3**, 693–712 (1999).

135. T. A. Spix, S. Nanivadekar, N. Toong, I. M. Kaplow, B. R. Isett, Y. Goksen, A. R. Pfenning, A. H. Gittis, Population-specific neuromodulation prolongs therapeutic benefits of deep brain stimulation. *Science* **374**, 201–206 (2021).

Publishing Agreement

It is the policy of the University to encourage open access and broad distribution of all theses, dissertations, and manuscripts. The Graduate Division will facilitate the distribution of UCSF theses, dissertations, and manuscripts to the UCSF Library for open access and distribution. UCSF will make such theses, dissertations, and manuscripts accessible to the public and will take reasonable steps to preserve these works in perpetuity.

I hereby grant the non-exclusive, perpetual right to The Regents of the University of California to reproduce, publicly display, distribute, preserve, and publish copies of my thesis, dissertation, or manuscript in any form or media, now existing or later derived, including access online for teaching, research, and public service purposes.

DocuSigned by:
Yau Ming (Isaac) Chang
929F89FB94394F9...
Author Signature

07/29/2026
Date